Magnetic Transduction for RF Micromechanical Filters

by

Sepehr Forouzanfar

A thesis
presented to the University of Waterloo
in fulfillment of the
thesis requirement for the degree of
Doctor of Philosophy
in
Electrical and Computer Engineering

Waterloo, Ontario, Canada, 2012

I hereby declare that I am the sole author of this thesis. This is a true copy of the thesis, including any required final revisions, as accepted by my examiners.

I understand that my thesis may be made electronically available to the public.

Abstract

The use of electrostatic transduction has enabled high-Q miniaturized mechanical resonators made of non-piezoelectric material that vibrate at high and ultra high frequencies. However, this transduction technique suffers from large values of motional resistance associated with the technique, limiting its use for interfacing to standard 50 Ω RF circuits. Piezoelectric transduction has advantages over the electrostatic method because of its comparable to 50 Ω motional resistance. However, the technique requires use of thin film piezoelectric materials with the demonstrated Qs that are much lower than their corresponding non-piezoelectric resonators. This research proposes use of electrodynamic transduction, reports analytic and experimental studies on electrodynamic transduction for RF application, highlights the method's advantages, and lists the contributions.

The use of Lorentz-force transduction for RF micromechanical filters proposed in this work is pursued by experimentally evaluating the transduction technique implemented for microfabricated designs. By fabricating single and coupled microresonators in a few different fabrication technologies, including CMOS35, the performance of the Lorentz-force driven microresonators is studied. Using a laser vibrometer, the actual performance, including the displacement and velocity of the moving points of the microstructures' surfaces, are measured.

The mode shapes and resonance specifications of the microstructures in air and vacuum derived by laser vibrometer provide data for characterizing the employed Lorentz-force transduction technique. Furthermore, the results from the electrical measurements are compared to the micromechanical resonators' frequency response obtained from the mechanical measurements by laser vibrometer. The significantly low values of motional resistance computed for the differently fabricated designs demonstrate the advantage of Lorentz-force transduction for RF filter applications. Should a device similar in size be driven electrostatically, the motional resistance would be multiple orders of magnitude higher.

This research reports the experimental results obtained by examining a Lorentz-force transduction application for developing RF micromechanical filters. The results demonstrate the Lorentz-force transduction's advantages over other transduction methods used for RF μ-mechanical filters. Compared to electrostatic transduction, the Lorentz-force method provides greater electromechanical coupling, multiple orders of magnitude lower motional resistance, the independence of the filter

center frequency from the bias voltage, higher power handling, and no requirement for bias lines, which decreases the work in microfabrication. Unlike piezoelectric transduction, the electrodynamic technique requires no piezoelectric material. Use of non-piezoelectric materials provides more flexibility for resonator material in the IC-compatible fabrications. Power handling in electrodynamic transduction has fewer limitations than other transduction techniques because the higher power needed in electrostatic or piezoelectric methods requires a higher voltage, which is limited by the breakdown voltage. The higher power in Lorentz-force-based transduction demands a larger current. The larger current produces heat that is removable by applying an appropriate cooling technique.

Acknowledgments

I would like to thank my supervisors, Professor Raafat Mansour and Professor Eihab Abdel-Rahman, for their patience, support, and encouragement. They have effectively spent time on my work, heard my reports, and encouraged me to go forward.

I am also grateful to Professor Safavi-Naieni, Professor Ismail, and Professor Boumaiza who agreed to be my thesis committee members. Thanks to Professor Chowhdury for serving as my external committee member.

Thanks to my fellow research group member, Dr. Siamak Fouladi Azarnaminy, who has helped me in the post processing of my designs on CMOS35 fabricated chips as well as Mr. Bill Jolley, CIRFE lab manager, who assisted me with his skills in lab related work. I would also like to thank Mr. R. L. Forgett from the University of Waterloo Engineering Machine Shop who fabricated my design of a mini-vacuum chamber. Without his patience and his excellent work, and without my supervisors, budgeting and support for mini-vacuum chamber's requirements, the characterization part of the microfabricated designs in this research would be hard to achieve.

Thanks to Mary McPherson who has spent time to review my thesis and provided me with the writing and presentation correcting suggestions.

Dedication

To people who have made significant contributions to civilization and better lives for others but received nothing in return D.1.

Contents

List of Tables

List of Figures

Nomenclature

A_0 effective opposing electrodes areas

A_c coupling beam's cross-section area

A_r resonator's cross-section

B magnetic intensity

BAW bulk acoustic wave

$C_M = 1/K$ compliance

C_c coupling beam's dispersion

$C_c l_c$ coupling beam's propagation constant

C_e capacitance

C_l coupling beam's location on resonator

E Young modulus

E^* combined Young modulus

E_K kinetic energy

E_c coupling beam's Young modulus

F force

$FBAR$ film bulk acoustic resonator

F_1 input force

F_2 output force

F_L Lorentz force

F_b time-dependent body force

G gap between meander coil and substrate

IL insertion loss

I_c coupling beam's bending moment

I_e current

I_f $n \times n$ identity matrix

I_{rms} input excitation current

K_c coupling beam's bending stiffness

K_{eq} equivalent stiffness

$K_{eq}(x)$ location dependent equivalent stiffness along the beam's length

Kc_{mn} coupling beam's stiffness

L inductance

M mass

$M(m, n)$ inter-resonator's coupling

M_f $n \times n$ filter's inter-resonator coupling matrix

M_{eq} equivalent mass

$M_{eq}(x)$ location dependent equivalent mass along the beam's length

Mi_{12} mutual inductance

Mi_{12} mutual inductance

Q quality factor

Q_L loaded quality factor

Q_m mechanical quality factor

Q_{UL} unloaded quality factor

Q_{filt} filter's quality factor

RQ_i input/output coupling

R_L return loss

R_M damping

R_Q input/output coupling

R_e resistance

R_f $n \times n$ filter's input/output coupling matrix

R_i input/output coupling

R_x motional resistance

R_{em} motional resistance

SAW surface acoustic wave

T Tesla

V velocity

V_P bias voltage

V_i input voltage

V_o output voltage

V_r reflected voltage

$Y_{a(mn)}$ shunt arm mechanical impedance

$Y_{b(mn)}$ series arm mechanical impedance

Z_M mechanical impedance

Z_e electrical impedance

Z_{e0} electrical source impedance

Z_{em} motional impedance

Z_{et} total input electrical impedance

Z_{m0} mechanical source impedance

$[R_f]_{11} = R_1$ filter's input coupling coefficient

$[R_f]_{nn} = R_n$ filter's output coupling coefficient

γ flex mode dependent coefficient

μ_0 free space permeability

$\overline{v}(t)$ average velocity

ρ material density

ρ^* combined density

ρ_c coupling beam's density

ρ_{comb} combined layers' density

σ residual stress

σ^* combined residual stress

$\vec{J_s}$ current density

d	electrodes gap
e	voltage
e_L	electromotive force
e_{ind}	induced voltage magnitude
e_{rms}	output sensing voltage
f	resonance frequency
f_0	filter's center frequency
f_{res}	resonance frequency
$fp(p)$	parasitic mode's freq
g_q	normalized filter's coefficient
g_{12}	gap
i	current
k_e	electrical coupling
l	resonator's length
l_c	coupling beam's length
$m_{q,q+1}$	inter-resonator coupling coefficient
t	μresonator thickness
t_c	coupling beam's thickness
u	displacement
$u(x)$	beam displacement
$u(x,t)$	beam displacement
$u\ (mp)$	midpoint maximum displacement
$u_{rms}(mp)$	mid-point displacement
v	velocity
$v(x)$	location dependent velocity along the beam's length
v_1	input velocity
v_2	output velocity
v_a	acoustic phase velocity
w	μresonator width
w_c	coupling beam's width

Chapter 1

Introduction

This chapter introduces the focus of this thesis. "Problem Statement" 1.1 declares the research motivation; "Outline" lists the thesis content and its organization, and "Contributions" summarizes the contributions made by this work. The background is provided to familiarize the readers with the multi-disciplinary nature of the research. The electrical filters' role in the efficient use of the electromagnetic spectrum for wireless communications, currently in-use mechanical filters, and the need for a transduction technique capable of overcoming the current techniques' limitations are described.

The limited frequency range of the electromagnetic spectrum usable for the increasing number of applications requires efficient use. Electrical filters have an important role in this purpose, where advancing communication systems, including mobile phones, demand high selectivity–high quality factor (Q)–low loss and miniaturized RF filters. These requirements cannot be addressed by electrical filters using electrical elements when size and cost restrictions are also involved. The significant advantages of mechanical filters are not limited to high Q values. Excellent temperature and aging characteristics, smaller resonator dimensions, better power handling capability, and more thermal stability are further advantages of mechanical filters [5]. However, mechanical filters require a transduction mechanism to couple energy between electrical and mechanical. Mechanical filters currently used in RF communication systems, miniaturized mechanical resonators for RF filter applications, and electrodynamic transduction for RF MEMS filters are briefly introduced.

Surface Acoustic Wave (SAW), bulk acoustic wave (BAW), and Quartz oscillators are the most important piezoelectric type filters and resonators currently in

use in communication systems. The ease of use and manufacture and the low cost make SAW very popular. However, being off-chip components and occupying a large space on the transceiver chip are important limitations of all of these piezo-type resonators and filters. Furthermore, SAW filters, for example, are limited in fabrication for higher frequency applications (above 2 GHz) because the electrodes' dimensions become smaller reaching fabrication tolerances. This limitation also affects the filter's power handling [6].

Requiring less power and demanding a lower cost in mass production, MEMS are orders of magnitude smaller than SAW. Work on the contour mode thin film resonators has produced interesting results, introducing a miniaturized version of piezo-type mechanical resonators that are developed for RF filter applications. However, as well as the need for piezoelectric material and low Q compared to non-piezoelectric microresonators, the in-plane thin film resonators suffer from low yield and difficulty in being coupled to function as standard filters [7], [8], [9].

Microelectromechanical resonators using electrostatic transduction are very promising for their Q and frequency performance. However, the large values of motional resistance involved in using electrostatic transduction is a challenge limiting use of the technique to interface with standard RF 50 Ω circuits. Nevertheless, use of electrostatic transduction has confirmed the possibility of manufacturing high performance miniaturized micromechanical filters, given that a more capable transduction technique be employed [10], [11], [12].

Magnetic transduction includes various techniques, three of which are proposed in my PhD thesis proposal for RF micromechanical filter applications. The first method uses electrodynamic transduction by implementing conducting microresonators in the presence of an external magnetic field. The second method is based on creating eddy currents in a conducting microresonator in the presence of an external magnetic field. The third method employs magnetostrictive materials. The first and second methods are based on Lorentz forces, and the third method employs microresonators made of a magnetostrictive material that has been widely employed for mechanical filters since 1946 [13].

However, while the first method requires a direct connection of RF signal to the transducer resonator, the second and third methods are non-contact transduction techniques. Both methods have advantages and limitations. Magnetic transduction use for mechanical filters is very attractive for its larger electromechanical

coupling compared to electrostatic and, there is no need for piezoelectric material compared to piezoelectric transduction [14]. This thesis focuses on the first method and mainly discusses experimental results obtained from employing electrodynamic transduction method.

The need for miniaturized micromechanical filters for RF applications requires transduction techniques to be integrable with RF circuits and be achievable in standard microfabrication technologies. Due to the large values of motional resistance in electrostatic transduction and the need for piezoelectric material and the lower Q of the piezoelectric thin film resonators, this thesis reports studies on Lorentz-force transduction for micromechanical RF filter applications.

1.1 Problem Statement

The significance of the mechanical resonators' advantages for electrical filtering when dimensions decrease outweigh the ones of the electrical resonators such that mechanical filters are currently in extensive use on most mobile transceivers. The large foot print of current mechanical filters used in RF mobile transceivers is a barrier to further development of these products. More free space on chips, less power consumption of the elements, and lower cost are needed. Accordingly, miniaturized mechanical filters addressing these needs are important prerequisites for developing RF mobile communication systems.

However, miniaturized mechanical filters require a transduction mechanism to convert energy from electrical to mechanical at the filter's input, and do the reverse conversion, from mechanical to electrical, at the filter's output. Electrostatic and piezoelectric transduction techniques are the most common methods, to which significant contributions have been made by researchers for RF filter applications.

Electrostatic transduction, which has been widely under investigation to serve this purpose, is limited by its large values of motional resistance (in the order of hundreds of $k\Omega$) [15], [7]. The large motional resistance of the device makes its interfacing to standard 50 Ω RF circuits unattractive. Lowering such a large motional resistance requires either smaller electrodes gaps (less than 20 nm) or a larger bias voltage. Both of these techniques are limited, in microfabrication and by breakdown voltage, respectively. The relationship governing the electrostatic transduction the input/output couplings is displayed in (1.1) [4]. R_Q, d, V_P, and A_0 represent

input/output coupling,the electrodes gap, bias voltage, and effective opposing electrodes areas, respectively. The gap decrease will also limit power handling due to lowering breakdown voltage.

$$R_Q \propto \frac{d^4}{V_P^2 A_0^2} \tag{1.1}$$

Piezoelectric transduction techniques using AlN require piezoelectric material, for which the reported Q is much lower than that for electrostatically driven ones. The low motional resistance ($50\ \Omega - 700\ \Omega$) of AlN resonators is an advantage compared to electrostatically driven resonators [7]. However, more challenges remain in making AlN resonators an integrated solution for RF application. The lower Q compared to non-piezoelectric resonators, the need for a piezoelectric material, compatibility to CMOS, and the difficulties in coupling resonators for multi-pole filters are among these challenges.

To address the need for a more capable transduction technique and in order to overcome the above limitations, this research involves analysis and experimental work using Lorentz-force transduction. The work includes analysis of the electrodynamic transduction technique and the implementation of microfabricated single and coupled microresonators. The microfabricated designs in various fabrication technologies and in CMOS35 allow for a comparison of results. CMOS35-fabricated designs driven by electrodynamic transduction demonstrate the technique potentials in IC-compatible technology. The content of the thesis is highlighted in section 1.2.

1.2 Outline

The thesis consists of five chapters, devoted to an introduction, literature review, analysis of Lorentz-force transduction, the microfabrication and experimental work, and conclusions, respectively. Four appendices are included that supply additional information.

Chapter 1 introduces the thesis topic, sets out the problem and the question this thesis addresses, outlines the thesis content and its organization, and gives the highlights of the research made.

Chapter 2 contains the literature review and presents a selection of previous works on mechanical filter transduction techniques, including work background and the contributions by other researchers to the field. The focus is on the strengths and shortcomings of the related work. Next, the mechanical resonators used for electrical filtering are reviewed, and the resonators are classified according to whether they are piezoelectric, magnetostrictive, or none of the two. Section 2.2 concentrates on miniaturized mechanical filters and the techniques employed in the previous work. Section 2.3 refers specifically to the records of using or proposing magnetic transduction for micromechanical filters.

Chapter 3 focuses on modeling and analysis of the proposed electrodynamic transduction for RF micromechanical filters. Section 3.1 describes modeling of electromechanical systems into pure electrical equivalent circuit. Section 3.2 illustrates typical multi-port filter designs to demonstrate the realization of the filter using Lorentz-force transduction. Section 3.3 examines the effect of mutual inductance on the performance of electrodynamically driven micromechanical resonators for RF filters.

Chapter 4 reports experimental work on the microfabricated designs. Section 4.1 explains the design and fabrication of micromechanical resonators implemented specifically to function by Lorentz-force transduction. Section 4.2 reports the experimental results on identifying resonance and mode shapes of Lorentz-force driven microresonators as well as electrical measurements on the performance of Lorentz-force driven micromechanical resonators. Section 4.3 reviews the results from measurements and computed values by equivalent circuit models.

Chapter 5 provides the readers with a summary of the thesis in section 5.1, highlighted contributions of the obtained results in section 5.2, and the plan for the work continuation in section 5.3.

"Appendix A" A consists of three parts including part of the work on which significant effort was made but is not reported because of too many challenges in microfabrication and characterization. Therefore, these parts are mentioned only for completion's sake. "Eddy-current based magnetic transduction" provides a summary of the proposed transduction technique, which was included in my PhD thesis proposal. The work on this technique pursued in microfabrication is briefly described. "Magnetostrictive transduction" is another proposed transduction technique to be implemented for RF MEMS filters and was also included in my PhD

thesis proposal. However, experimental work on this technique was not pursued due to limitations in fabrication facilities. Direct use of Lorentz-force transduction by employing meander coils has been attempted in microfabrication and is briefly reported.

"Appendix B," B "Multi-pole electrical filter design," includes an example of g-value computation for electrical filter design. The g-value computations referred to in section 3.2 are explained by demonstrating an example, where these g-values are also obtainable from electrical filter handbooks. "Y-matrix elements computation" illustrates the computation process for the Y-matrix elements discussed in section 3.2. These computations are necessary in the analysis of coupling beams, providing mechanical connections for microresonators.

"Appendix C" C includes selected "Avi" video files of the vibrating micromechanical resonators. The clips demonstrate measured performance of single, coupled two-, and coupled-three resonators. The displayed performances correspond to different mode shapes.

"Appendix D" D includes quotes or comments not directly relevant to this work; however, the author believes that some facts about the development history of science and technology are worth remembering. These are the scientific and technological contributions along with contributions in other aspects of human life that have made civilization happen and grow .

This outline briefly introduces the content and organization of the thesis. The contributions are listed in the next section.

1.3 Contributions

The contributions reported in this thesis are the outcome of the experimental work in examining Lorentz-force transduction application for developing RF micromechanical filters. Analysis and modeling of Lorentz-force transduction for single and coupled resonators form part of the reported achievements. The modeling technique is extendable to a higher number of coupled resonators. Fabrication of single and coupled microstructures driven by electrodynamic transduction is another part of the implementation process. The evaluation of the microfabricated designs in

experimental studies results in demonstration of the strength and advantages of the transduction technique for RF applications. This research made the following contributions:

- Implementing electrodynamic transduction for single and coupled micromechanical resonators for RF miniaturized filter applications
- Designing and fabricating micromechanical resonators using electrodynamic transduction in standard CMOS35 microfabrication technology displaying the feasibility of the technique in an IC-compatible microelectronic circuit technology
- Reporting multiple orders of magnitude lower motional resistance associated with Lorentz-force transduction for RF micromechanical filters. This greatly reduced motional resistance associated with electrodynamic transduction presented in this work is the very important advantage of using the proposed transduction technique for RF micromechanical filters.
- Highlighting other advantages of electrodynamic transduction over current transduction techniques: independence of the filter center frequency from bias voltage, larger electromechanical coupling compared to electrostatic [14], no need for a piezoelectric material and the corresponding fabrication challenges, higher power handling, and no requirement for bias lines, which decreases the work in microfabrication.
- Adopting multi-port electrical filter design techniques in the implementation of the design of multi-port micromechanical filters using electrodynamic transduction The detailed analysis process is described in section 3.2.
- Employing electrodynamic transduction in driving a clamped-clamped micromechanical resonator (U2) to its higher modes (9th mode)

The results of this research was presented at the Transducer Conference 2011 and published in IEEE Computer Society and IEEEXplore [16]. The journal version of the conference paper, "Lorentz force transduction for RF micromechanical filters," was published in the Journal of Micromechanics and Microengieering [17]. The second journal paper, "Highly reduced motional resistance of coupled micromechanical resonators for RF filters," reporting another part of the results was submitted for publication in Journal of Micromechanics and Microengieering on February 13, 2012.

Chapter 2

Literature Review: Mechanical Filter Transduction Techniques

This chapter reviews the most relevant literature on the topics of "Mechanical resonators for electrical filtering," "RF MEMS filters' transduction techniques," and "Mechanical filters by magnetic transduction" in sections 2.1, 2.2, and 2.3, respectively; these introducing the background of work on micromechanical filters, describing the employed transduction techniques, and highlighting the advantages and shortcomings of the employed techniques. The literature review on transduction techniques for RF micromechanical filters is preceded by a brief history of electrical filter development. Electrical filter development milestones, today's most common types of microwave filters, and the theoretical frequency limitation of mechanical resonators are briefly reviewed.

The discovery of the first image-parameter electric wave filters in 1915 (independently by Wagner and Campbell) was an important step in the development of filter theory and design [18]. The achievements in filter design theories were significant between the 1920s and 1930s, when the real components were limited to passive elements, including inductors, capacitors, resistors, and transformers.

Active RC filters using active components–thermionic valves and semiconductor devices–developed after the second World War. The development of switched-capacitor filters in the 1970s was a turning-point in filter advances. Using the ratio of capacitors to simulate a resistor, switched-capacitor filters eliminate the need for resistors, which are expensive and take a lot of room in manufacturing. The introduction of the first single chip digital signal processor in the 1980s increased

the importance of digital filters, which process binary-coded samples taken from analog signals.

Today's most common types of microwave resonators are of three main types [19]: lumped-element–LC, planar, and three-dimensional cavity-type resonators. Microchips of inductors and capacitors, microstrips in the shape of a transmission line or ring, and rectangular, circular, or dielectric waveguides are examples of these three main types, respectively.

Mechanical vibrations are propagated in air at frequencies as high as 500 MHz (a wavelength of about 0.6 m), which is an order of magnitude of the mean free path of air molecules. In solids, the upper limit for mechanical vibration's frequency is the intermolecular spacing of approximately 0.1 nm, corresponding to a limiting frequency of about one Terahertz. However, the ultimate limit is set for a wavelength equal to lattice cells [20].

Reviewing the literature illuminates where the work of this thesis stands, displaying the work's bridging role in connecting past contributions to future developments. The need and importance of the work is described by providing the readers with a brief history of electrical filters development, the most common of today's conventional RF filters, and the limitations in frequency that restrict mechanical filters' ability to address the needs of electrical filtering. Mechanical resonators for electrical filtering, the transduction techniques employed for micromechanical filters, and the background of magnetic transduction for micromechanical resonators are considered in the following sections.

2.1 Mechanical resonators for electrical filtering

Where electrical filters make use of electrical elements (inductors and capacitors) to process electrical signals, mechanical filters employ the resonance of mechanical structures for electrical filtering. Mechanical resonators made of piezoelectric or magnetostrictive material do not require a transducer. However, non-piezoelectric and non-magnetostrictive resonators do need such mechanism to convert electrical signals to mechanical motions or vice versa. Mechanical filters can be categorized based on the type of transduction technique or according to the type of employed resonators.

Discovery of piezoelectricity by the Curie brothers in 1881 initiated applications in various fields. However, having an important role in the development of mechanical filters, piezoelectric materials have applications either in transducer or resonators. The oldest known natural piezoelectric material is quartz, and its first application was in underwater transducers during World War I, as studied by Paul Langevin. Quartz crystal oscillators were developed later. Good chemical and physical stability, high Q in the range of 400,000 to 1 million, and a very low temperature coefficient re the reasons for extensive use of quartz in oscillators and resonators. Nevertheless, quartz's small electromechanical coupling coefficient limits its application in filters.

Barium titanate is another well-know piezoelectric discovered between 1942 to 1944, whose first use in mechanical filters was in a transducer. A Langevin-type transducer consists of a barium titanate disk sandwiched between two metal disks. The Murata manufacturing company developed these filters using the radial vibration modes of steel balls. These 455 KHz low-cost mechanical filters were for consumer market radios needs. Low yields because of unwanted vibration modes of steel balls led to the direct use of coupled Langevin transducers without steel balls [21]. Unlike Rochelle salt, which is water soluble and has poor temperature characteristics, and which was used for underwater transducers and phonograph pickup, barium titanate is not water soluble and has a high coupling coefficient. However, barium titanate has two weaknesses: a poor temperature coefficient and excessive aging because of the low Curie point. Work on improving barium titanate's performance led to the discovery of PZT, which has advantages over barium titanate.

The limitation in making physically smaller filters from Langevin-type transducers and the market demand for miniaturized filters motivated research toward direct use of piezoelectrics as resonators. Figure 2.1 illustrates radially resonating PZT disks used in ladder-type filters along with their equivalent series and parallel circuits [21]. These filters were developed for U.S. Army between 1958-1960. Operating at 455 KHz and 4.3 MHz, these ladder-type filters use radial modes of the ceramic disk resonators. Figure 2.2 displays radially resonating PZT disks used for 455 KHz IF filters. Similar filters were later used for commercial communication equipment [21].

Using thickness shear vibration mode of an AT-cut quartz crystal plate, a 4.3 MHz filter was developed by Curran in 1961. Curran also used thickness-expansion mode of a PZT disk to make a 10.7 MHz filter. Acoustically coupled resonators were

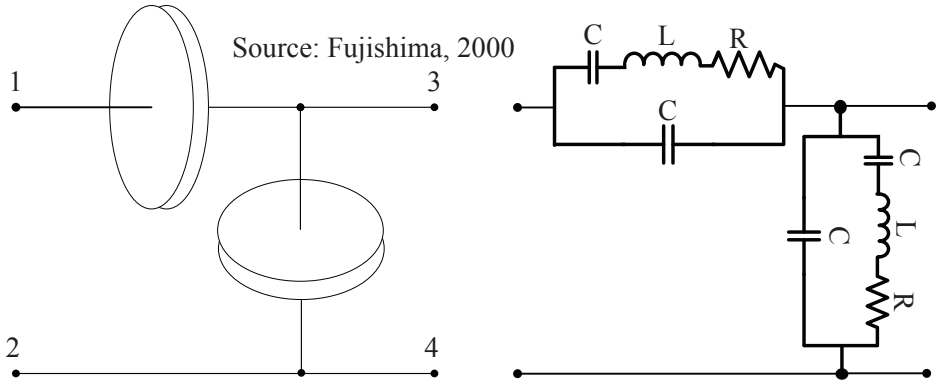

Figure 2.1: Ladder-type PZT filters and their equivalent circuits

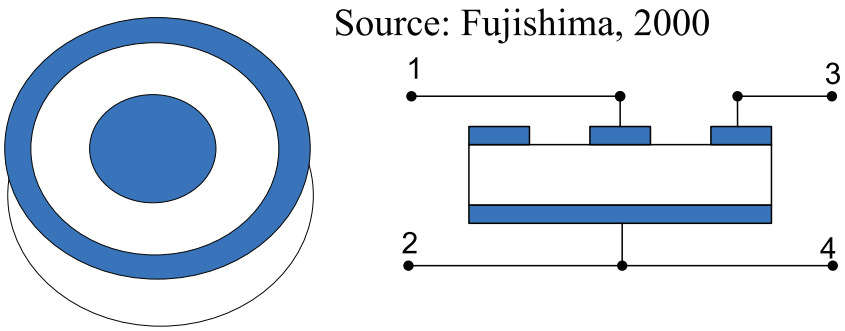

Figure 2.2: Radially resonating PZT disks used for 455 kHz IF filter

developed in 1962. Coupled-mode 10.7 MHz ceramic filters, using the thickness-expansion vibration mode, for FM automobile radios, were developed in 1967. The design consists of two acoustically isolated coupled-mode filters on a ceramic wafer and a coupling capacitor. Philco-Ford ordered a large quantity of these filters in 1970 [21].

Following the theoretical work on energy trapping published by W. Shockley in 1963, a 10.7 MHz crystal filter using the multi-energy trapping mode of thickness shear vibration was developed by Professor Onoe in 1964. Using inter-digital electrodes deposited on a piezoelectric substrate, the practical development of Surface Acoustic Wave (SAW) filters was suggested by White in 1965. However, the surface acoustic waves were discovered by Lord Rayleigh who published his studies' results

in 1885.

Development of SAW filters has experienced fluctuations because of the varying market demand after 1965. However, rapid growth of mobile communications created a significant interest toward further development and application of SAW filters since the 1980's. Commonly used piezoelectrics for SAW filters are lithium niobate, lithium tantalate, and quartz. Suffering from thermal stability, lithium niobate has an advantage over quartz for its strong coupling. Better than both, quartz and lithium niobate, lithium tantalate exhibits strong coupling and good thermal stability for SAW filters.

In 1980, independent groups reported their results on FBAR whose simple configuration is displayed in figure 2.3 [22]. The structure consists of a diaphragm with a P^+-doped Si layer on which an aluminum electrode and a piezoelectric film of zinc oxide are deposited. A cavity is also formed by the anisotropic etching of a (100) Si substrate.

Use of piezoelectric thin film resonators for mobile communications began early in the 1990's. No requirement for high resolution photo-lithography for electrode spacing is one advantage of FBARs over SAW. Further advantages of FBARs over SAW are higher Q, higher frequency, and lower loss. Despite these advantages, SAW filters still dominate the market because of low cost, ease of resonators coupling, ease of manufacture, and an acceptable level of performance.

However, the work by Ruby et al. shows a good performance of FBAR filters for mobile communications [22]. Extensive on-going investigations focus on different types of FBAR and SMR using either ZnO or aluminum nitride (AlN) thin films [23], [7], [24]. These efforts aim at increasing the performance of thin film resonators and overcoming the limitations of these type of resonators for future filter applications.

Robert Adler introduced the first practical electromechanical filter in 1946 [13]. This mechanical filter operates at 455 KHz and uses magnetostrictive transducers. Following Adler's work, rod-neck and disk-wire filters were developed. For their high Q and good temperature and aging stability, these filters were employed in first high performance receivers resulting in the fast development and extensive use of single-sideband equipment [25]. The work by Mason (in 1941-2) and others at

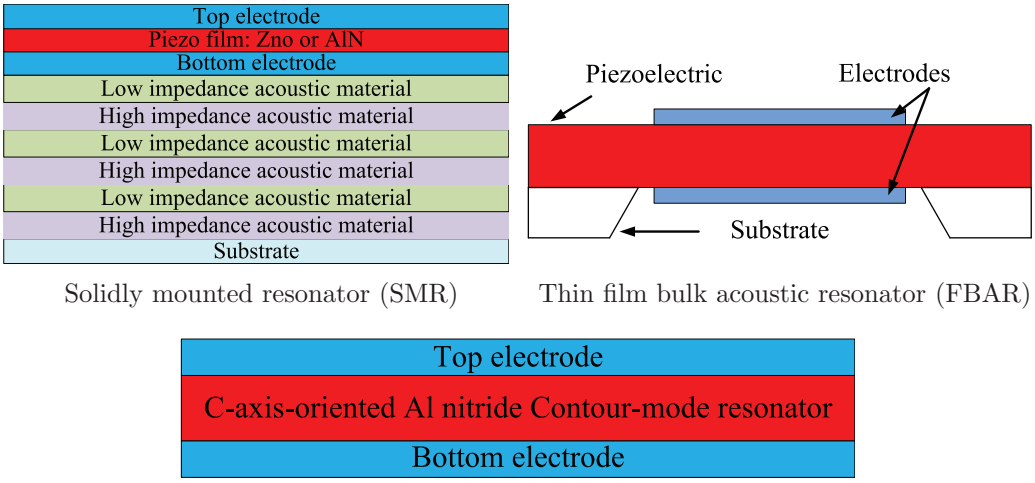

Figure 2.3: Common types of piezoelectric thin film resonators

Bell Laboratories, describing spring-mass systems and transmission-line mechanical filters, are the earlier essential steps taken in mechanical filter developments [26].

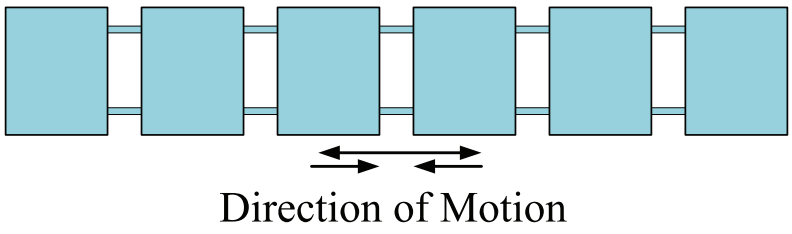

Figure 2.4: 1st practical mechanical filter operating at 455 KHz

Figure 2.4 shows the central structure of Adler's plate-type filter designed for 455 KHz Intermediate-Frequency (IF) and driven by magnetostrictive transducers. Extensional-mode resonating metal plates are mechanically coupled, providing the filter with a bandwidth of 0.02 % and Q in the range of 2000 to 4000. Figure 2.5 depicts the resonating structure of the neck-and-slug type filter developed by Roberts, Burns, and George in 1949 to 1956. The neck-and-slug type filter can operate in two modes: torsional and extensional. The small diameter quarter-wave

length coupling rods provide spring coupling between resonators. A distinguishing feature of the neck-and-slug type filter vibrating in longitudinal is its use of mass coupling instead of spring coupling [27].

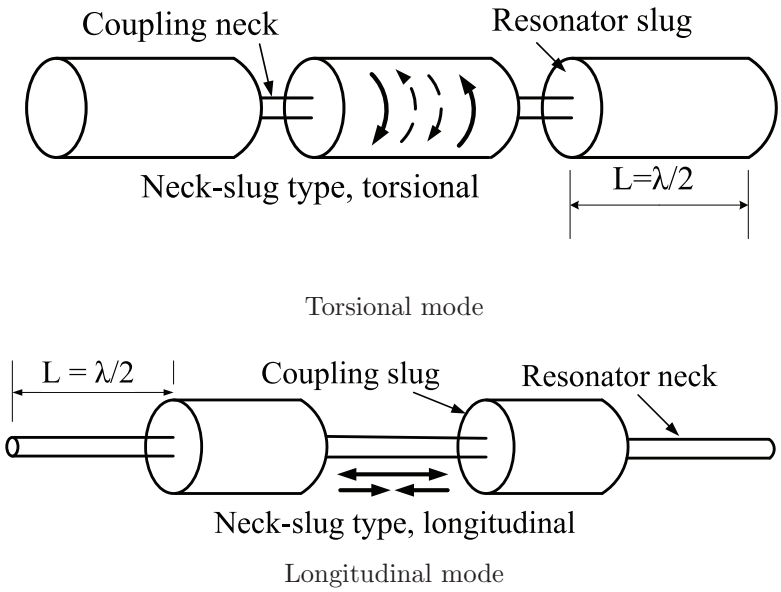

Figure 2.5: Neck-and-slug type mechanical filter

Illustrated in 2.6, disk-type filters made of Ni-Span C resonators vibrate in flexural mode with their motion directions perpendicular to the disks' flat surfaces. The Q of disk-type resonators is as high as 10,000. The thickness and diameter of disks adjust the resonance frequency. The number of disks determines the selectivity and the total cross-section area of the coupling wires defines the bandwidth. The very important advantage of disk resonators is the improvement in spurious responses, reduced from 60 dB to 100 dB below the pass band level. Disk-type mechanical filters are discussed by Doelz, Hathway, and Brown, in 1953 [27].

The transduction mechanism in all three types of mechanical filters described above is magnetostrictive. However, with the advent of better performance piezoelectric materials, piezoelectric transduction has later received increasing popularity. Larger electromechanical coupling is the important advantage of piezoelectric transducers. When a ferrite-type transducer provides an electromechanical coupling of about 10 %, the electromechanical coupling of a piezoelectric transducer

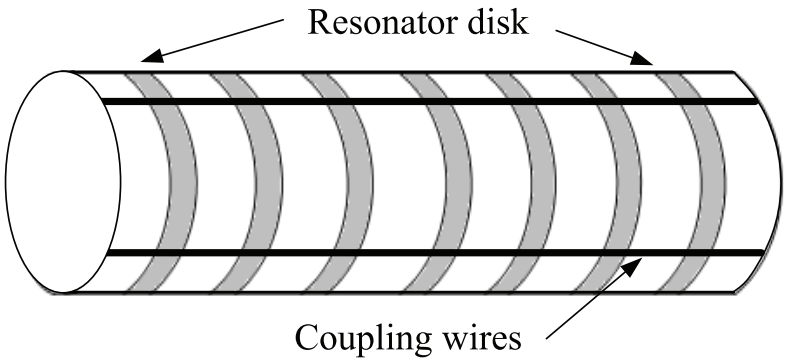

Figure 2.6: Mechanical filter using disks flexural mode resonation

may reache 15 % to 25 % or even more. The preferred piezoelectric transducers is the Langevin-type, which is a piezoceramic sandwiched between two metal plates.

Ferrite magnetostrictive materials provide better performance and lower loss compared to magnetostrictive alloys. Ferrite types show a transduction loss of 2 dB while alloy types display an insertion loss of 8 dB to 15 dB[1] . Comparing insertion loss, the ferrite and alloy types involved have an insertion loss of less than 2 dB and about 16 dB, respectively. The main source of this loss is the eddy current. The input impedance of these filters ranges between a few hundred Ω to $50,000\ \Omega$ [27].

Torsional rod-wire, introduced by Borner (1958/1962) and Tanaka (1959), and tuning fork, developed and widely used in Japan (1965), are two other important types of mechanical filters. Following these developments, significant research on modeling and analysis of mechanical resonators and coupling elements resulted in a better understanding of mechanical filters and their characteristics [5]. The demand for lower cost miniaturized filters to satisfy the need in mobile communication systems with no other advantageous alternative made mechanical filters using piezoelectric resonators more attractive.

This literature review is on the types of mechanical resonators for electrical filtering. Mechanical resonators that are either piezoelectric or magnetostrictive do

[1]Transmission loss is defined equal to $20\log(V_i/V_o)$ and insertion loss equal to $20\log(V_i/V_r)$ where V_i, V_o, and V_r are input, output, and reflected voltages, respectively.

not require any transduction techniques. However, mechanical resonators that are non-piezoelectric and non-magnetostrictive do require a transduction technique. In section 2.2, transduction techniques employed for RF MEMS are reviewed.

2.2 Transduction techniques for RF MEMS filters

Miniaturization of mechanical filters enabled by MEMS technology was not possible in the 1960's. Driven electrostatically and sensed capacitively, a resonant microbridge was introduced as a chemical vapor sensor in 1986 [28]. This achievement highlighted MEMS potential for micromechanical resonators and filters. Work on laterally driven polysilicon resonant microstructures that function at a low frequency range of 18 kHz to 80 kHz and quality factors from 20 to 130 was published in 1989 [29]. RF MEMS filters are mostly recognized for their use of electrostatic transduction.

The results of using electrostatic transduction to drive micromechanical resonators in Very High Frequency (VHF) and Ultra High Frequency (UHF) with high-Q values ($\geq 10,000$) are very promising [30]. Electrostatically driven rings resonating at 1.46 GHz with a Q of 15,248 are a world record [8]. Contour-mode disk resonators made of Polysilicon are demonstrated that resonate at 1.156 GHz with Q of 2650 (both in air and vacuum) [31], 734.6 MHz with a Q of 7800 (in vacuum) and 5160 (in air) [31], and 193 MHz with Q of 23,000 (in air) [11]. Work on MEMS resonators for RF filter applications is not limited to disks and rings or only to single resonators.

Reported results on clamped-clamped microbeam (ccμbeam) [4] and single free-free microbeam [1] resonating at 8.51 MHz and 71.5 MHz with Qs of 8000 and 8250, respectively, were also published. Furthermore, two-pole and three-pole filters consist of a coupled ccμbeams [4] and folded-beam (combdrive) were introduced [12]. For example, the performance of an electrostatically driven two-pole filter was reported [4]: center frequency 7.81 MHz, filter's Q 435, resonators' Q 8000, resonator's (beam) length 40.8 μm, bandwidth of 18 KHz, insertion loss (IL) 1.8 dB, and input/output couplings (RQ_i)19.6 $K\Omega$. For overcoming large motional resistance in use of electrostatic transduction, some researchers are focused on increasing the effective actuation/sensing area (A_0) [9], [32], [33].

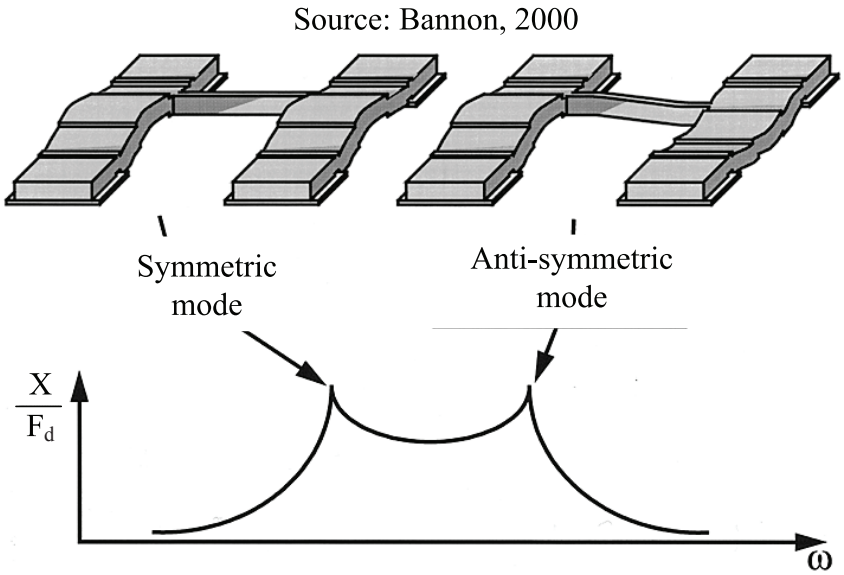

Figure 2.7: Coupled clamped-clamped microbeams filter [1].

A filter design to attain large stiffness-to-mass ratios was proposed using two clamped-clamped microbeams coupled by a soft flexural-mode mechanical spring, as shown in 2.7. The large stiffness to mass ratio enables a large dynamic range and power handling in micromechanical filters. However, the limitation of this design is its significant energy dissipation to the substrate via its anchors. The filter's resonance frequency is 8 MHz, and the bandwidth depends on both the coupling spring dimensions and location between the resonators. $Q-$values from 40 to 450 corresponding to the bandwidth percentage of 0.23 to 2.5, was reported [4].

To minimize anchor dissipation in using clamped-clamped resonators, a filter design employing free-free microbeam resonating in flexural-mode was proposed. In this design, the microbeams' ends were not clamped to the substrate but to the body of other fixed-ends microbeams, as shown in 2.8. Consequently, a dramatic improvement with Q-values as high as 8400 at VHF frequencies from 30 MHz to 90 MHz was demonstrated. The Q is one order of magnitude higher than the one in the clamped-clamped type filter [1]. Figure 2.8 shows (a) Perspective view of free-free beam microresonators, depicting bias, excitation, and off-chip output, (b) Top view, and (c) ANSYS simulation of the resonator's mode shape.

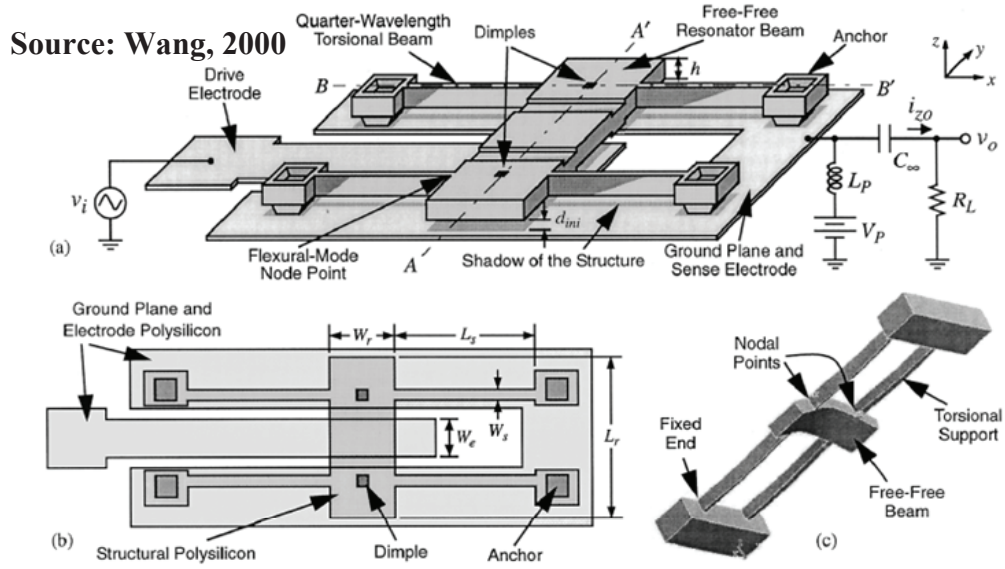

Figure 2.8: Filter using free-free beam microresonators

Using combined polysilicon surface-micromachining and metal electroplating microfabrication techniques, researchers at the University of Michigan developed a laterally vibrating disk resonator whose demonstrated high frequency was 829 MHz with a very high $Q-$value of $23,000$ at 193 MHz. The resonator operates at atmospheric pressure and shows a $Q-$value of $8,800$; this high $Q-$value without vacuum packaging confirms the resonator's potential applications by ordinary packaging. Figure 2.9 shows a plotted frequency in relation to a disk's diameter, mode shapes and relative displacements, a perspective view, and a SEM of a fabricated design for 433 MHz $(1stmode)$ [34].

Should the above disk be resonating in flexural mode at the same frequency, the microdisk's dimensions have to be significantly smaller. However, resonating in contour mode, the disk is fabricated with larger dimensions. This feature is an advantage from a fabrication point of view, increasing the potential disk's applications in future IF and RF circuits. Nevertheless, obtaining a submicron lateral capacitive gap in the microfabrication is very challenging limiting the potential development.

The micromechanical filters potential to be incorporated into a wireless receiver is examined by a proposed design of a filter-mixer combination taking use

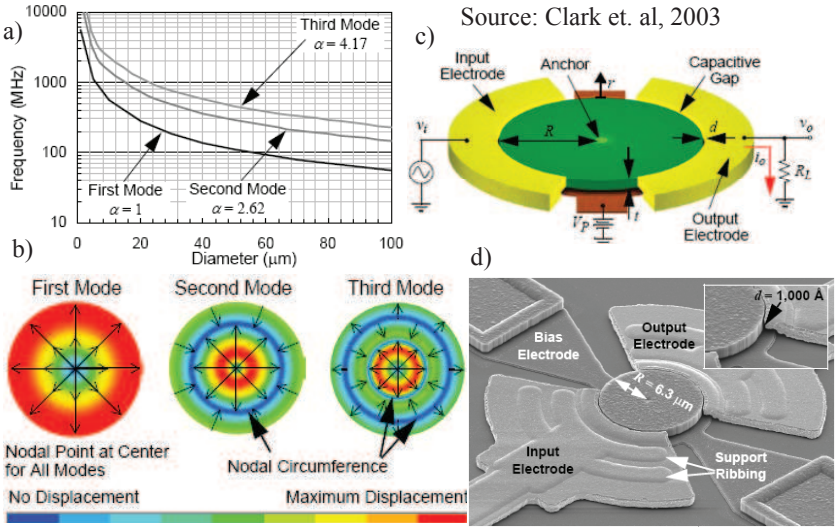

Figure 2.9: Disk resonator: (a) frequency versus disk's diameter (b) Contour plots, the relative displacement, and mode shapes (c) perspective view (d) SEM of a fabricated disk for 433MHz (1st mode) [34].

of clamped-clamped resonators. The configuration is based on capacitive mixer transducers. As a result, both the frequency mixing and highly selective low-loss filtering of electrical input are performed. The conversion of a $200 - MHz$ RF signal down to a $37 - MHz$ IF signal and subsequent filtering at the IF frequency were reported [35].

The mechanically-coupled flexural-mode of square resonator arrays are proposed to lower the impedance of a 68.1 MHz (VHF) microresonator. The result shows a less than 2.7 dB insertion loss for a 190 KHz passband width (0.28 % bandwidth). The design features are shown in 2.10. Although the $Q-$values of the resonator array are lower in comparison to a $Q-$value of a single square resonator, the filter still has excellent performance [36]. Work on PolyMUMPs fabricated coupled two clamped-clamped beam resonators was reported using v-shape coupling [37], [38]. These coupled resonators are driven by electrostatic transduction.

Researchers working on Aluminum Nitride (AlN) piezoelectric resonators whose frequencies are determined by in-plane dimensions report very promising results [30], [8], [7], [39]. These contour-mode resonators in the shape of plates and rings

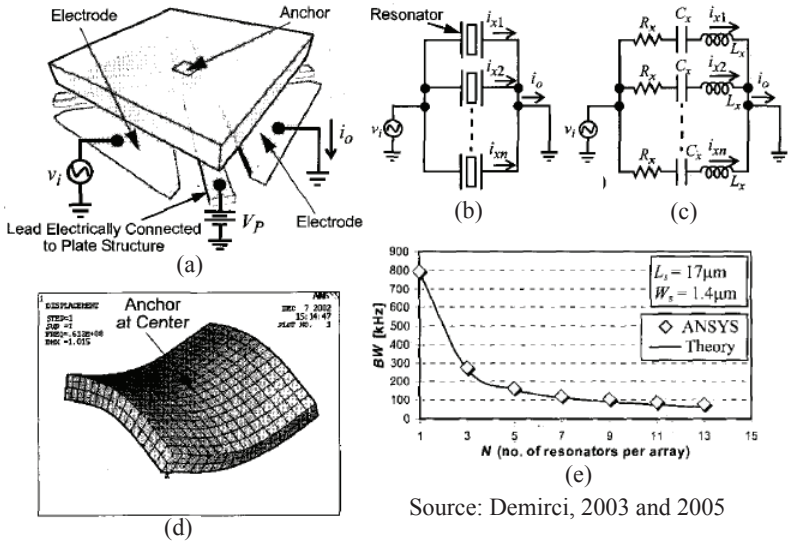

Source: Demirci, 2003 and 2005

Figure 2.10: (a) Perspective-view displaying bias, excitation, and sensation (b) array of Square plate resonators in parallel; R_x is motional resistance of each resonator (c) array's equivalent RLC circuit (d) ANSYS simulation of mode shape [36].

allow multiple frequencies on the same substrate, providing an advantage over FBARs. Resonators with a center frequency of 229.9 MHz and Q of 4300 (in air) [7] and a filter with an insertion loss of 4.8 dB, fractional bandwidth of 0.5 %, and operating frequency of 22.4 MHz were demonstrated [39], [40]. Thin film resonators using AlN piezoelectrics demonstrate the important advantage over electrostatic methods for their low values of motional resistance compared to electrostatic method.

The literature review on the use of different transduction techniques for RF MEMS filters shows that electrostatic transduction has played an impressive role by demonstrating promising results in developing miniaturized mechanical filters for RF applications. Electrostatically driven rings at the frequency of 1.46 GHz with a Q of 15,248 [8] is an example. A variety of geometries and designs of single as well as coupled resonators are developed using electrostatic transduction. Furthermore, a large number of research work are devoted to lowering the large values of motional resistance involved in use of electrostatic transduction. Research work on AlN piezoelectric resonators using piezoelectric transduction shows a motional resistance close to 50 Ω. The literature review on use of magnetic transduction is covered in

section 2.3.

2.3 Mechanical resonators by magnetic transduction

Use of magnetic transduction is not as common as the electrostatic or piezoelectric methods. In fact, the majority of the reported achievements on MEMS micromechanical filters employ electrostatic excitation and capacitive (electrostatic) detection or piezoelectric transduction. However, use of these magnetic transduction methods was also reported in literature. Lorentz-force transduction use for excitation of SAW and bulk acoustic waves, magnetically driven resonators for sensing applications, remote excitation and detection by magnetic transduction for non-destructive needs, and proposed use of Lorentz-force transduction for RF micromechanical filters are reviewed, here.

Use of Lorentz transduction to excite SAW or bulk acoustic waves on both non-piezoelectric conductors as well as on non-piezoelectrric dielectric are achieved. These applications are toward developing resonators and filters using meander shape electrodes deposited on substrates in the presence of a magnetic field. The operating frequencies include MHz and above MHz frequency range [41], [42], [43].

The wave equation for the electrodynamic transduction is displayed in (2.1) [44]. u , z , v_a , E , and F_b are displacement along z-direction, propagation direction, acoustic phase velocity ($v_a = \sqrt{E/\rho}$), Young modulus, and a time-dependent body force derived from $\vec{F_b}(t,z) = \vec{J_s} \times \vec{B}$, respectively, where $\vec{J_s}$, $\vec{B}$, and ρ are time-dependent current density, magnetic intensity, and material density.

$$\frac{\partial^2 u}{\partial z^2} - \frac{1}{v_a^2}\frac{\partial^2 u}{\partial t^2} = -\frac{1}{E}\frac{\partial F_b}{\partial t} \tag{2.1}$$

For non-piezoelectric dielectrics, a thin layer of conductor patterns such as meander shape designs is deposited on top of dielectric substrate for SAW excitation and incorporated inside the substrate for bulk mode. The substrate inserted in a magnetic field experiences Lorentz force for the RF signal inputted through the conducting pattern. Figure 2.11 illustrates an example of this configuration for bulk mode excitation. With the substrate being a non-piezo-conductive material,

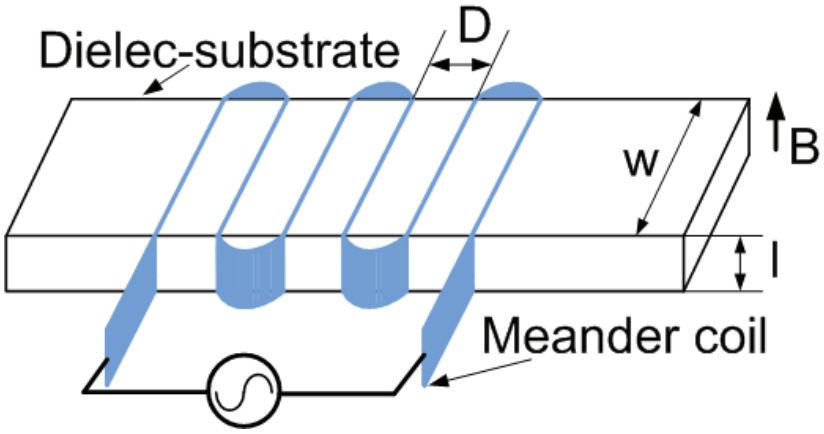

Figure 2.11: Lorentz-force transduction for SAW excitation on non-piezo-dielectric

the coil in the shape of a meander, for example, is fixed with a distance, G, above the substrate. In this configuration, the eddy current inductively generated in the conductive substrate interacts with external magnetic field and generates SAW.

Lorentz-force transduction is employed in the development of a very sensitive pressure sensor using silicon H-shape microstructure [45]. Figure 2.12 shows a schematic of excitation and sensing of the H-shape microstructure that is driven by electrodynamic transduction for a resonant strain gage [2]. The H-shape resonant strain gage is fabricated from heavily doped P^+ silicon.

Research on the resonant structures for sensing applications makes use of Lorentz-force transduction in driving a silicon nitride membrane to resonance [3]. Figure 2.13 displays the silicon nitride membrane that is suspended on a rectangular silicon frame. Patterned conductor lines on the membrane carrying an alternate current in the presence of an in-plane static magnetic field drive the membrane plate to its out-of-plane flexural mode resonation.

A u-shape resonator made of a brass–reed-like structure–inserted in a static magnetic field was evaluated as an acoustic sensor for filter application [46]. Sound waves at the resonance frequency drive the resonator and cause a voltage appears at the fixed ends of the structure, displayed in 2.14.

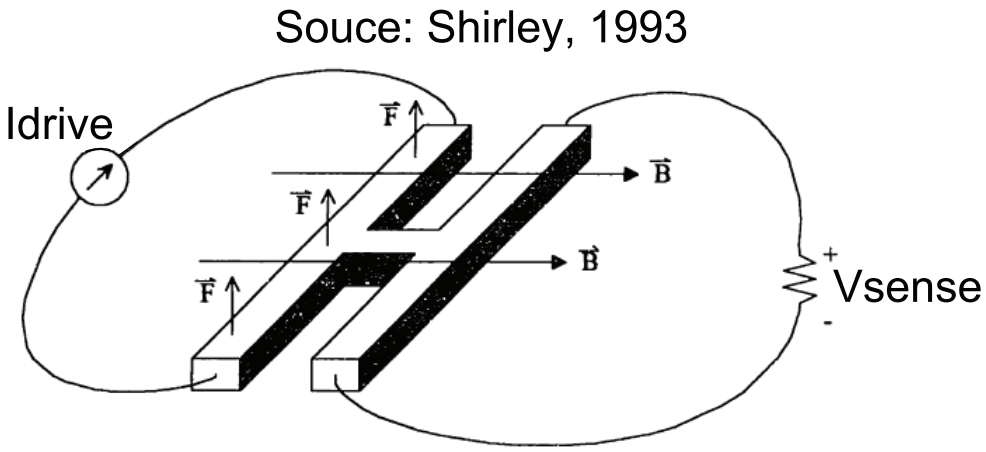

Figure 2.12: Lorentz-force transduction for H-shape strain gage resonator [2]

A well-known technique in non-destructive testing is use of electromagnetic excitation and detection to identify flaws in materials. Accordingly, the acoustic waves are inductively generated and detected in the material. However, because of high loss of transduction (about 100 dB transduction loss), use of high current pulses in the range of 20 Amp is required to create signals detectable with the available equipment. A more efficient way of using this technique is proposed to develop microresonators with high Q factors [47], [48]. For example, a spiral coil carrying RF signal in the vicinity of a silicon membrane generates eddy current in the microstructure. Interaction of an external magnetic field with this induced current develops Lorentz forces. The varying Lorentz forces at the resonance frequency drives the microstructure into resonance. Using non-contact electromagnetic excitation and detection, experimental work reports high-Q silicon resonator sensor with measured Q-factor up to 10^5 [49].

Among the most relevant to the research reported in this thesis is the proposed use of Lorentz force to excite a u-shape-cantilever microresonator [50]. The application is for narrow band pass RF filter. Microstructures in the shape of cantilever and fixed-fixed microbeams are assumed on which conducting lines are deposited. This configuration is to be inserted in a strong magnetic field of 2 $Tesla$. The same resonator is suggested for vibration sensing for the electromotive force induced on the conducting electrodes ends. The pure theoretical work conducts an analysis on this proposal computing corresponding resonance frequencies up to GHz.

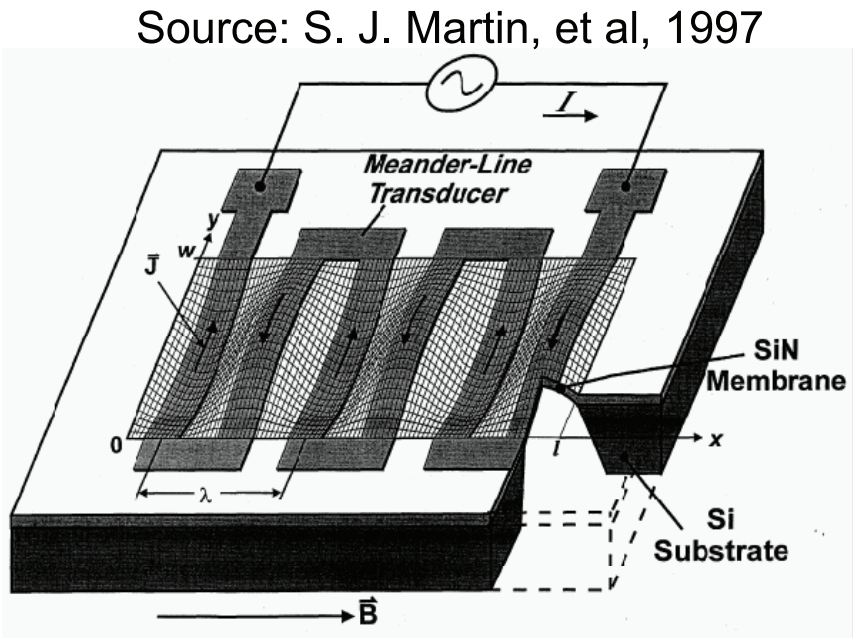

Figure 2.13: Lorentz-force transduction for flex mode resonating membrane [3]

The literature review on use of magnetic transduction for driving micromechanical resonators shows extensive work and applications. Lorentz transduction to excite SAW or bulk acoustic waves on both non-piezoelectric conductors and non-piezoelectric dielectric are reported. Research on resonant structures for sensing applications is significant. Non-contact electromagnetic excitation and detection are reported with high-Q up to 10^5. Lorentz-force transduction for developing RF micromechanical filters is also proposed in a theoretical analysis [50].

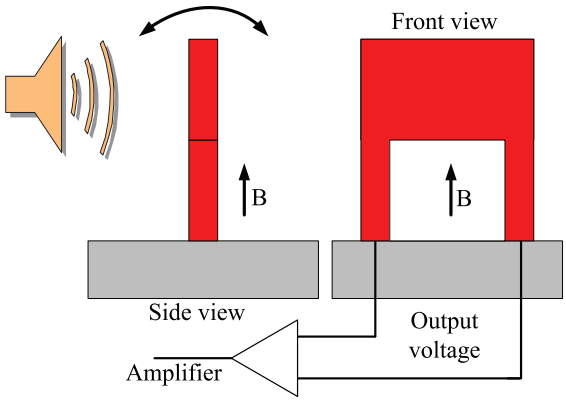

Figure 2.14: Magnetically driven micromechanical acoustic sensor

Chapter 3

Analysis of Lorentz-force Transduction for RF Filters

This chapter introduces the research method used in analyzing the electrodynamic transduction of RF micromechanical filters. Single and coupled micromechanical resonators using electrodynamic transduction are modeled. The studied inductance effect on the coupled microresonators is considered to identify whether the proposed transduction technique is limited for RF filter applications. Equivalent modeling, microstructure design for Lorentz-force transduction and design of Lorentz-force-driven multi-pole micromechanical filters, and mutual inductance effects on the performance of the coupled micromechanical resonators are the section topics in this chapter.

Electrodynamic transduction implementation requires an external magnetic field. This need does not limit the miniaturization because the external field is part of the total wireless system packaging, for example, provided by using permanent magnets. In fact, Lorentz-force-driven micromechanical resonators and filters are fabricated in CMOS technology, along with all other signal processing elements. After post processing the chips for their release, the magnetic field is provided externally by exposing the chip area, including these micromechanical resonators, in the magnetic field, as described in section 4.2.

Implementation of Lorentz-force transduction for micromechanical filters requires design and fabrication of microstructures to serve this purpose. With no need for bias lines, microstructure design for single resonators using electrodynamic transduction requires a single moving structural layer. However, in coupling

single resonators to make a filter the couplings have to be made out of a dielectric material, which is different from the resonators' electrical conducting structural material. Clamped-clamped microbeam resonators are chosen in this analysis for their ease of fabrication and because their out-of-plane vibrations are detectable by laser vibrometer. Multi-port electrical filter design techniques are employed to demonstrate the realizability of the micromechanical filters using clamped-clamped microbeams and Lorentz-force transduction.

Computation of the inductance effect on the coupled microresonators allows for evaluating whether the transduction technique is limited for the application. However, the possibility for choosing longer coupling elements allows the paralleled conducting microsturctures to be located far enough from one another. Consequently, the mutual inductance effect will be decreased proportional to the inverse of the squared distance.

The above statements are summarized. The analysis and modeling of single and coupled clamped-clamped microresonators for electrodynamic transduction are presented. The design geometries of clamped-clamped microbeams are chosen for their ease of fabrication and the characterization of their out-of-plane vibrations. The inductance effect for parallel coupled conductive resonators is studied to investigate whether the inductive coupling affect is significant enough to limit filtering application. In next the section, equivalent modeling is introduced. Equivalent modeling for the analysis of electromechanical systems is demonstrated to be a powerful technique in its simplicity and effectiveness, as well as for its ability to produce accurate results.

3.1 Equivalent modeling

Use of analogies in modeling facilitates understanding of one field of knowledge by using the language of another field. Types of analogies, electrodynamic transduction and equivalent circuit modeling, single resonators driven by Lorentz force, coupled resonators driven by Lorentz force, and computation of input excitation current as well as output induced voltage of electrodynamically driven resonators are presented.

For the fundamental analogies between mechanical and electrical systems, many concepts and equations have been interchanged between the fields [26], [51]. These

interchanges, which were initially all from mechanical to electrical and later from electrical to mechanical, are possible because the same differential equations govern electrical as well as mechanical vibrations. In the past, mechanical models were employed to explain electrical phenomenon and wave propagation. Voltage (tension), current, and resistance are examples of terms with mechanical origins. However, later, with developments in electrical engineering, electrical concepts have facilitated analyzing mechanical systems.

Use of schematic representation of electrical circuits enables engineers to visualize the performance of electrical circuits with no need to solve the corresponding differential equations. Even if differential equations are needed, deriving these equations directly from electrical circuits' schematics is more straightforward [52]. Application of electrical circuit representation for a mechanical or electromechanical system allows use of electrical concepts and theories to solve mechanical system problems. In fact, coupling characteristics of electromechanical systems and their overall performance are often better analyzed using the system equivalent electrical circuit model. A purely electrical or mechanical equivalent circuit model can be made by combining mechanical and electrical elements of an electromechanical system.

Comparing electrical differential equations for current and voltage with mechanical differential equations for force and velocity results in two applicable types of analogies [53]. Table 3.1 displays the corresponding representation of electrical and mechanical elements in these two analogies. Equations (3.1) and (3.2) show differential equations governing simple series and parallel electrical oscillators' circuits, respectively. Figure 3.1 displays schematics of the series and parallel electrical oscillators' circuits, where e, L, i, R_e, C_e are voltage, inductance, current, resistance, and capacitance.

$$e = L\frac{di}{dt} + R_e i + \int i\frac{dt}{C_e} \tag{3.1}$$

$$i = C_e\frac{de}{dt} + \frac{e}{R_e} + \int e\frac{dt}{L} \tag{3.2}$$

Figure 3.2 depicts a mechanical oscillator introduced by a parallel circuit, displayed in 3.2(a), and its two different equivalent circuit model representations, illustrated by 3.2(b) and 3.2(c). Equations (3.3) and (3.4) show the corresponding

Table 3.1: Mobility and impedance analogies

Mobility analogy		**Impedance analogy**	
Electrical	Mechanical	Electrical	Mechanical
e	v	e	F
I_e	F	I_e	v
R_e	$\frac{1}{R_M}$	R_e	R_M
C_e	M	C_e	C_M
L	C_M	L	M
Z_e	$\frac{1}{Z_M}$	Z_e	Z_M

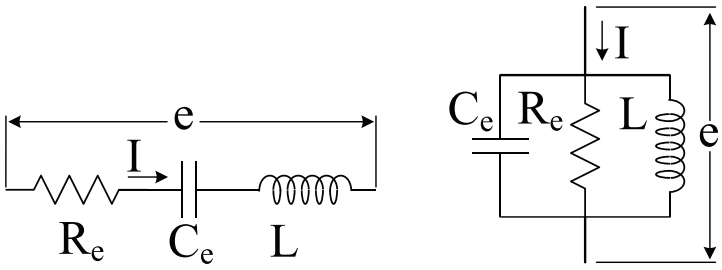

(a) Series oscillator (b) Parallel oscillator

Figure 3.1: Simple series and parallel electrical oscillator

differential equations, respectively. F, M, R_m, v, and $C_M = 1/K$ are force, mass, damping, velocity, and compliance, respectively. Adopting either of these two electrical representations requires an appropriate choice of corresponding electrical and mechanical element relationships, as displayed in 3.1.

$$F = M\frac{dv}{dt} + R_m v + \int v\frac{dt}{C_m} \tag{3.3}$$

$$v = C_m\frac{dF}{dt} + \frac{F}{R_m} + \int F\frac{dt}{M} \tag{3.4}$$

Figure 3.3 illustrates a two-port network representing a bilateral Lorentz-force or

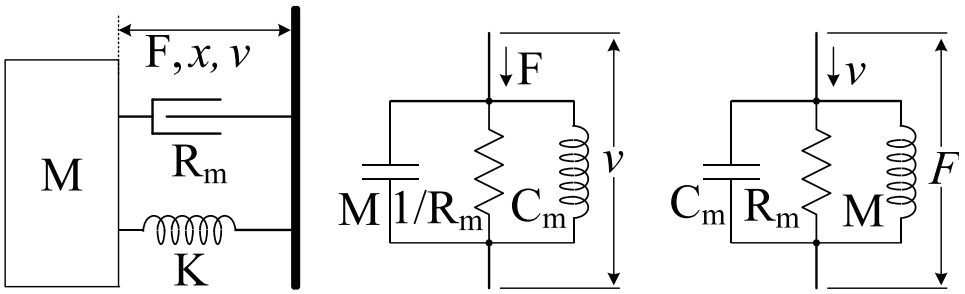

(a) Mechanical resonator (b) Mobility analogy (c) Impedance analogy

Figure 3.2: Two types of electrical representations of a mechanical oscillator

electrodynamic transducer. The network includes the source voltage on the electrical side as well as the source force on the mechanical side, e_0, F_0, and their corresponding internal impedances, Z_{e0}, Z_{m0}. The inputs to this two-port network

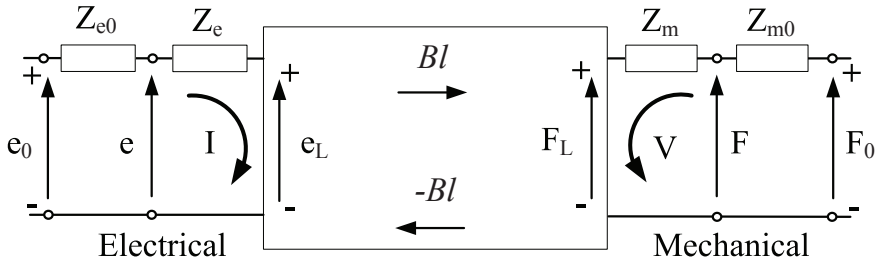

Figure 3.3: Two-port representation of an electrodynamic transducer

at a micromechanical filter's input are voltage e and current I, whereas its outputs are force F and velocity V. However, the bilateral transducer has a reverse function when used at the filter output, taking force F and velocity V as its input, outputting voltage e and current I.

A μmechanical resonator carrying current I in the presence of a crossing magnetic field B experiences Lorentz force F_L represented by (3.5).

$$F_L = I \oint (\vec{dl} \times \vec{B}) \tag{3.5}$$

Should such a microstructure resonate in the magnetic field B, an electromotive

force e_L computed by (3.6) is developed across its ends.

$$e_L = \oint (\vec{V} \times \vec{B}) \cdot \vec{dl} \tag{3.6}$$

Equations (3.7) and (3.8) display the effective input voltage and output force, respectively, where Z_e, l, and Z_m represent input electrical impedance, with the resonator being blocked ($V = 0$), resonator's length, and mechanical impedance with no electrical input (open circuit), respectively.

$$e - e_L = Z_e I \tag{3.7}$$

$$F - F_L = Z_m V \tag{3.8}$$

Assuming a uniform magnetic field B all over the conductor length (l), non-compressibility of the conductor, and with force direction perpendicular to the plane including magnetic field B and current I, the paired (3.6), (3.7) and (3.5), (3.8) reduce to (3.9) and (3.10), respectively.

$$E = -BlV + Z_e I \tag{3.9}$$

$$F = BlI + Z_m V \tag{3.10}$$

The transfer function of the Lorentz-force transducer used at a filter input is represented by (3.11). The inverse function of the electrodynamic transducer is represented by (3.12).

$$\begin{bmatrix} F \\ \\ V \end{bmatrix} = \begin{bmatrix} Bl + \dfrac{(Z_m Z_e)}{Bl} & -\dfrac{Z_m}{Bl} \\ \dfrac{Z_e}{Bl} & -\dfrac{1}{Bl} \end{bmatrix} \begin{bmatrix} I \\ \\ E \end{bmatrix} \tag{3.11}$$

$$\begin{bmatrix} I \\ \\ E \end{bmatrix} = \begin{bmatrix} \dfrac{1}{Bl} & -\dfrac{Z_m}{Bl} \\ \dfrac{Z_e}{Bl} & -(Bl + \dfrac{Z_e Z_m}{Bl}) \end{bmatrix} \begin{bmatrix} F \\ \\ V \end{bmatrix} \tag{3.12}$$

Figure 3.4 shows an equivalent circuit model for a Lorentz-force driven single resonator. Accordingly, the total input electrical impedance, Z_{et}, of the transducer

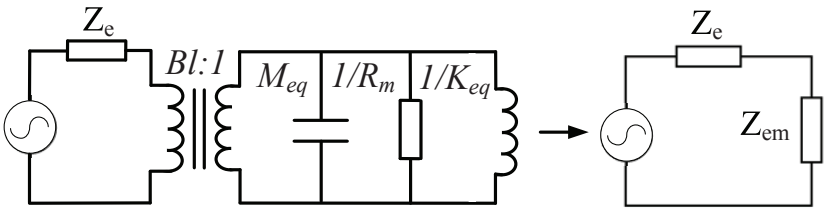

Figure 3.4: Equivalent circuit for a single Lorentz-force driven resonator

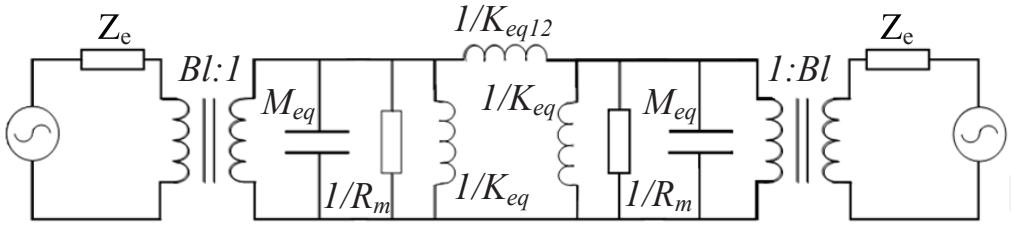

Figure 3.5: Equivalent circuit of a coupled two resonators

is computed from (3.13). Z_{em} is motional impedance due to the mechanical resonator.

$$Z_{et} = Z_e + Z_{em}, \quad Z_{em} = \frac{(Bl)^2}{Z_m} \tag{3.13}$$

At resonance, the motional impedance reduces to motional resistance R_{em}, and mechanical impedance reduces to damping R_m represented by (3.14). The mechanical damping (R_m) and motional resistance (R_{em}) at resonance for a given degree of freedom of the microresonator are computed from (3.14),

$$R_m = \frac{\sqrt{M_{eq}K_{eq}}}{Q_m}, \qquad R_{em} = \frac{(Bl)^2}{R_m} \tag{3.14}$$

where M_{eq}, K_{eq}, and Q_m are equivalent mass and stiffness, and mechanical Q, respectively [54], [5].

Figure 3.5 illustrates the equivalent circuit modeling for coupled two resonators using electrodynamic transduction. Figure 3.6 depicts the coupled two resonators' equivalent circuit model driven by Lorentz force that reduces to a pure electrical circuit at resonance.

Figure 3.7 shows an equivalent model representing the out-of-phase mode of the Lorentz-force-driven coupled two resonators. The out-of-phase mode receives

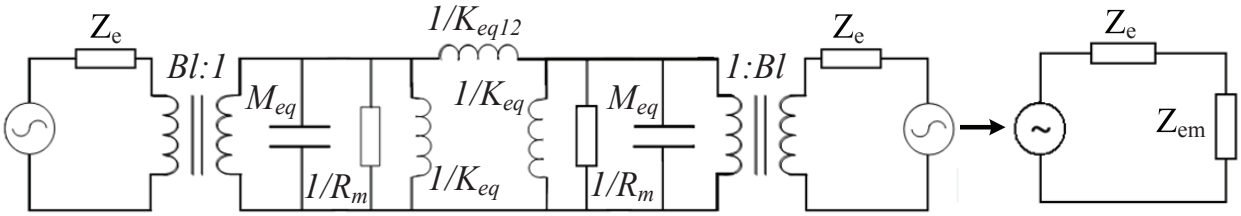

Figure 3.6: Coupled-two resonators' circuit reduces to a pure electrical equivalent

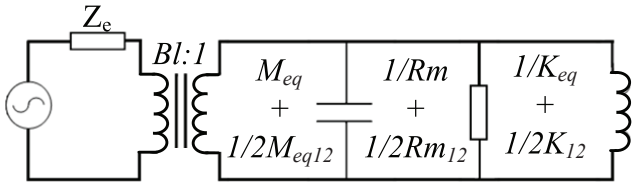

Figure 3.7: Coupled-two resonators out-phase mode's equivalent circuit

the coupling beam contributions of stiffness and mass to the resonators' mass and stiffness. Accordingly, the frequency of the out-of-phase mode is different from the original resonators' frequency where the in-phase mode of coupled two resonators has the same frequency as the resonators', regardless of the coupling.

The input excitation current I_{rms} and output sensing voltage e_{rms} of these CCμM resonators in their 1st flexural mode are computed from equations (3.15) and (3.16) [50].

$$I_{rms} = \frac{32 u_{rms}(mp) E w t^3}{Q B l^4} \tag{3.15}$$

$$e_{rms} = 3.287 l f B u_{rms}(mp) \tag{3.16}$$

The symbols $w, t, u_{rms}(mp), f$, and Q_m represent μresonator width, thickness, mid-point displacement, resonance frequency, and quality factor.

For the arrangement illustrated in 3.8, the computation of induced voltage magnitude, e_{ind}, is from Faraday's law, as displayed in (3.17). $u(x,t)$ and $\overline{v}(t)$ are beam displacement and average velocity, respectively [50].

$$e_{ind} = \frac{\partial \Phi_B}{\partial t} = B \int_0^l \frac{\partial u(x,t)}{\partial t} dx = Bl\ \overline{v}(t), \quad \text{where} \quad \overline{v}(t) = \frac{1}{l} \int_0^l \frac{\partial u(x,t)}{\partial t} dx \tag{3.17}$$

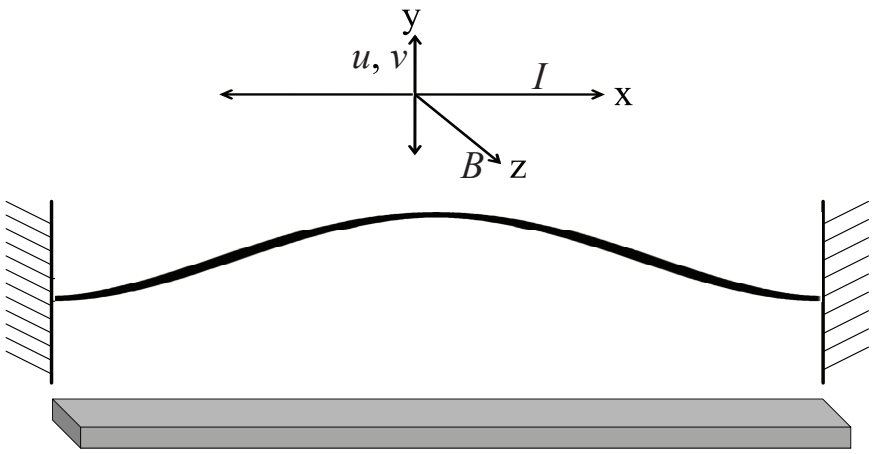

Figure 3.8: Out-of-plane move of a Lorentz-force driven fixed-fixed microbeam

If $F = F_0 \cos(\omega t)$, $u(x,t)$ is computed from (3.18),

$$u(x,t) = u(x)e^{j\omega t} \tag{3.18}$$

where $u(x)$ is given in (3.23) and can be approximated by (3.19) from which (3.16) is derived [55]. $u\ (mp)$ is the clamped-clamped beam midpoint maximum displacement.

$$u(x) = \frac{u\ (mp)}{2}\left(1 - \cos(\frac{2\pi x}{l})\right) \tag{3.19}$$

3.2 Microstructure design and multi-pole micromechanical filters

Clamped-clamped microbeam single and coupled resonators are chosen for investigating Lorentz-force transduction. These microstructures are driven out-of-plane should they experience in-plane magnetic field crossing the electrical current through their length. Out-of-plane motions of microresonators allow for characterization of their mechanical vibrations using a laser vibrometer. The design of

microresonators and the realization process of two-pole and three-pole micromechanical filters are demonstrated.

The resonance frequency of a clamped-clamped beam corresponding to its 1st flexural mode is computed by (3.20) [56], [54].

$$f_{res} = \frac{(Cl)^2 t}{4\pi\sqrt{3}l^2}\sqrt{\frac{E}{\rho}}\left(1 + \frac{12\sigma l^2}{t^2\gamma 1 E}\right), \qquad \gamma 1 = 38.56 \tag{3.20}$$

$$M_{eq}(x) = \frac{E_K}{(\frac{1}{2})v(x)^2} = \frac{\rho w t \int_0^l u(x')^2 dx'}{u(x)^2} \tag{3.21}$$

$$K_{eq}(x) = (2\pi f)^2 M_{eq}(x) \tag{3.22}$$

where

$$u(x) = \cosh(Cx) - \cos(Cx) - \eta\left(\sinh(Cx) - \sin(Cx)\right), \qquad C = \frac{4.73}{l},\ \eta = \frac{\cosh(Cl) - \cos(Cl)}{\sinh(Cl) - \sin(Cl)} = 0.9825 \tag{3.23}$$

The equivalent mass and stiffness of a clamped-clamped microresonator whose 1st flexural resonance frequency is f are computed from (3.21) and (3.22), respectively [5]. $M_{eq}(x)$, E_K, v, E, ρ, w, t, σ, and u represent the equivalent mass at location x along the beam length, total kinetic energy, velocity, Young modulus, mass density, width, thickness, residual stress, and mode shape, respectively. Figure 3.9 displays the 3rd, 5th, 7th, and 9th mode shapes of a 90 micron length clamped-clamped beam.

Although flexural resonance modes of the beams are not the only modes that can be employed for micromechanical filters, a frequency scaling computation can show the effects of dimension change on the frequency. A frequency scaling relationship can also demonstrate the requirements for physical dimensions of a flexural beam when frequency increases to a higher range of RF applications. Accordingly, from (3.20) and by assuming σ is negligible, the resonance frequency of a beam in flexural modes is given in (3.24).

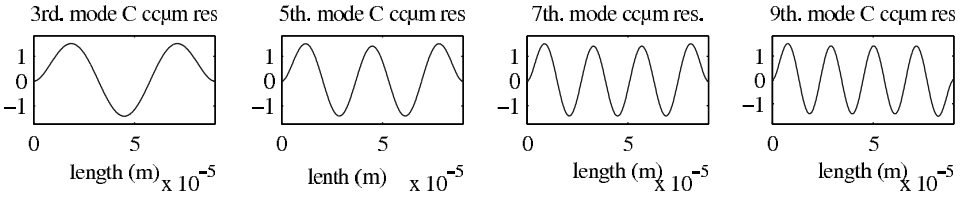

(a) 3rd mode (b) 5th mode (c) 7th mode (d) 9th mode

Figure 3.9: 3rd, 5th, 7th, & 9th mode shapes of a 90-μm CCμM resonator

The relative change of frequency over relative variation of the beam dimensions is computed by taking the logarithm from both sides of (3.24) as displayed in (3.25). Differentiating on both sides of (3.25) results in (3.26). Equation (3.26) shows that the relative change in frequency is proportional to the relative change in thickness if a microbeam's length is constant. The relative change of frequency also inversely depends on the two times of the relative length variation if the thickness remains constant. For example, C resonating at about 2.3 MHz with a length and thickness of 90 μm and 3.28 μm would require a length of about 9 μm to resonate at 230 MHz with the same thickness.

$$f = \frac{(Cl)^2 t}{4\pi\sqrt{3}l^2}\sqrt{\frac{E}{\rho}} \tag{3.24}$$

$$\log(f) = \log((Cl)^2) + \log(t) - \log(4\pi\sqrt{3}) - 2\log(l) + \log(\sqrt{\frac{E}{\rho}}) \tag{3.25}$$

$$\frac{df}{f} = \frac{dt}{t} - 2\frac{dl}{l} \tag{3.26}$$

The scalability of the transduction technique for higher frequency is estimated by an analysis of the relative change of the motional resistance with respect to relative change of frequency. To serve this purpose, the relative change of both quantities are derived using (3.14) and (3.22).

$$\log(R_{em}) = 2\log(B) + 2\log(l) - \log(R_m) \Rightarrow \tag{3.27}$$

$$\frac{d(R_{em})}{R_{em}} = 2\frac{d(B)}{B} + 2\frac{d(l)}{l} - \frac{d(R_m)}{R_m} \tag{3.28}$$

$$\log(R_m) = 0.5\log(M_{eq}) + 0.5\log(K_{eq}) - \log(Q_m) \Rightarrow \tag{3.29}$$

$$\frac{d(R_m)}{R_m} = 0.5\frac{d(M_{eq})}{M_{eq}} + 0.5\frac{d(K_{eq})}{K_{eq}} - \frac{d(Q_m)}{Q_m}, \tag{3.30}$$

$$\frac{d(R_{em})}{R_{em}} = 2\frac{d(B)}{B} + 2\frac{d(l)}{l} - 0.5\frac{d(M_{eq})}{M_{eq}} - 0.5\frac{d(K_{eq})}{K_{eq}} + \frac{d(Q_m)}{Q_m} \tag{3.31}$$

$$\log(K_{eq}) = 2\log(2\pi f) + \log(M_{eq}),\ \frac{d(K_{eq})}{K_{eq}} = 2\frac{d(f)}{f} + \frac{d(M_{eq})}{M_{eq}} \Rightarrow \tag{3.32}$$

$$\frac{d(f)}{f} = \frac{1}{2}\left(\frac{d(K_{eq})}{K_{eq}} - \frac{d(M_{eq})}{M_{eq}}\right) \tag{3.33}$$

From (3.31) and (3.33) and assuming B is constant, relative change is computed by (3.34).

$$\left(\frac{d(R_{em})}{R_{em}}\right) / \left(\frac{d(f)}{f}\right) =$$
$$\left(4\frac{d(l)}{l} - \frac{d(M_{eq})}{M_{eq}} - \frac{d(K_{eq})}{K_{eq}} + 2\frac{d(Q_m)}{Q_m}\right) / \left(\frac{d(K_{eq})}{K_{eq}} - \frac{d(M_{eq})}{M_{eq}}\right) \tag{3.34}$$

Aiming at higher frequency results in scaling down of the resonators' volume for which mass (M_{eq}) is scaled to S^{-3} where S is a length scale [55]. However, the stiffness (K_{eq}) scales with the scaled strength of the material, which is S^{-2}. Therefore, the relative change of M_{eq} is higher than K_{eq}, with both terms being present in the numerator and denominator of (3.34). The relative change of l ($d(l)/l$) depends on the geometry of the design. For example, a higher frequency CCμM resonator requires a shorter l; however, if the resonator is a ring or disk, the l, which is the circumference of the ring or disk, can be longer even for a higher frequency. Accordingly, (3.34) does not show a dramatic change of motional resistance as the frequency scales up. Continuation of the experimental work will illuminate more aspects of the transduction technique.

The requirement for an external magnetic field in implementation of Lorentz-force transduction is discussed to study whether it poses a limitation for the application. In fact, the requirement for this external field does not add any limitation

to prevent the miniaturization because the external field can be provided as part of the total wireless system packaging, for example, by using permanent magnets. In fact, Lorentz-force driven micromechanical resonators and filters can be fabricated in the CMOS technology, for instance, along with all the other signal processing elements and then post processed for their release; the magnetic field is provided externally by exposing the chip area, including these micromechanical resonators in the magnetic field.

Figure 3.10 shows three possible scenarios for providing out-of-plane and in-plane magnetic fields for in-plane and out-of-plane vibrating micromechanical resonators, respectively. A single or double permanent magnet of less than a few-square-millimeter surface size are included in the body of the transceiver to be held in the proximity of the resonators as shown in 3.10. Such an arrangement can produce a uniform magnetic field of about 0.5-0.8 Tesla at a distance not exceeding about one millimeter above the magnet surface by using Neodymium magnets. A gap of about 5 to 6 millimeters between two magnets when using a two-magnet configuration can still produce the above mentioned magnetic field intensity, given that the two magnets are connected by a ferromagnetic tape to create a magnetic circuit. Other options are also achievable. For example, a magnetic circuit can be made using a permanent magnet and ferromagnetic tapes to lead the field to the area of micromechanical resonators, as shown in 3.10. The tapes and permanent magnet are incorporated in the body of the transceiver. In this configuration, the permanent magnet does not even need to be close to the micromechanical resonators on the chip where the gap between tape tips produces the required magnetic field.

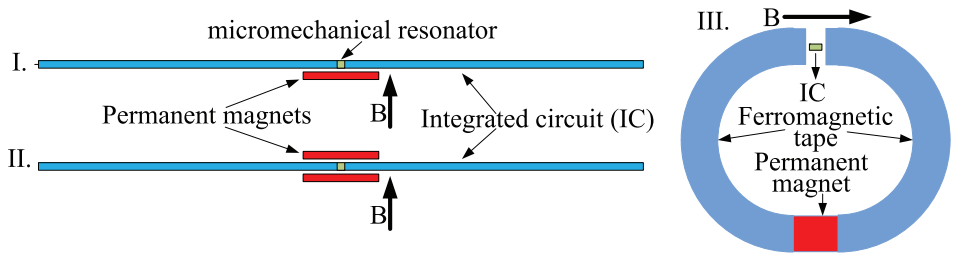

Figure 3.10: External magnetic field for Lorentz-force transduction

The conventional approach in designing a multi-pole electrical filter is applicable in the design of a mechanical filter for electrical filtering too. However, in realization of the multi-pole mechanical filter, the application of the coupling matrix elements to determine mechanical coupling specifications requires further compu-

tations. These computations are also applicable to the identification of the filter's input/output coupling. The mechanical elements' specifications include the dimensions by which the demanded resonators' frequency is provided, coupling locations, coupling length, and coupling material [57], [5]. The micromechanical filter design and realization procedure are adapted for electrodynamic transduction.

For a given filter's response, the design and synthesis of the corresponding multi-pole filter involve the following steps. The filter's response is represented by $S-$parameters, insertion loss, and return loss that are derived from (3.35), (3.36), (3.38), and (3.39), respectively. R_f, I_f, and M_f are $n \times n$ matrices: All elements of R are zero except $[R_f]_{11} = R_1$ and $[R_f]_{nn} = R_n$. R_1 and R_n are filter's input and output coupling, respectively. M_f is a symmetric coupling matrix. I_f is an identity matrix. λ is computed from (3.37), where f_0, f, and BW are the filter center frequency, incoming signal frequency, and filter's bandwidth, respectively. Step one in filter design is to compute the coupling matrix, M_f, and R_f, which includes normalized input/output couplings of the filter. Step two in filter design is the realization stage by which the mechanical resonators' and couplings' specifications are calculated [57], [19].

The insertion loss method is employed in step one to compute the coupling matrix. The normalized g-values corresponding to the Chebychev filter's required insertion loss or pass band ripple level are either taken from filter synthesis handbooks or computed as shown in Appendix B. Elements of the coupling matrix, the M_f, and R_f-matrix, are computed from 3.40 and 3.41, using normalized $g_0, g_1, g_2, ..., g_{n+1}$ [57], [19].

$$S_{11} = 1 + 2jR_1[\lambda I_f - jR_f + M_f]^{-1}_{11} \tag{3.35}$$

$$S_{21} = -2j\sqrt{R_1 R_n}[\lambda I_f - jR_f + M_f]^{-1}_{n1} \tag{3.36}$$

$$\lambda = \frac{f_0}{BW}\left(\frac{f}{f_0} - \frac{f_0}{f}\right) \tag{3.37}$$

$$RL = -20\log|S_{11}| \tag{3.38}$$

$$IL = -20\log|S_{21}| \tag{3.39}$$

$$m_{q,q+1} = \frac{1}{\sqrt{g_q g_{q+1}}}, \ (q = 1, 2, ..., n-1) \tag{3.40}$$

$$R_1 = \frac{1}{g_0 g_1}, \quad R_n = \frac{1}{g_n g_{n+1}} \tag{3.41}$$

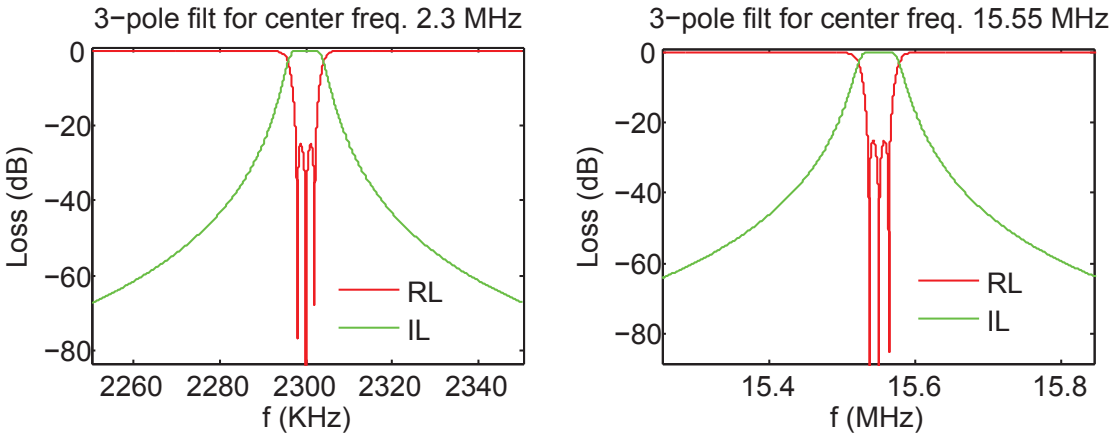

Figure 3.11: 3-pole filter response for center freq. of 2.3 MHz and 15.55 MHz

To demonstrate the realization process in the design of a multi-pole filter, some numerical values are assumed: a 25 dB insertion loss and a filter Q_{filt} of 500. The center frequencies are chosen to the extent that their characterization is achievable using a laser vibrometer. Accordingly, the coupling matrices and input/output coupling coefficients for three-pole (3p) and two-pole (2p) electrical filters are computed by 3.42 and 3.43, respectively. Figures 3.11 and 3.12 display three- and two-pole filter responses for the center frequencies of 2.3 MHz and 15.55 MHz, respectively, using the above-mentioned computation results.

$$M_f\ (2p) = \begin{bmatrix} 0 & 2.1670 \\ 2.1670 & 0 \end{bmatrix}, \qquad R1 = 2.0483,\ R2 = 2.0483 \tag{3.42}$$

$$M_f\ (3p) = \begin{bmatrix} 0 & 1.2197 & 0 \\ 1.2197 & 0 & 1.2197 \\ 0 & 1.2197 & 0 \end{bmatrix}, \qquad R1 = 1.4918,\ R3 = 1.4918 \tag{3.43}$$

Step two is micromechanical filter realization: calculating the filters mechanical resonators' and couplings' specifications based on the coupling matrices and input/output coupling coefficients computed in the previous step. For coupled clamped-clamped microresonators, specifications of the resonators, their coupling dimensions, and coupling locations are needed and are computed in two stages :

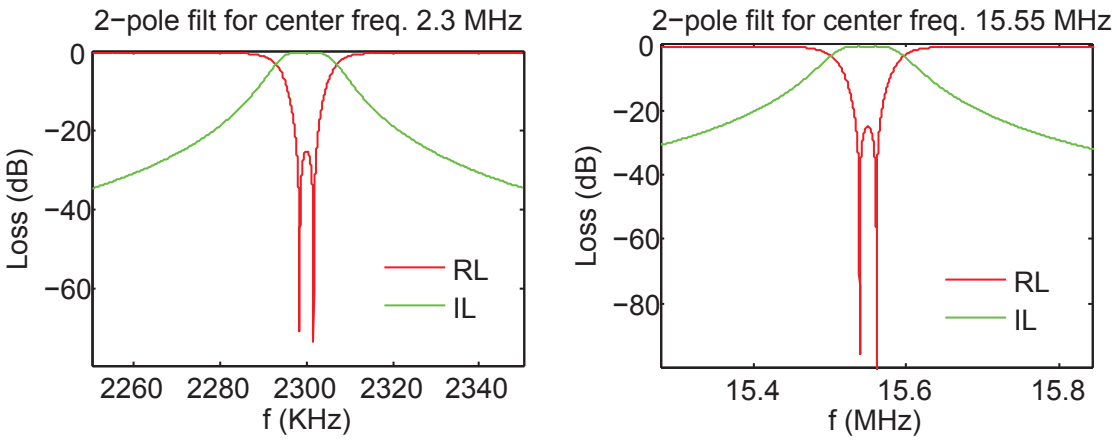

Figure 3.12: 2-pole filter response for center freq. of 2.3 MHz and 15.55 MHz

first, the mechanical resonators' dimensions are computed. Second, the resonators' inter-couplings as well as the couplings' locations are derived [5].

However, the design process requires a reiteration approach going forward and backward in choosing mechanical dimensions of the resonators, couplings, and coupling locations. Using the calculated data, the performance of the filter for the chosen dimensions is simulated to see if it is realizable and whether it satisfies other requirements. This reiteration process continues to reach an optimized final design. For example, microfabrication limitations only allow a certain minimum feature size, limited minimum distance between features, and limited options for material selections. After deriving a given dimension for the coupling beam that satisfies all corresponding equations and provides the filter with the required performance, one also needs to check whether the resonance frequency of the coupling beam for the given dimensions, for example, are out of the filter's pass band.

For the first stage in step two of filter realization 3.2, the dimensions of the individual mechanical resonators are chosen in order that their computed resonance frequency is the filter center frequency. For the coupled clamped-clamped micromechanical resonators in their flexural modes, the resonance frequency, which is the filter center frequency, is computed from (3.20). However, calculations for the couplings' locations and the couplings' dimensions involve a more complicated process.

In designing conventional macroscale mechanical filters, the stiffness of the coupling wires or beams can be chosen to be small enough compared to the resonators'

stiffness to address the narrow band pass filters' requirement. However, the stiffness of couplings and resonators in microscale are relatively close to one another. The limited feature size and distance between features because of microfabrication difficulties results in relatively close stiffness of resonators and couplings. In the design of a narrow band pass filter, the relative stiffness of resonators and coupling need to large enough. To overcome this limitation, the coupling locations are chosen in order that the equivalent stiffnesses of the resonators are significantly higher than the ones of the couplings. Following this approach, the computations for the coupling dimensions and coupling locations are explained [5], [26].

A two-port equivalent circuit can represent a coupling beam connecting two flexural mode vibrating clamped-clamped mechanical resonators. Figure 3.13 illustrates the two-port representation for a coupling beam having flexural motion. Equation 3.44 shows this two-port representation in matrix form, where F_1 , v_1 , F_2 , v_2 , f , K_c , $C_c l_c$, C_c , l_c , E_c , I_c, w_c , t_c , ρ_c , and A_c are the coupling beam's input force, input velocity, output force, output velocity, frequency, bending stiffness, propagation constant, dispersion, length, Young's modulus, bending moment, width, thickness, density, and cross-section area. For the first flexural mode, $C_c l_c$ is 4.730. Equations 3.47 and 3.48 represent $Y_{a(mn)}$ and $Y_{b(mn)}$ that are shunt and series arm mechanical impedances, respectively. The representations are valid when the coupling beam acts as a quarter-wavelength line where $Y_{a(mn)} = -Y_{b(mn)}$ [5], [26].

For the beam's 1st flex mode ($Cl = 4.730$) and regarding the beam's structural material of $SiO2$, the coupling length is derived by 3.46. Using computed l_c, shunt and series arm mechanical impedances, $Y_{a(mn)}$ and $Y_{b(mn)}$, are calculated from 3.47 and 3.48, respectively. Inserting the computed value for shunt arm mechanical impedance in 3.49, the coupling beam stiffness Kc_{mn} is calculated, where m and n refer to the corresponding resonators being connected by the coupling beam. After these computations, it would be helpful to calculate the resonance frequencies $fp(p)$ (parasitic modes) of the coupling beam from 3.50 to make sure the modes are far enough away from the filter's pass band.

The required resonators' stiffness $K_{eq}(i)$ is calculated from 3.51 where $M(m, n)$ is the coupling matrix elements computed by 3.42 and 3.43, and $Q_{filt} = f/BW$ is the filter's Q. The corresponding equivalent mass of the resonator is computed from 3.22. Solving 3.52 by inserting the computed value for equivalent mass from 3.22 results in derivation of the coupling location(s), which are the roots of 3.52 for

locations on the clamped-clamped micromechanical resonators. Where i in $K_{eq}(i)$ and $M_{eq}(i)$ designates the corresponding resonator, ρ_{comb} , A_r , and E_k are the resonators' density, cross section, and kinetic energy, respectively. ρ_{comb} or ρ represents the equivalent or combined density of the resonator consisting of stack of layers of different materials. Having the coupling beam length, thickness, width, and the resonators location to which the coupling is connected, the coupling beam computations stage in the realization step is complete [5].

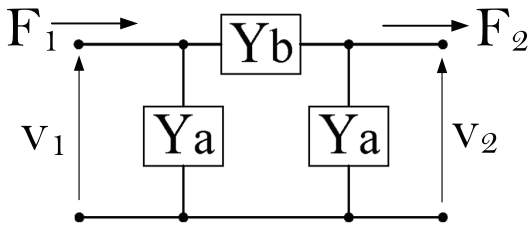

Figure 3.13: A two-port representation of a coupling beam

$$\begin{bmatrix} v_1 \\ \\ F_1 \end{bmatrix} = \begin{bmatrix} 0 & j\left(\dfrac{2\pi f l_c^3\left(\sinh(a)+\sin(a)\right)}{2(C_c l_c)^3 K_c\left(\sinh(a)\sin(a)\right)}\right) \\ j\left(\dfrac{2(C_c l_c)^3 K_c\left(\sinh(a)\sin(a)\right)}{2\pi f l_c^3\left(\sinh(a)+\sin(a)\right)}\right) & 0 \end{bmatrix} \begin{bmatrix} v_2 \\ \\ F_2 \end{bmatrix} \tag{3.44}$$

$$\cos\left(C_c l_c\right)\cosh\left(C_c l_c\right) - 1 = 0 \tag{3.45}$$

$$K_c = E_c I_c = \frac{E_c w_c t_c^3}{12}, \quad l_c = \frac{C_c l_c}{C_c} = \frac{\sqrt[4]{\frac{\rho_c A_c (2\pi f)^2 l_c^4}{E_c I_c}}}{\sqrt[4]{\frac{\rho_c A_c (2\pi f)^2}{E_c I_c}}} \tag{3.46}$$

$$Ya = \left(\frac{K_c (C_c l_c)^3\left(\sinh(a)+\sin(a)\right)}{j\omega l_c^3\left(\cosh(a)\cos(a)-1\right)}\right) \tag{3.47}$$

$$Yb = \left(\frac{jK_c (C_c l_c)^3\left(\sinh(a)+\sin(a)\right)}{j\omega l_c^3\left(\cosh(a)\cos(a)-1\right)}\right) \tag{3.48}$$

$$Kc_{mn} = Yb(2j\pi f) \tag{3.49}$$

$$fp(p) = \frac{C_c l_c(p)^2}{2\pi l_c^2}\sqrt{\frac{E_c I_c}{\rho_c A_c}} \tag{3.50}$$

$$K_{eq}(i) = Q_{filt}\frac{Kc_{mn}}{M(m,n)} \tag{3.51}$$

$$M_{eq}(i) = \frac{\rho_{comb} A_r E_k}{\left(\cosh(Cu) - \cos(Cu) - Zeta\left(\sinh(Cu) - \sin(Cu)\right)\right)^2} \tag{3.52}$$

$$Zeta = \frac{\cosh(Cl) - \cos(Cl)}{\sinh(Cl) - \sin(Cl)} = 0.9825, \qquad E_k = \int_0^l \left(u(x)^2 dx\right)$$

Proper termination impedance values are required to flatten the pass band for the coupled microresonators function as a filter; otherwise, the resonators' Q_m are too large for and the filter pass band consists of two distinct peaks. In fact, employing the proper termination impedances decreases the end resonators' Q_m. To derive the required input and output couplings, $R_Q(i)$, the normalized values for $R1$ and $R2$ from 3.42 for the two-pole filter or $R1$ and $R3$ from 3.43 for the three-pole filter are inserted in 3.53, where R_i is either $R1$ or $R2$ of the two-pole filter or $R1$ or $R3$ of the three-pole filter. Q_m and R_{em} are resonators' Q and motional resistance computed in 3.14 [4].

$$R_Q(i) = \left(\frac{Q_m}{R_i Q_{filt}} - 1\right) R_{em} \tag{3.53}$$

3.3 Mutual inductance effect

Coupled microresonators using electrodynamic transduction involve parallel conducting structures that are separated by the coupling beam length. The proximity of these parallel conductors, each connected to either input or output, causes a cross-talk between input and output, which is undesirable. The significance of this effect are evaluated, from which an estimation of the relative magnitude of the picked up signal with respect to the induced voltage is obtained. The induced voltage is by Lorentz force for the moving microstructure in the magnetic field where

the picked-up voltage is by the mutual inductance effect.

Mutual inductance occurs when the change in current in one inductor induces a voltage in another nearby inductor. The mutual inductance is a measure of the electrical coupling between the two inductors. When this effect is the fundamental operation principle of transformers, mutual inductance in the use of Lorentz-force transduction for RF micromechanical filters can cause unwanted coupling between filter input and output.

The mutual inductance by circuit 1 on circuit 2, Mi_{12}, is given by the double integral Neumann formula by (3.54) where μ_0 , dl_1 , dl_2 , and g_{12} are free space permeability, length element of the circuit 1, length element of the circuit 2, and the gap between two circuits. Equation (3.54) reduces to 3.55 for the coupled two clamped-clamped microbeams displayed in layouts of 4.7 and 4.8. Figure 3.14 depicts δ variation that is computed numerically and is a function of the relative coupling length (l_c) over the resonators' length (l) [4].

The picked up signal as a result of the inductance between the two parallel conducting microresonators is calculated by 3.56, where I_{rms} is derived by 3.15. The relative magnitudes of the two voltages, $S2N_{rel}$, the induced electromotive force e_{rms} 3.15 and the picked-up voltage 3.56 due to the mutual inductance of the two parallel conducting resonators, is computed by 3.57 [4].

$$Mi_{12} = \frac{\mu_0}{4\pi} \oint_1 \oint_2 \frac{d\vec{l}_1 . d\vec{l}_2}{g_{12}} \tag{3.54}$$

$$Mi_{12} = \frac{\mu_0}{4\pi} l\delta \left(\frac{l_c}{l} \right) \tag{3.55}$$

$$e_{rms}(picked - up) = -Mi_{12} \frac{dI_{rms}}{dt} = \frac{\mu_0}{4\pi} l\delta \left(\frac{l_c}{l} \right) \frac{dI_{rms}}{dt} \tag{3.56}$$

$$S2N_{rel} = \frac{e_{rms}}{e_{rms}(picked - up)} \tag{3.57}$$

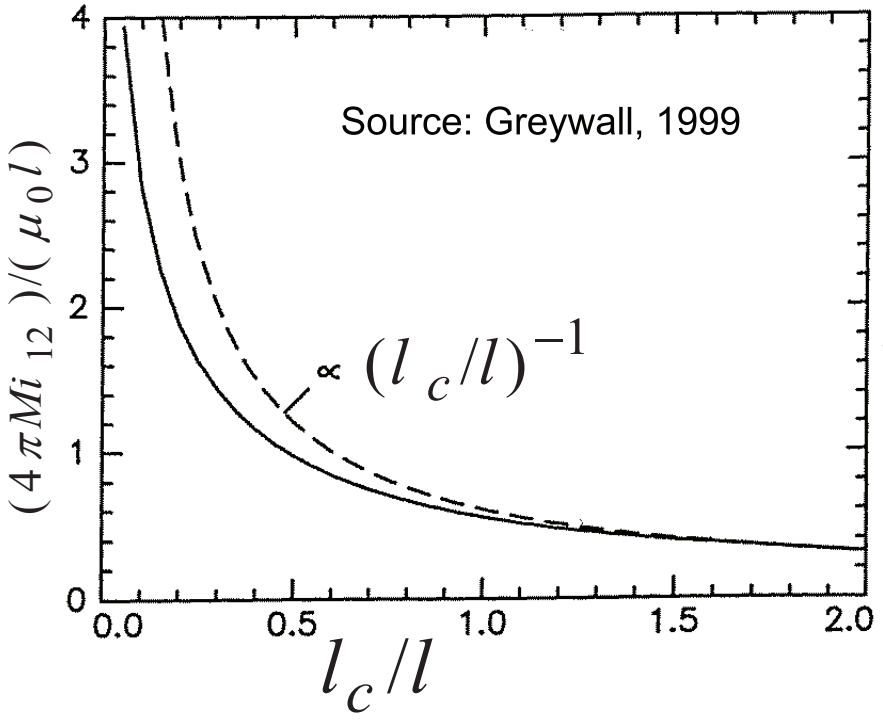

Figure 3.14: Mutual inductance between two coupled microresonators 4.8 [4]

Chapter 4

Microfabrication and Experimental Studies

This chapter reports my experimental results on using electrodynamic transduction for RF micromechanical filters. In implementing Lorentz-force transduction, microstructures are designed, fabricated, and fixed on test fixtures for experimental evaluation. The experimental evaluation of these fabricated designs requires driving the microstructures by electrical signals at a wide spectrum and measuring the response of the microresonators. Mechanical vibrations of the microstructures as well as their electrical behavior are measured and recorded. Microfabrication and the experimental setup, mechanical motion measurements, and electrical characterizations are described and the measurement results are reported.

Microfabrication of clamped-clamped beams in various technologies allow for studying the performance of Lorentz-force driven microresonators made of different structural materials. Choosing a geometry of clamped-clamped beams for implementing single and coupled microresonators is done for ease of experimental measurements. Such simple designs are less complicated to fabricate. Measuring out-of-plane mechanical vibrations of these microstructures by laser vibrometer is also more straightforward. The corresponding fabrication technologies are briefly introduced in section 4.1. The engineering design, layout preparation, and fabrication are also described in section 4.1, as are Some designs, such as the ones implemented in CMOS35, that require post-processing. The specifications of the single and coupled resonators fabricated using these technologies are summarized in 4.1 and 4.2, respectively.

A significant post-fabrication effort is a requirement in the preparation of the fabricated designs' chips for measurements. Section 4.1 describes this part of the experimental work. A mini-vacuum chamber that is described in section 4.1 is the main and the most effective experimental tool in all these measurements. The mini-vacuum chamber was designed by myself and fabricated under my supervision.

The out-of-plane motions of various points on a vibrating microstructures are measurable by a laser vibrometer. The operating principle of this detection technique is Doppler effect, which has been extensively employed in different applications to measure the relative velocity and displacement of a moving object. By detecting the performance of every point on a web pattern defined on the moving microstructure, the mode shapes of the resonating microstructure are detectable. In the "mechanical measurements," section 4.2, identifying mode shapes, resonance frequencies, quality factors, and overall mechanical performance of the fabricated microstructures are reported. These measurements are achieved both in air and vacuum.

Electrical characterization of single and coupled microresonators involves using a Vector Network Analyzer (VNA). Single port measurements on single resonators and two-port measurements are conducted on coupled microresonators. With no application of bias current or voltage, the measured electrical response of a Lorenz force driven resonator is the voltage produced at the resonator's terminal displaying the sharp change of motional resistance. However, these microvolt amplitude voltages, as shown in the results 4.1, require amplification for the corresponding application. Section 4.3 reports the electrical measurements displaying motional resistance changes, the electromotive forces produced by electrodynamic transduction, and allows for comparing the results with the mechanical measurements by laser vibrometer.

Reporting experimental results in this chapter will provide readers with the examining results of the research method presented in Chapter 3, to verify the equivalent model representation, and to demonstrate the feasibility of electrodynamic transduction implemented for RF micromechanical filters. Using two different measurement techniques of mechanical vibration detection by laser vibrometer and electrical characterization by standard RF measurement tools (VNA) enhances the certainty of the research work and allows results to be compared. The following sections provide a detailed report of the experimental work and obtained results.

4.1 Microfabrication and experimental setup

The design of single clamped-clamped microbeam resonators for a given frequency and a detailed analysis on the use of coupled clamped-clamped resonators serving as a multi-pole filter are provided in section 3.2. In this section, single and coupled resonators fabricated in a few different microfabrication technologies based on the analysis given in section 3.2 are reported. Further to ease of fabrication, clamped-clamped microbeams are chosen for their out-of-plane resonating that allows for mechanical measurements by laser vibrometer, described in section 4.2. Features of the microfabrication technologies, SEMs and layouts of the fabricated designs of the single and coupled microresonators, and experimental setup are described.

Figure 4.1 displays an overview of the fabrication processes for UW-MEMS, PolyMUMPs, and CMOS35. Figure 4.2 shows the measurement setup and SEMs of four single clamped-clamped micromechanical resonators, labeled C, P, U1, and U2, that are fabricated in CMOS35 , PolyMUMPs , and UW-MEMS, respectively. C designates the design implemented in CMOS35; P is the design in PolyMUMPs; and U1 and U2 fabricated in UW-MEMS.

In CMOS35, the resonators are made of a stack of four layers: $Al(1\mu m)$ + $Sio2(0.64\mu m)$ + $Al(1\mu m)$ + $Sio2(0.64\mu m)$ [58]. In PolyMUMPs, the only design reported in this work is P making use of Poly2 layer with gold deposited on top [59]. In UW-MEMS, the single gold layer G2 is the only layer released after fabrication [60]. The designs of single and coupled resonators implemented in UW-MEMS make use of G2 for the moving part of the clamped-clamped resonators where the microbeams ends are anchored to the substrate.

Single resonators are fabricated for their out-of-plane flexural modes. Figure 4.3 displays schematics of the first flexural mode and the setup in which a $90\mu m$ clamped-clamped micromechanical resonator is driven by Lorentz force. The magnetic field is in-plane and perpendicular to the microbeam length.

Resonator C is 90 μm long, 10 μm wide, and 3.28 μm thick fixed-fixed beam, using a stack of four layers, $Al(1\mu m) + Sio2(0.64\mu m) + Al(1\mu m) + Sio2(0.64\mu m)$. Resonator P is made of $P2 + Gold$ layers, 40 μm long, 13 μm wide, and 2.02 μm thick. Resonators U1 and U2 are made of the single layer of gold G2 whose thickness and width for these two designs are $1.25\mu m$ and $55\mu m$, respectively. The beam length for U1 and U2 are $80\mu m$ and $280\mu m$, respectively. Resonators C and P do

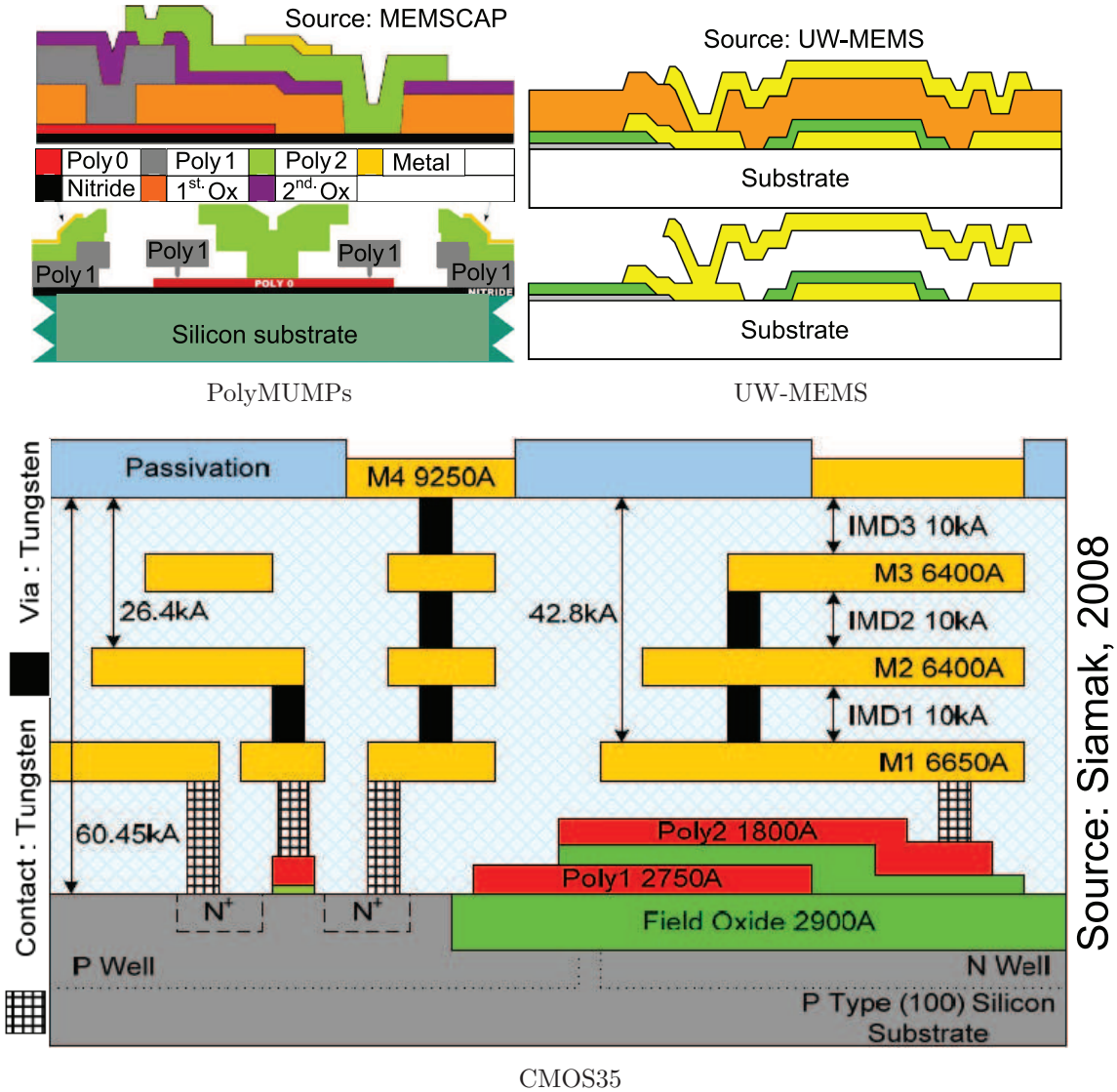

Figure 4.1: Fabrication process of PolyMUMPs, UW-MEMS, and CMOS35

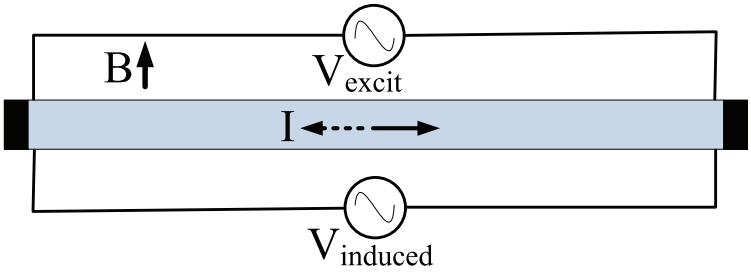

(a) Measuring setup

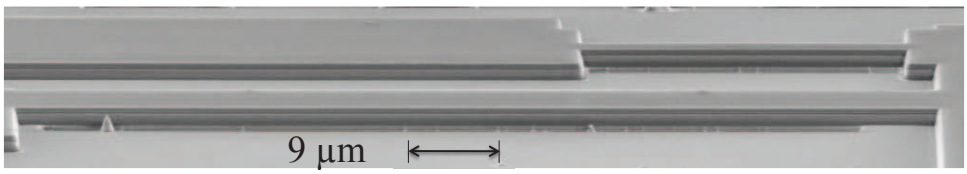

(b) CMOS35 design (C)

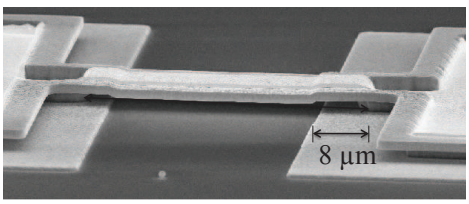

(c) PolyMUMPs design (P)

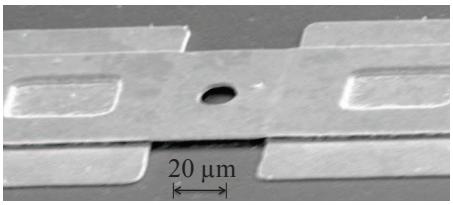

(d) UW-MEMS design (U1)

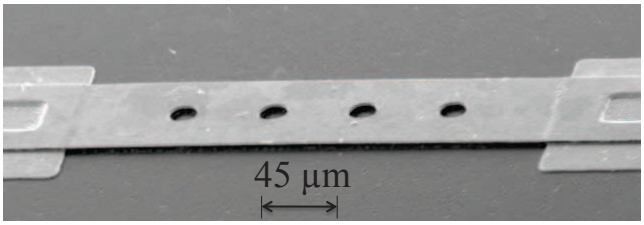

(e) UW-MEMS design (U2)

Figure 4.2: Measurement setup and C, P, U1, and U2

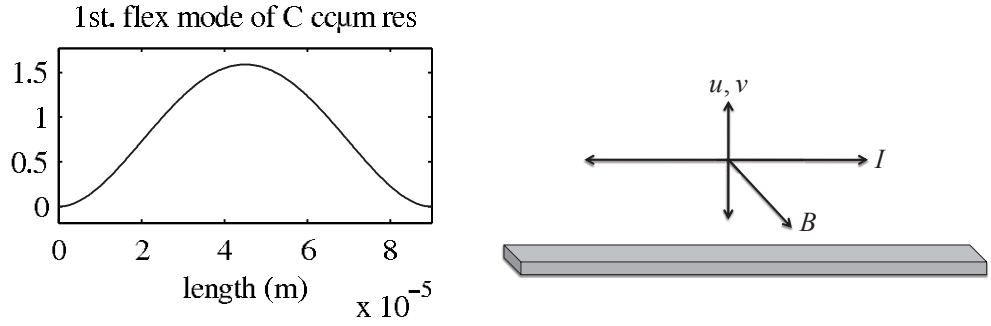

(a) CCμMR 1st. mode (b) Lorentz-force driving

Figure 4.3: Schematics displaying out-of-plane move of a CCμMR

not include etch holes because of their smaller width. However, U1 and U2 have etch holes for their width of $55\mu m$. The effect of etch holes and a larger beam-width-to-length ratio, which affects use of beam theory to compute the resonance frequency, are accounted for by deriving an effective Young modulus (E^*). Use of a stack of multiple different structural layers in the fabrication of microresonators as for C and P requires computations for an effective value of ρ^* , E^* , and σ^* . The specifications of the four single resonators are summarized in 4.1.

The coupled resonators displayed in 4.21 are fabricated by UW-MEMS. The resonators and coupling are made of the same structure layer as G2. Therefore, the coupled resonators are not electrically isolated. However, fabrication of such coupled resonators allows for mechanical characterization of the coupled resonators by laser vibrometer as described in section 4.2. The resonator length, width, and thickness in these UW-MEMS fabricated coupled resonators are 680 μm , 100 μm , and 1.25 μm , respectively, where the coupling length, width, and thickness are 340 μm , 20 μm , and 1.25 μm. The coupling location from the anchored part of the clamped-clamped beam is 170 μm.

Figure 4.4 shows SEM of designs A and B, which are coupled two resonators fabricated in CMOS35. These clamped-clamped microbeams employ the same above-mentioned stack of structural layers in CMOS35 technology as the ones used by the single resonator C. The specifications of these two designs are given in 4.2. Figure 4.5 depicts SEM of designs D and E, which are coupled three resonators fabricated in CMOS35. Designs D and E are similar in dimensions and specifications to designs A and B, respectively. The only difference is in that D and E are coupled three resonators for a three-pole filter.

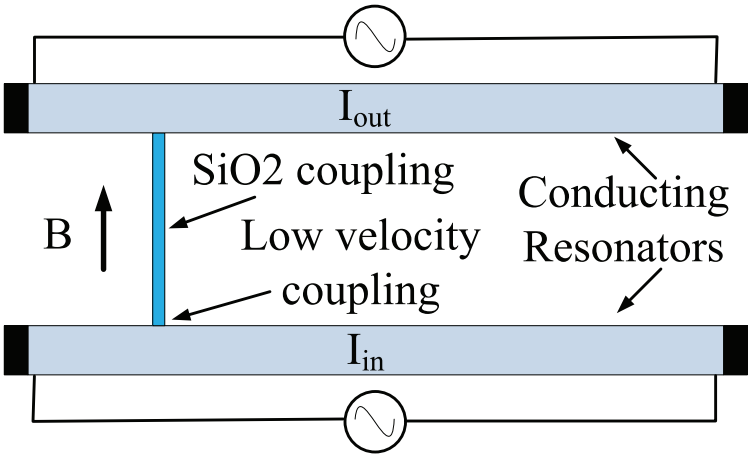

Schematic of measuring setup

Design A's SEM

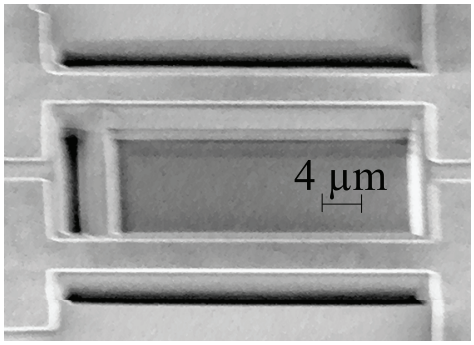

Design B's SEM

Figure 4.4: SEMs of designs A and B and schematic of measuring setup

Figure 4.6 shows the layouts of the fabricated single resonator designs C, P, U1, and U2. These designs are fabricated in CMOS35, PolyMUMPs, and UW-MEMS, respectively. Figure 4.8 shows the layouts of CMOS35 designs A and B, whose specifications are given in 4.2. Figure 4.9 depicts the layouts of CMOS35 fabricated designs D and E, coupled three resonators. Figure 4.7 displays the layouts of the coupled two resonators fabricated in UW-MEMS.

Applying electrodynamic transduction for out-of-plane vibrations of microfabricated designs requires inserting the microstructures in an external in-plane magnetic field. Furthermore, to identify the maximum Q performance of the moving microstructures, the experiments need to be achieved in vacuum. This requirement

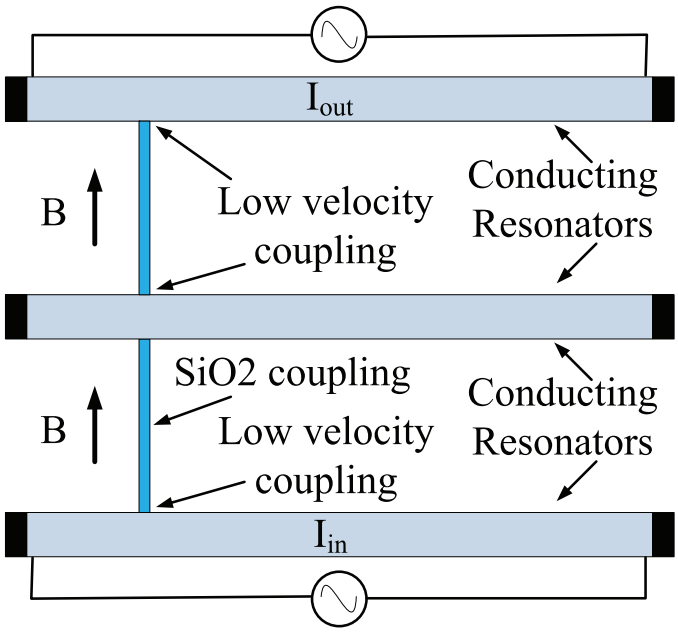

Schematic of measuring setup

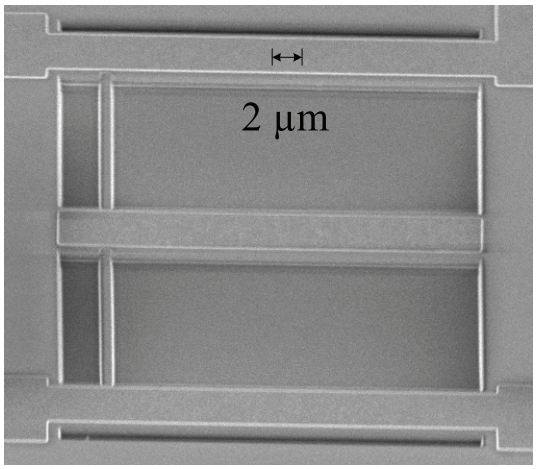

Design D's SEM

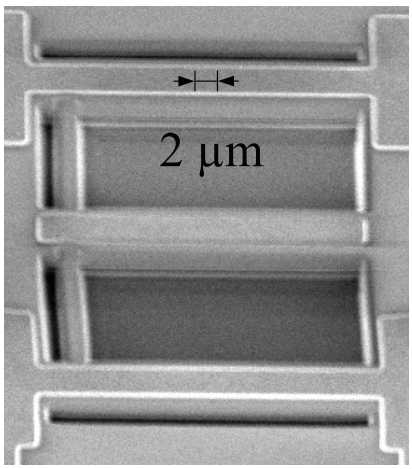

Design E's SEM

Figure 4.5: SEMs of designs D and E and schematic of measuring setup

is especially important as it allows for the electrical performance of the vibrating microstructures with the mechanical origin to be distinguished from possible electrically originated responses. Therefore, comparing measurements in air and vacuum enables researchers to find the sharp change of response in a vacuum due to mechanical vibrations. For mechanical measurements by vibrometer, the vacuum chamber requires an optically transparent window for the laser beam to pass through to illuminate the moving microstructure's surface and be reflected back to the laser vibrometer detector.

Figure 4.10 shows pictures of the experimental setup, displaying a custom-made mini-vacuum chamber, a Polytec laser vibrometer, and a test fixture including permanent magnets and a chip holder. The experimental setup is designed and fabricated to address all the above-mentioned requirements: a mini-vacuum chamber to be fitted under an available laser vibrometer microscope; a magnetic circuit to provide an in-plane magnetic field; a chip holder wafer with electrical lines made of gold to allow for the electrical connections to be provided to the chip through wirebonding; BNC connections inside the mini-vacuum chamber with wires to be connected to the chip wafer; a test fixture to accommodate the external magnetic field, the chip holder wafer, and mechanical facilities for adjusting and fixing its position inside the vacuum chamber with respect to the laser vibrometer; external electrical BNC connections for connecting the microsturctures to outside equipment and measuring tools.

Figure 4.11 displays the mini-vacuum chamber. I designed this mini-vacuum chamber and supervised its fabrication in the University of Waterloo workshop for the experimental part of this work. The main parts of this equipment are the mini-vacuum chamber body, including vacuum connections to gauge, valve, and pump, the door accommodating the optical transparent window, the guiding screws for the text fixture position to be adjusted to the laser source and fixed inside the mini-vacuum chamber, and internal wires connecting to BNC connectors that provide access for input/output electrical signals to outside measurement equipment.

The mini-vacuum chamber is equipped with vacuum gauge, vacuum valve, and four ports for electrical connections. Two of these electrical ports use floating ground BNC connectors. The optically transparent window located in the mini-vacuum chamber's door includes an optical grade highly transparent glass with anti-reflection coatings on its both surfaces to minimize reflections. The transparent window is for the laser beam to pass through and be reflected back from the

out-of-pane moving surface of the designs as well as for observing the chip under microscope. Employing the described experimental setup will allow for mechanical measurements as well as the electrical characterization of the moving microstructures both in air and in vacuum.

Figure 4.12 depicts the test fixture accommodating chip holder wafer for inserting chip in the magnetic field, the magnetic circuit providing the in-plane external magnetic field for the chips under test, and corresponding holes for adjusting and fixing the test fixture in the mini-vacuum chamber. Figure 4.13 shows a text fixture providing the same functionality as the one displayed in 4.12; however, this test fixture exposes the designs on the chip to an out-of-plane magnetic field. Therefore, the microresonators are driven into their in-plane vibration modes. Figure 4.14 depicts the test fixture used for the experiments before the fabrication of the mini-vacuum chamber.

The magnetic circuit connecting two permanent magnets to create the magnetic field necessary for the microresonators is another important part of this experimental setup. Test fixtures accommodate the magnetic circuit, chip wafer holder, and mechanical elements to fix the chip holder wafer in its location. The test platform also includes holes for fixing it inside the min-vacuum chamber.

Figure 4.16 shows chips of the designs in CMOS35, UW-MEMS, and PolyMUMPs fixed on the chip wafer holder. Figure 4.15 displays different wafer holders for in-plane and out-of-plane magnetic fields. Fixing chips on the wafers allows electrical connections to be provided to the designs through wirebonding. The designed and fabricated chip holders are of two types, both of which are displayed in 4.15. These wafers position the chip in the most uniform location of the external magnetic field and are fixed on the test fixtures inside the magnetic field.

The prepared setup allows for the mechanical and electrical measurements of clamped-clamped micromechanical resonators (CCμMR) reported in the following sections.

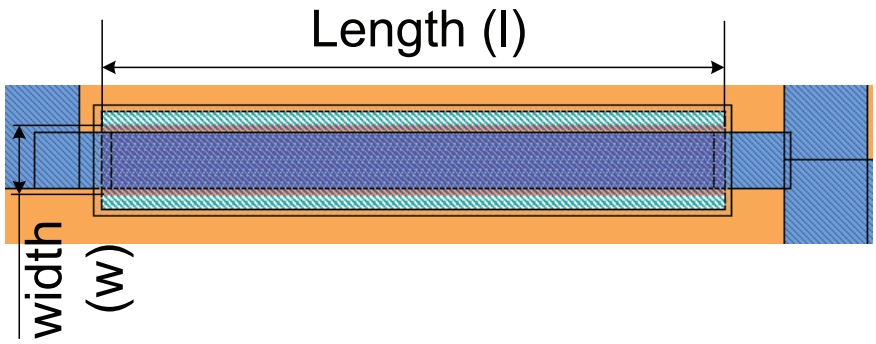

CMOS35 design layout C

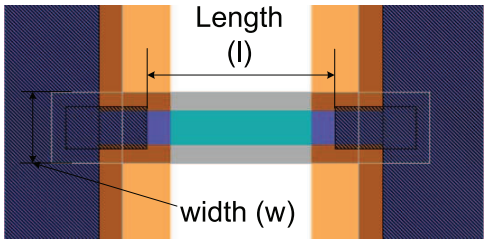

PolyMUMPs design layout P

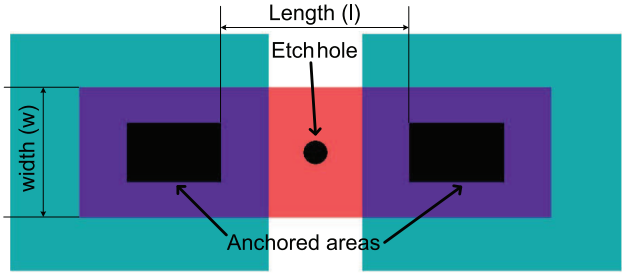

UW-MEMS design layout U1

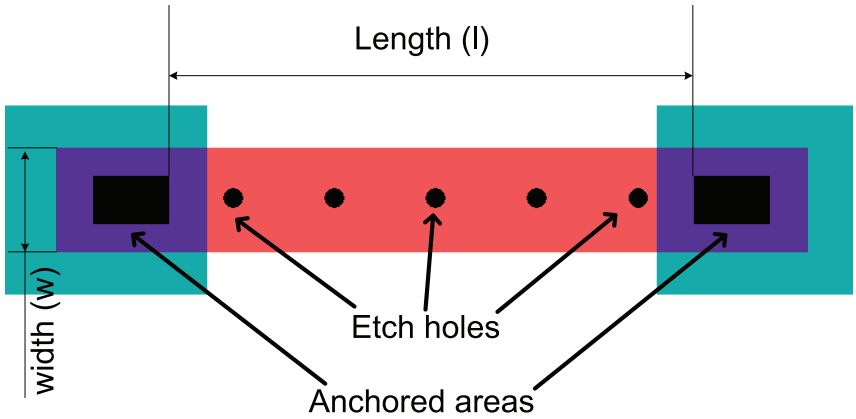

UW-MEMS design layout U2

Figure 4.6: Layouts of single resonator designs C, P, U1, and U2

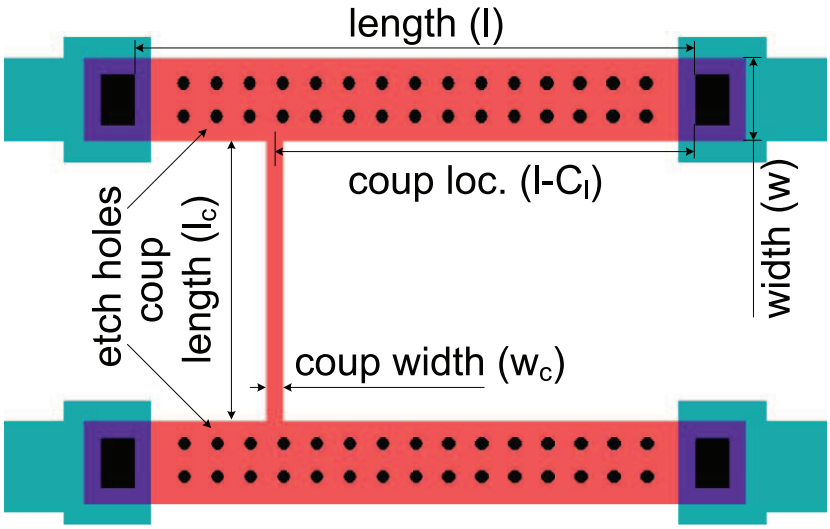

UW-MEMS coupled resonators layout

Figure 4.7: Layout of coupled resonators fabricated in UW-MEMS

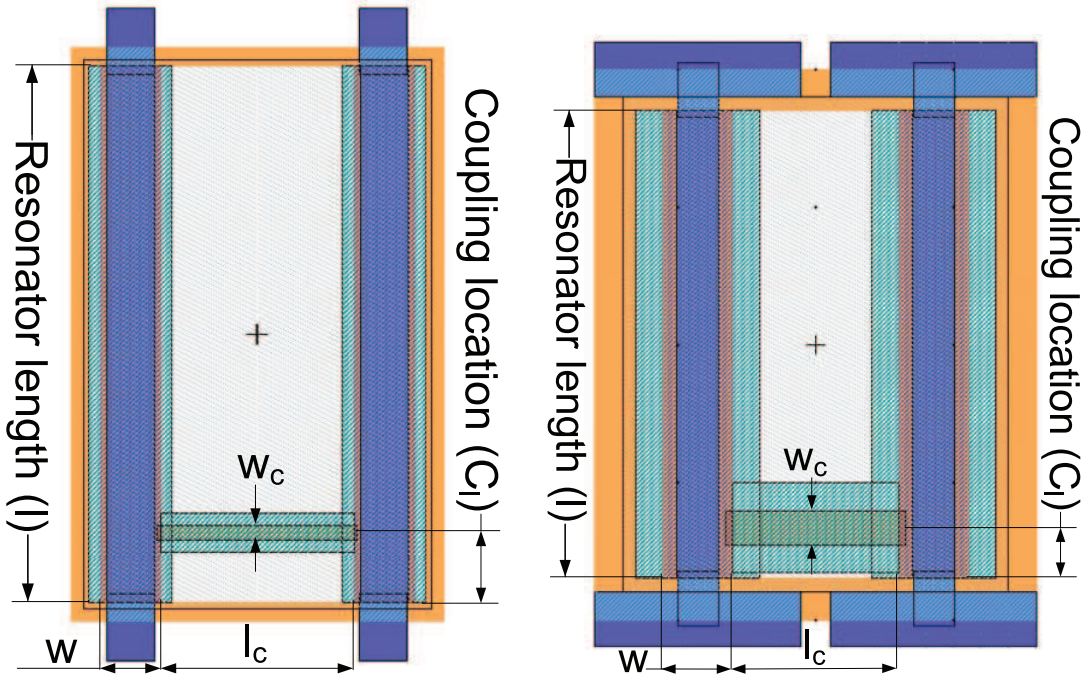

(a) CMOS35 design A layout

(b) CMOS35 design B layout

Figure 4.8: Layouts of the CMOS35 designs A and B

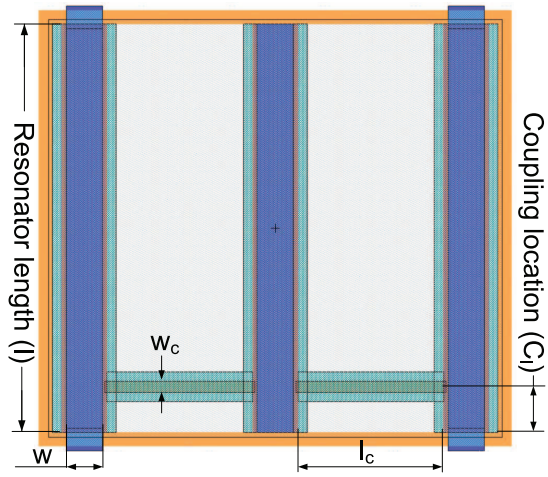

(a) CMOS35 design D layout

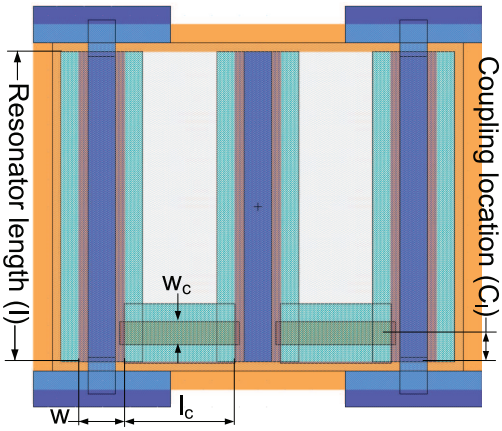

(b) CMOS35 design E layout

Figure 4.9: Layouts of the CMOS35 designs D and E

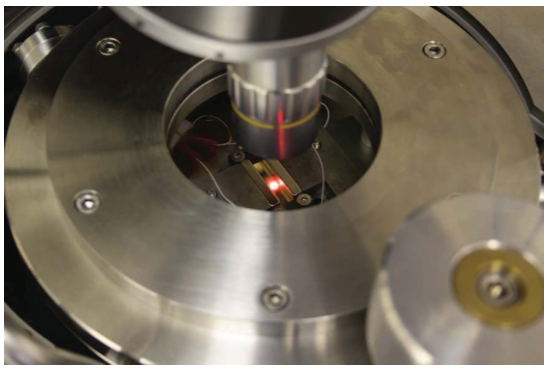

Mini-vac chamber 1

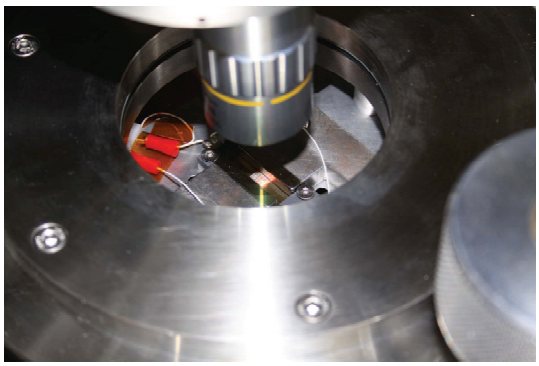

Mini-vac chamber 2

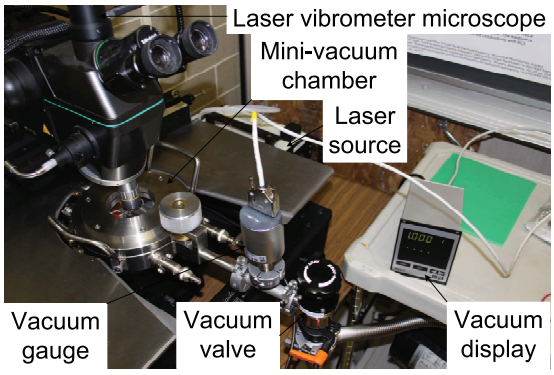

Mini-vac chamber 3

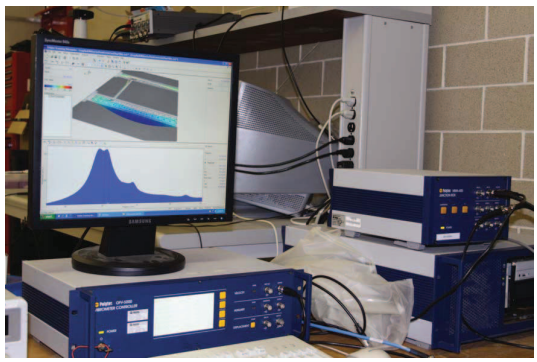

Laser vib and data display

Figure 4.10: Experimental setup, mini-vac chamber, and laser vibrometer

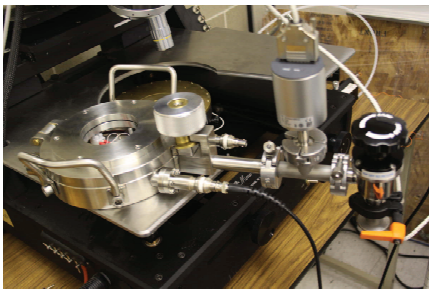

Mini-vac chamber 4

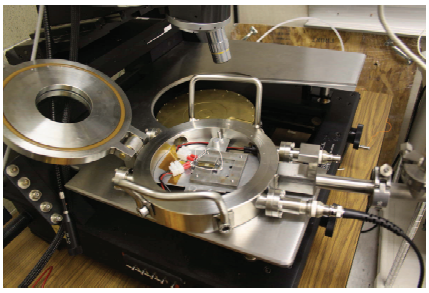

Mini-vac chamber 5

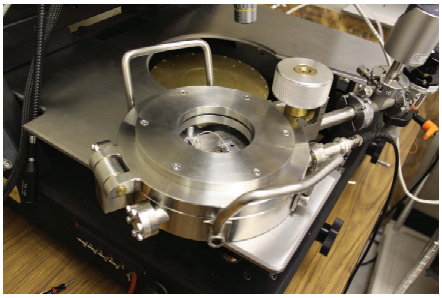

Mini-vac chamber 6

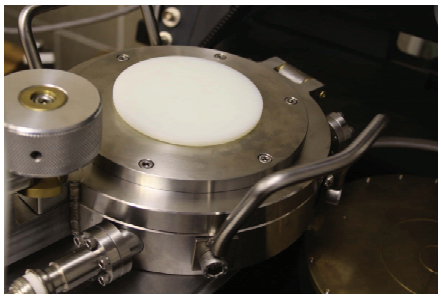

Mini-vac chamber 7

Figure 4.11: Mini-vacuum chamber

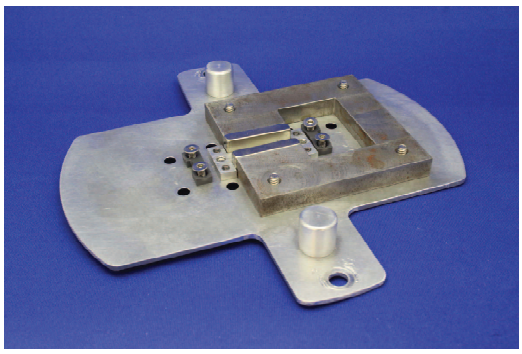

Test fixture for in-plane $\vec{B}$

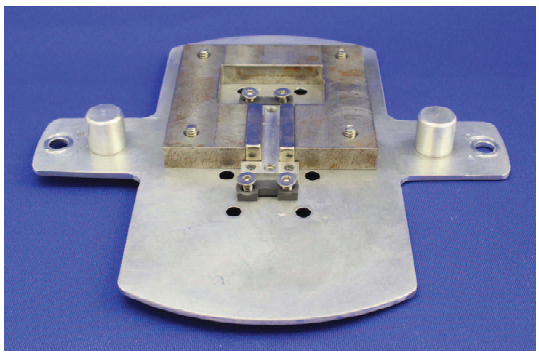

Test fixture for in-plane $\vec{B}$

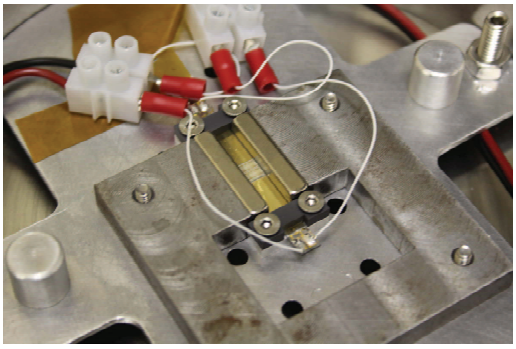

Test fixture inside vac chamber

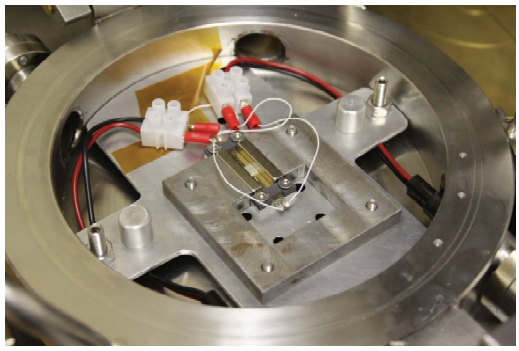

Test fixture inside vac chamber

Figure 4.12: Test fixture holding chips and providing in-plane magnetic field

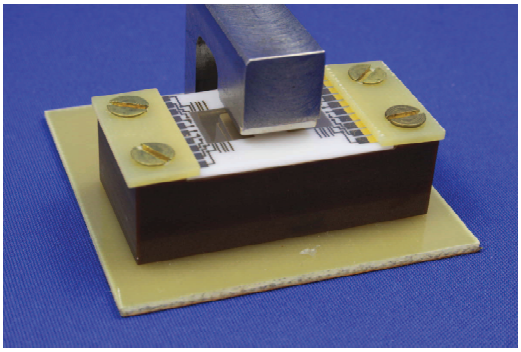

Test fixture for out-plane $\vec{B}$

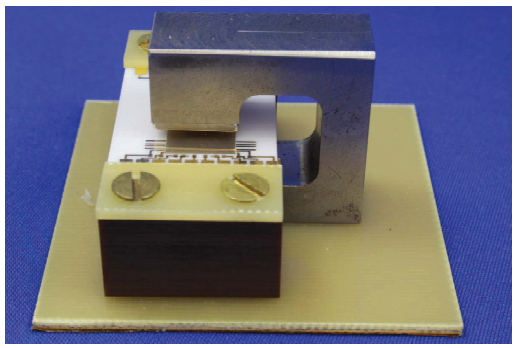

Test fixture for out-plane $\vec{B}$

Figure 4.13: Test fixture holding chips and providing Out-of-plane magnetic field

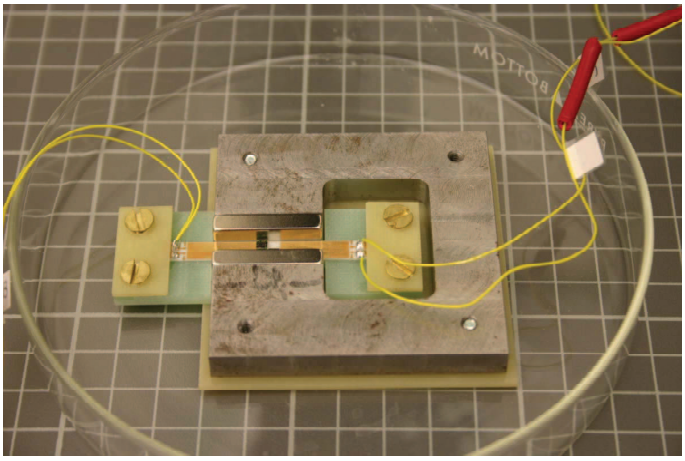

Figure 4.14: Test fixture used in experiments before making vacuum chamber

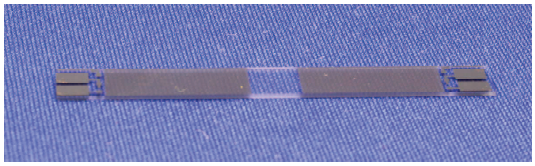

Chip holder wafer for in-plane $\vec{B}$

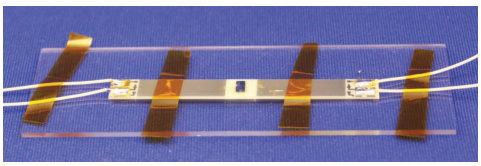

Chip holder wafer for in-plane $\vec{B}$

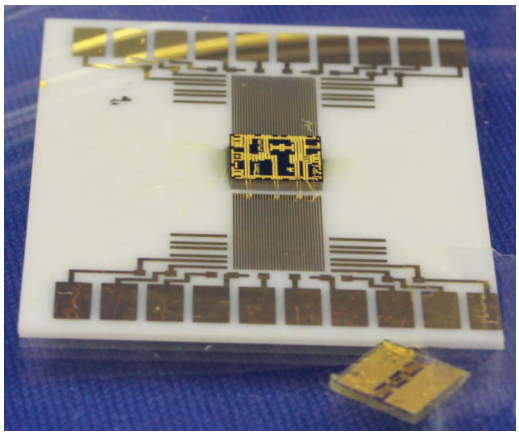

Chip holder wafer for out-plane $\vec{B}$

Figure 4.15: Wafer fabricated for holding the design chips on test platrom

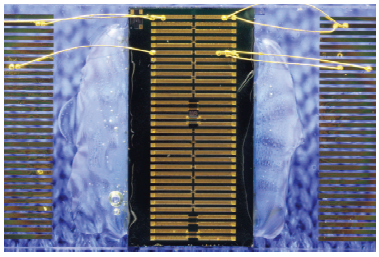

PolyMUMPs chip on wafer

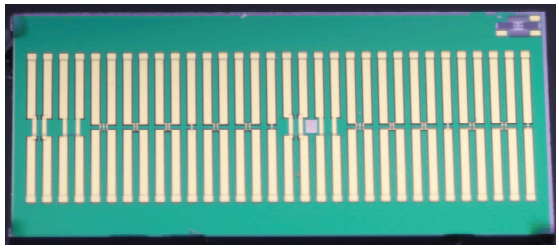

PolyMUMPs chip

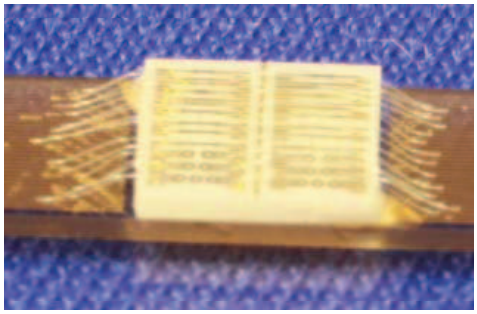

UW-MEMS chip on wafer

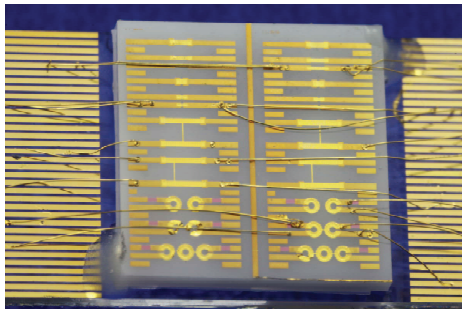

UW-MEMS chip on wafer

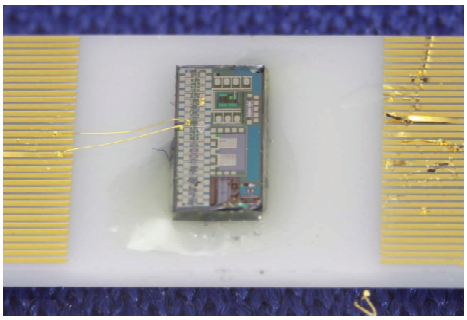

CMOS35 chip on wafer

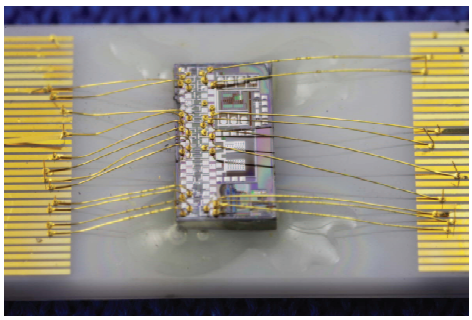

CMOS35 chip on wafer

Figure 4.16: Wafer fabricated for holding the design chips on test platrom

4.2 Mechanical and electrical measurements

Use of a laser vibrometer allows for mechanical measurements of the microfabricated designs. Single and coupled clamped-clamped microbeams resonate into and out-of-plane using Lorentz-force transduction in the presence of an in-plane external magnetic field. The chips including microresonators are fixed on the test fixtures and inside the mini-vacuum chamber. The mini-vacuum chamber is then fitted under a microscope, allowing for laser vibrometer measurements. Laser vibrometer use in the mechanical measurements, the experimental evaluation in air and vacuum of single and coupled microresonators, and their performance-related results computed from experimental data are reported.

The Polytech laser vibrometer used in these experiments allows a laser beam at 632.8 nm to illuminate the surface of a microstructure. The Doppler effect is the operation principle behind these vibrometers. The laser beam illuminates the out-of-plane moving microresonator's surface through the optically transparent window of the mini-vacuum chamber. The laser vibrometer in all these measurements is used to either measure the velocity or displacement of moving microstructures. Accordingly, the reflected back laser beam is detected from which the velocity and displacement of the microbeam's moving point are calculated. Furthermore, the FFT components of the signal are also retrieved. Applying these measurements on enough points on the surface of an out-of-plane moving microresonator's surface results in deriving the mode shapes and resonance characteristics of the moving structures. These measurements result in identifying the actual performance, including frequency response and the quality factor of the microresonators in air and vacuum.

Figures 4.17, 4.18, 4.19, and 4.20 display the derived-by-laser-vibrometer flexural mode shapes and resonance specifications of four single CCμMR designs in air and in vacuum. The input signal to the resonators is pseudo random (noise). The applied input voltage in these experiments is 3 V, where the blocked resistance (R_e) of the resonator, including connecting wires and wirebondings resistance, is about 10 Ω. However, the performance of the resonators is equally measurable whether the excitation voltages is 0.1 V or 5 V. In all these experiments, the measured magnetic field experienced by CCμMR is 0.5 Tesla.

Figures 4.21 and 4.22 show the SEM, a schematic of the measurement setup, and the measured performance of the coupled CCμMR: a Q of 1764 in vacuum and

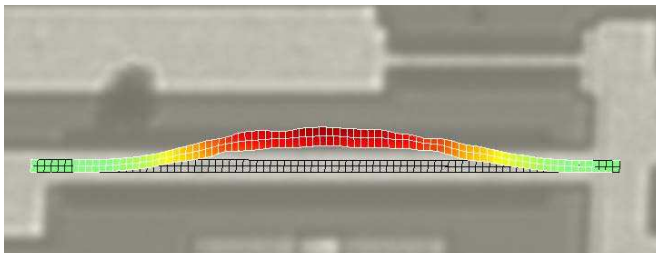

(a) C 1st flex mode

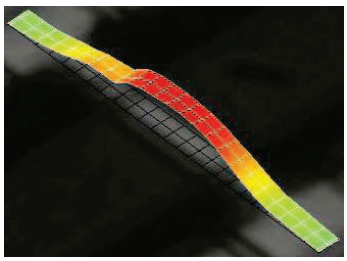

(b) P 1st flex mode

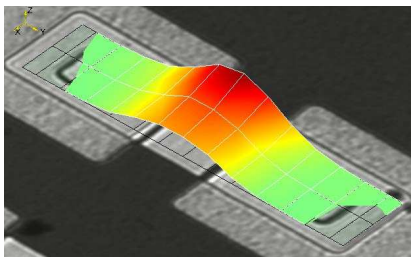

(c) U1 1st flex mode

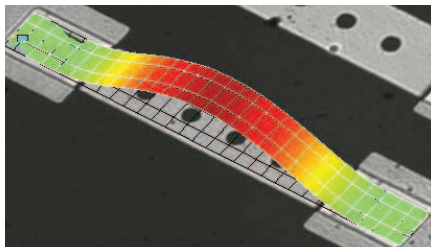

(d) U2 1st flex mode

Figure 4.17: Measured by laser vib. 1st mode of C, P, U1, & U2

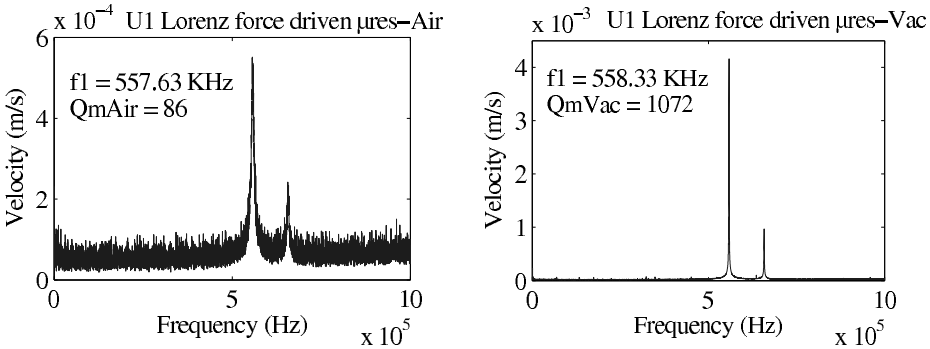

(a) Measured in air

(b) Measured in vacuum

Figure 4.18: Measured by laser vib. frequency response of U1

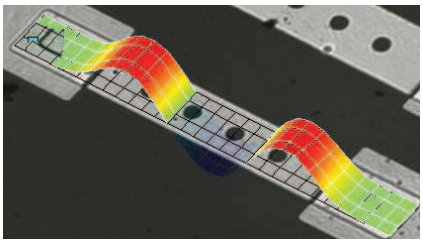

(a) U2 3rd mode

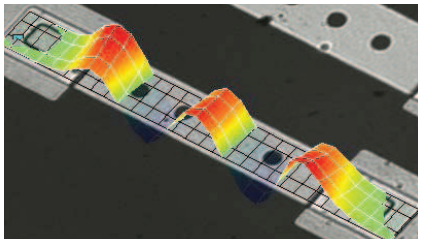

(b) U2 5th mode

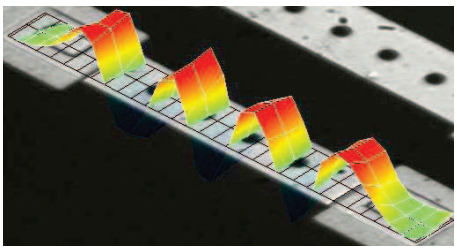

(c) U2 7th mode

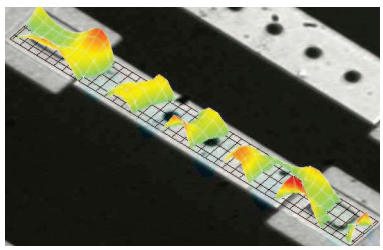

(d) U2 9th mode

Figure 4.19: Measured by laser vib. higher modes of U2

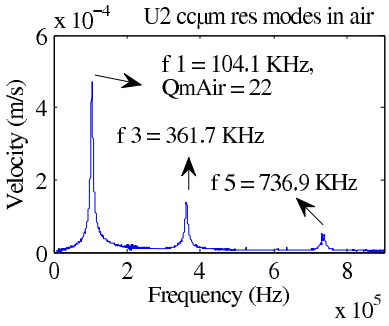

U2 frequency response in air

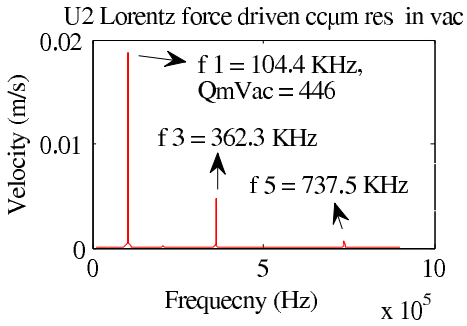

U2 frequency response in vac

Figure 4.20: Measured by laser vib. freq. response of U2 in air and vacuum

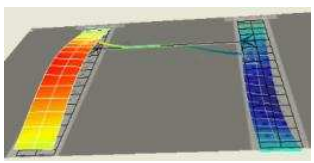

Out-of-Phase mode

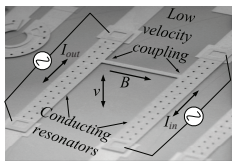

UW-MEMS coup. res. SEM

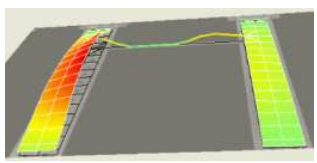

In-Phase mode

Figure 4.21: Lorentz-force driven coupled CCμMR 1st in-phase/out-phase modes

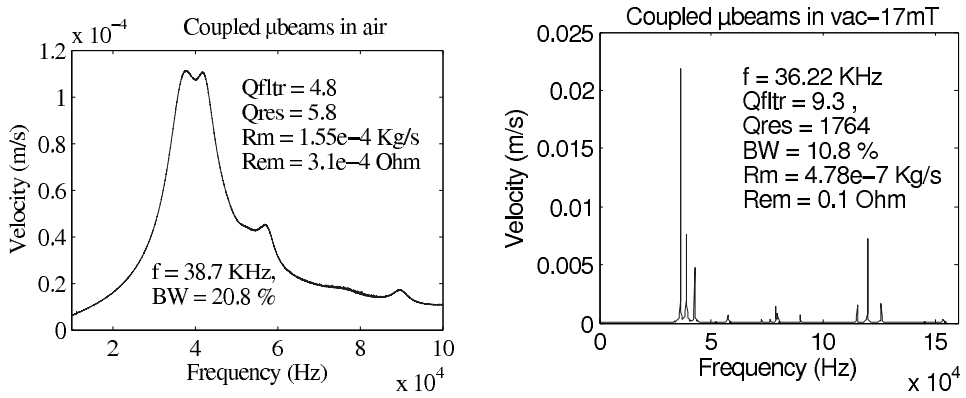

Figure 4.22: Lorentz-force driven coupled μresonators in air and vacuum

5.8 in air for the 1st flexural mode and the computed motional resistance of 0.1 Ω in vacuum. Figures 4.23 and 4.25 show design As and B's laser-vibrometer-derived first in-phase and out-of-phase modes. Figure 4.24 displays design As derived-by-laser-vibrometer third in-phase and out-of-phase modes. Figure 4.2 shows the SEMs of CMOS35 fabricated designs A and B displaying two identical clamped-clamped microbeams that are mechanically coupled by a single SiO2 μbeam. This coupling beam provide the two mechanical resonators a low stiffness coupling required for a narrow bandpass filter; however, the two conducting mechanical resonators remain isolated electrically for the coupling beam made of Sio2. Using low velocity coupling in 4.2, for example, allows design A and B to perform as narrow band pass filters: 0.144 % and 0.141 % bandwidth in vacuum, respectively. Table 4.2 summarizes the two designs specifications and measured performance.

Figures 4.26 and 4.27 show the measurement by vibrometer the two-pole filters made of coupled microresonators, A's and B's, frequency response in air and vacuum. The displayed results correspond to the first flexural mode vibrations of the coupled clamped-clamped microresonators. The results including measured Q and the resonance frequency provide data for motional resistance computations by 3.13 and 3.14, where applicable equivalent electrical circuit models are illustrated in 3.5, 3.6 and 3.7.

In fact, two R_{em} values are calculated for the two first coupled in-phase and out-of-phase modes, corresponding to the two modes different Q_m , K_{eq} , and M_{eq}. The in-phase modes M_{eq} and K_{eq} are the ones computed for either resonator of the two coupled resonators. However, the out-of-phase modes M_{eq} and K_{eq} receive

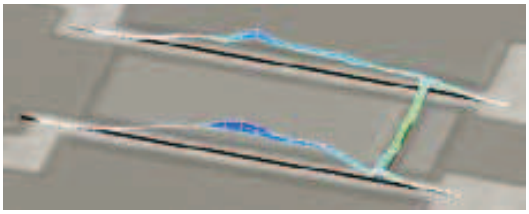

A's 1st mode in-phase

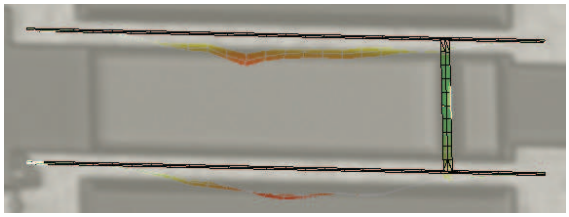

A's 1st. mode in-phase

A's 1st mode out-phase

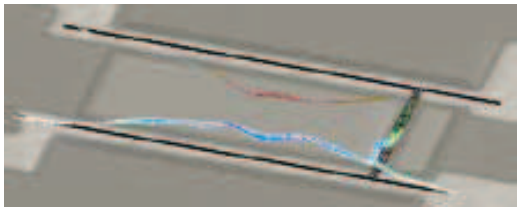

A's 1st mode out-phase

Figure 4.23: Designs A derived by laser vibrometer 1st in-phase/out-phase modes

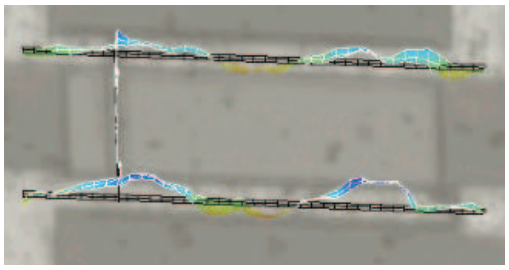

A's 3rd mode in-phase

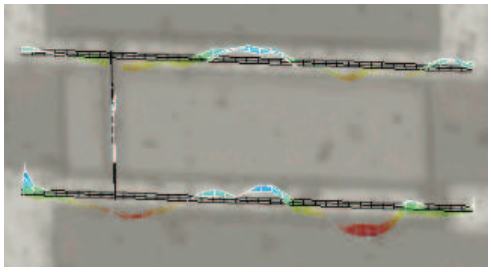

A's 3rd mode in-phase

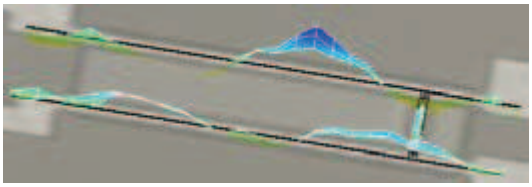

A's 3rd mode out-phase

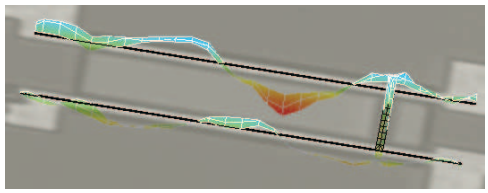

A's 3rd mode out-phase

Figure 4.24: Designs A derived by laser vibrometer 3rd in-phase/out-phase modes

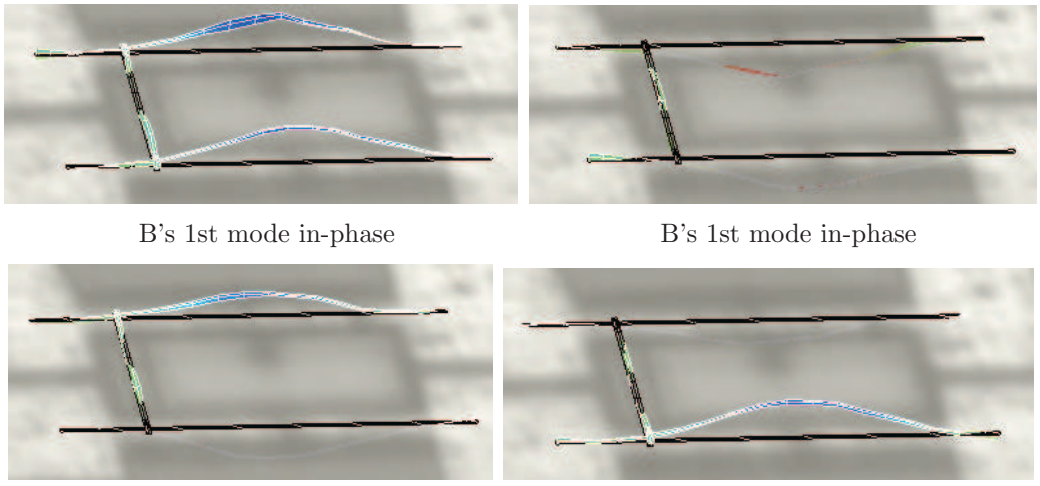

Figure 4.25: Designs B derived by laser vibrometer 1st in-phase/out-phase modes

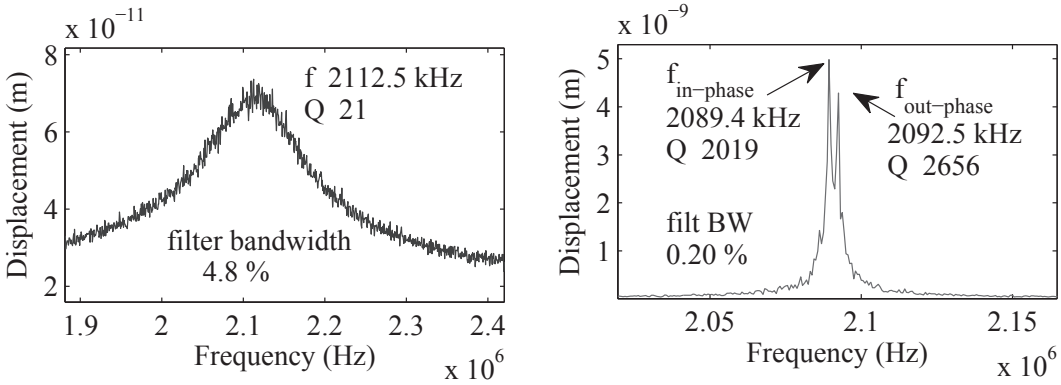

(a) A's freq response in Air

(b) A's freq response in Vac

Figure 4.26: Measured by vibrometer A's freq response in air and vacuum

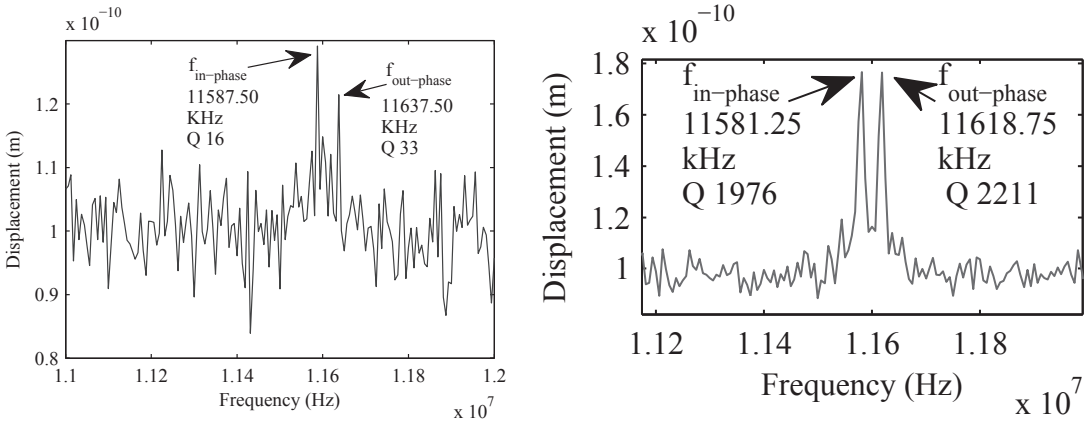

(a) B's freq response in Air

(b) B's freq response in Vac

Figure 4.27: Measured by vibrometer B's freq response in air and vacuum

contributions from the coupling microbeam as depicted in 3.7.

Figure 4.28 shows coupled modes of design B1. B1 is a CMOS35 fabricated design similar in dimensions and structure to B; however, design B1 is tested under laser vibrometer using a temporary license for higher resolution of the vibrometer software. This higher resolution version allows identification of some complex rotational/flexural modes demonstrating very large values of Q_m, even in air. Figure 4.29 displays the measured-by-laser-vibrometer very high Q_m modes. The measured Q_m is to the limits of the software resolution, with the actual corresponding values expected to be higher. The measured Q_m for these coupled modes, which have large values in air, shows significant decrease in vacuum, as displayed in 4.29.

Coupled three resonators are displayed in 4.30, illustrating the measured-by-laser-vibrometer frequency response of these coupled three resonators. These resonators are similar to design A but instead of two resonators, three similar resonators are coupled. However, due to the three modes associated with these couplings, the coupled three resonators can perform as a three-pole filter. Figure 4.31 shows the measured-by-laser-vibrometer D's 3rd flexural modes. The 1st flexural mode shapes of these coupled three resonators are depicted in 4.32.

Directly measuring mechanical motions of the micromechanical resonators enables directly characterizing their performance. Mechanical measurements allow

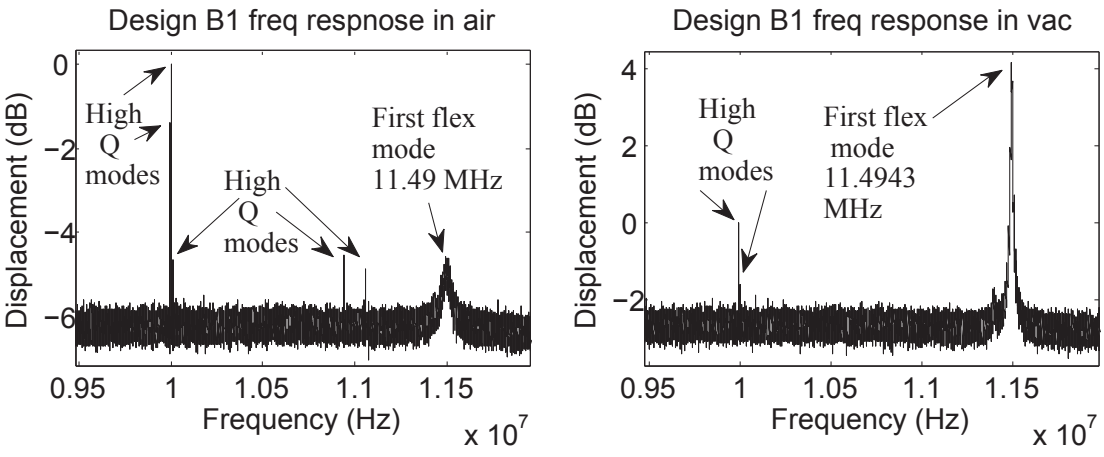

B1's freq response in air

B1's freq response in vac

Figure 4.28: Measured by vibrometer B1's coupled modes in air and vac

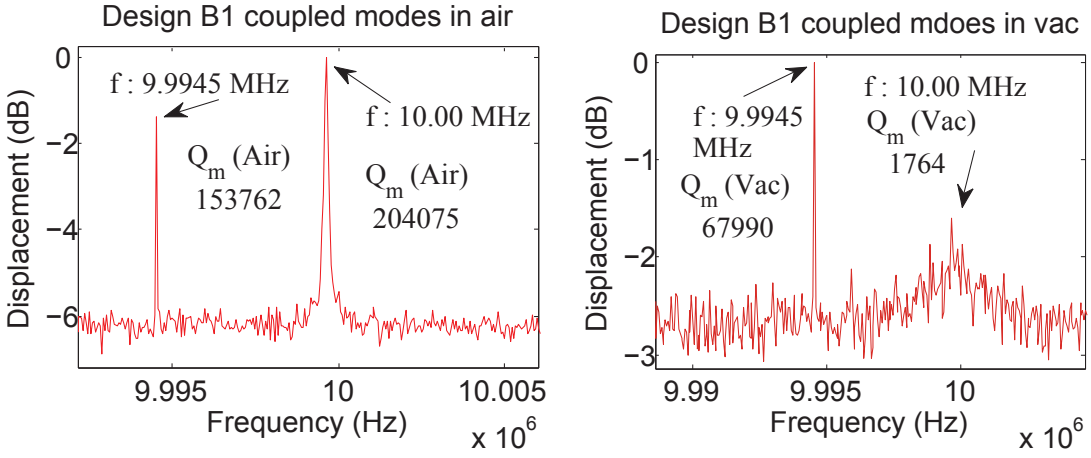

B1's high Q complex mode in air

B1's high Q complex mode in vac

Figure 4.29: Measured by vibrometer B1's high Q coupled modes in air and vac

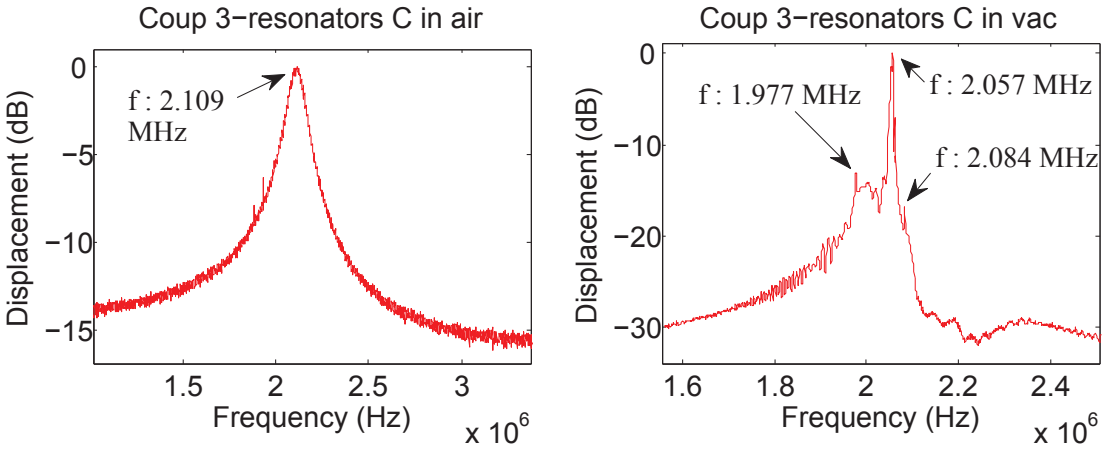

D's response in air

D's response in vac

Figure 4.30: Measured by vibrometer D's frequency response in air and vac

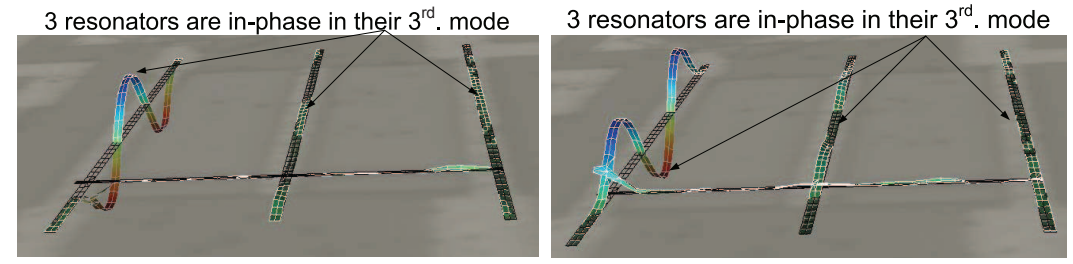

D's 3rd mode in-phase

D's 3rd mode in-phase

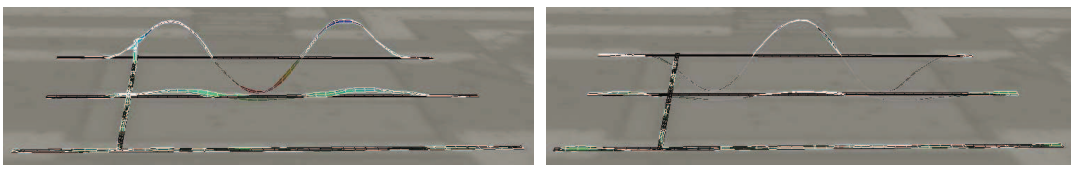

D's 3rd mode in-phase

D's 3rd mode in-phase

Figure 4.31: Measured by vibrometer D's 3rd mode

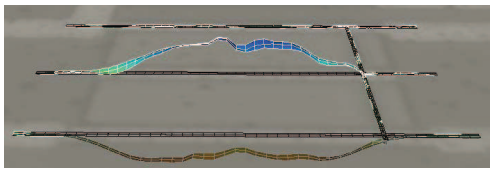

D's 1st mode out-phase

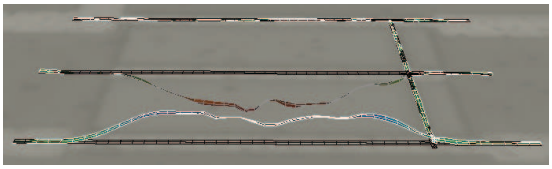

D's 1st mode out-phase

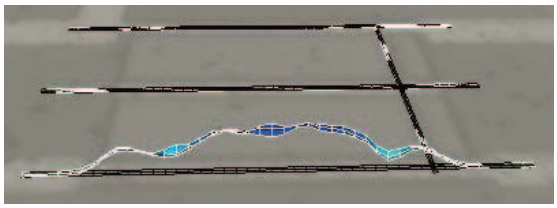

D's 1st mode out-phase

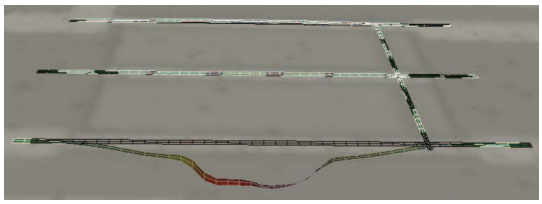

D's 1st mode out-phase

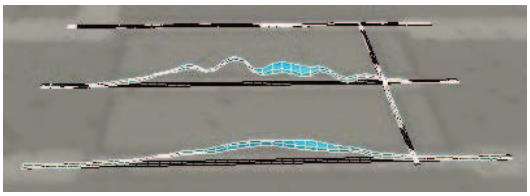

D's 1st mode out-phase

D's 1st mode out-phase

D's 1st mode in-phase

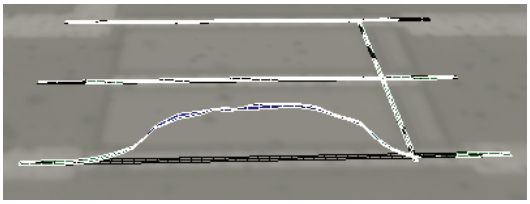

D's 1st mode in-phase

Figure 4.32: Measured by vibrometer D's 1st mode

directly derivation of transduction technique performance. Accordingly, for a given electrical input, the mechanical output is measured, and for the produced electrical output, the input to the mechanical side is known. Use of a laser vibrometer for mechanical measurements, experimental results in air and vacuum of single and coupled microresonators, and micromechanical resonators' motional resistance computed from experimental data are discussed.

Use of laser vibrometers for mechanical measurements has significantly facilitated characterization of micromechanical resonators. Using a laser vibrometer to measure the displacement and velocity of a large number of points on a moving microstructure's surface allows identifying more data than resonance frequency and Q. The out-of-plane vibrations of these microresonators are measured in air and vacuum by the laser vibrometer, resulting in extraction of mode shapes and resonance specifications. These data facilitate any further electrical measurements by providing the exact data of the resonance frequency and the mode shapes. Therefore, the expected electrical signal that is to be measured is already known.

Mechanical measurements in air and vacuum shows higher mode driving of single and coupled microresonators. For example, U2's higher modes are displayed in 4.19. The first flexural mode of U2 is about 95 KHz; however, the identified 9th flex mode of U2 is measured: 11.8172 MHz with Q 458 in air and 3925 in vacuum (10mT). Should the judgment be on an electrically measured signal, the derived data may only display the resonance at the given frequency with no more information about the mode shape or other resonance characteristics. Although no direct evidence can be provided in this step whether or not the use of Lorentz-force transduction has enabled this performance, there is the possibility that this higher mode (9th) driving occurs because of the bi-directional nature of the Lorentz force.

The measured mechanical Q_m for single resonators, C, P, U1, and U2, and coupled resonators A and B are expected to be higher than what are measured. Either of three factors might be the reasons for low measured mechanical Q_m. One reason could be the frequency resolution settings in the software used by the laser vibrometer, when the actual Q could be higher. The software limitation is confirmed to be one of the reason, as displayed in the measurements on B1. Design B1 is similar in dimensions and structure to B, and both are fabricated in CMOS35. Using a temporary license for higher resolution of the vibrometer software results in identification of some complex coupled rotational/flexural modes demonstrating very large values of Q_m even in air. Figure 4.29 displays results measured by laser

vibrometer of very high Q_m modes. The measured Q_m for these coupled modes, which have large values in air, shows significant decrease in vacuum. Finding the reason behind this behavior requires more experiments; however, in the presence of air, the first flexural mode is significantly damped where these high Q_m-coupled modes, which apparently have fewer interactions with air, demonstrate high values of Q_m. In vacuum, it seems that the energy from these high-Q modes might leak to the main flexural mode that demonstrates high Q in a vacuum. Nevertheless, an accurate judgment requires more experiment.

The second reason might be that the microstructures in all four designs are clamped-clamped beams, which are limited to providing high Q values because of significant loss at the anchored locations [61], although the reported Q with electrostatically driven clamped-clamped beams is higher [4]. The third reason might be the driving current that possibly can cause a thermo-elastic-related type of damping. With the focus of this paper on introducing experimental results on low motional resistance of the Lorentz-force transduction, research on the input current effect on damping and on more accurate measurement techniques has been left for the continuation of this work. However, the initial expectation is that the Q of the micromechanical resonator is independent of the transduction technique, whether electrostatic or electrodynamic.

The resonance frequencies computed for micromechanical resonators show differences with the experimentally measured ones reported in 4.1 and 4.2. This deviation may be due to the value considered for residual stress [62], [63], [59], [60]. The assumed residual stress of the Al layer, for example, before any post processing, is expected to be tensile with the given average value; however, the post processing of the CMOS35 chips in dry etching and wet release, for example, could have modified the stress and even reversed its role by making it compressive rather than tensile.

Measurements on coupled resonators A and B show the effective use of low velocity coupling that implements very narrow band pass filters 4.2: 0.144 % and 0.141 % bandwidth in vacuum, respectively. Should such a low velocity coupling technique not be employed, microbeam resonators and their coupling beam that do not have significant stiffness differences would produce two distinct peaks of resonance, too far apart to be adjusted for a filter performance.

The mechanical measurements by laser vibrometer provide sufficient data for

micromechanical resonators' motional resistance computation. Experimentally derived resonators' Q_m and resonance frequencies are all data required for calculating motional resistance from (3.14). These computations are based on the resonators' equivalent circuit models displayed in 3.4, 3.5, 3.6, and 3.7. All these results facilitate characterization of single and coupled resonators' electrical performance regarding the very small output signals' amplitude, as computed in 4.1.

Laser vibrometer use enables directly characterizing single and coupled micromechanical resonators. Such a direct measurement allows for obtaining significant data of the fabricated designs' performance. The experiments in air and vacuum on single and coupled microresonators produce enough data for motional resistance computations as well as to identify the relationship with the corresponding mode. Mechanical measurements have significant impact on facilitating electrical measurements.

The measured electrical performance of single and coupled micromechanical resonators driven by Lorentz-force transduction are reported. The reported results include measurements in air and in a vacuum, allowing for electrical responses of mechanical origin be identified. Those single and coupled micromechanical resonators whose electrical performance are reported are the microfabricated designs that are described in previous section 4.2. Therefore, the electrical measurements are comparable with the corresponding mechanical measurements: single port s-parameter measurements, Q-computations for single resonators, electrical impedance variation of Lorentz-force driven single resonators, and two-port s-parameters measurements of coupled resonators.

Figure 4.33 shows single-pole electrical measurements (S11) of U1 in air and vacuum by Vector Network Analyzer (VNA), Agilent E5061B. The electrically measured Q is the loaded Q (Q_L) from which the unloaded Q (Q_{UL}) is computed using (4.1), where k_e is the electrical coupling [64], [19].

$$Q_{UL} = Q_L\,(1 + k_e) \tag{4.1}$$

Electrical coupling, k_e, represents the electrical resonator interaction in connection with the external electrical circuit such as the measuring equipment. Computing k_e from experimentally measured $S11$ requires determination of $S11_{min}$ (dB) corresponding to the resonance frequency displayed in 4.33. By deriving $S11_{(\phi=45^\circ)}$

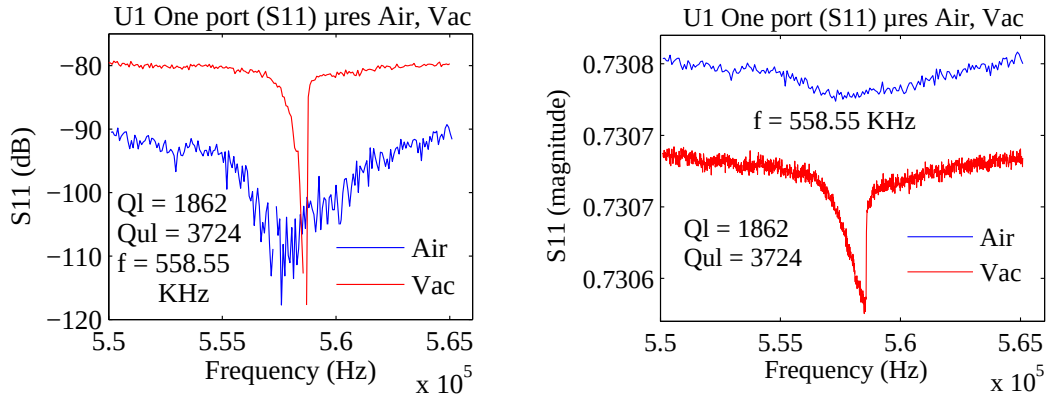

(a) U1 in air & vac (dB)

(b) U1 in air & vac (magnitude)

Figure 4.33: VNA measured Lorentz-force driven U1

(dB) from (4.2), two frequencies of f_1 and f_2 are obtained from 4.33.

$$S11_{min} = 20\log|\Gamma_{res}| = 20\log\left|\frac{k_e - 1}{k_e + 1}\right| \tag{4.2}$$

where

$$k_e = \frac{1 - 10^{(S11_{min}/20)}}{1 + 10^{(S11_{min}/20)}} \quad \text{if the resonator is undercoupled}$$

$$k_e = \frac{1 + 10^{(S11_{min}/20)}}{1 - 10^{(S11_{min}/20)}} \quad \text{if the resonator is overcoupled}$$

$$S11_{\phi} = 10\log\frac{1 + 10^{-(S11_{min}/10)}}{2}$$

Using these two frequencies and calculating Q_L from (4.3), Q_{UL} is computed from (4.1), where f_L is the resonance frequency measured and displayed in 4.33.

$$Q_L = \frac{f_L}{f_2 - f_1} \tag{4.3}$$

Figure 4.34 shows the input electrical impedance variation of the electrodynamically driven microresonator (U1) versus frequency. These illustrations show variation of the imaginary versus real part of the transducer's input electrical impedance for the measured frequency range in air and vacuum.

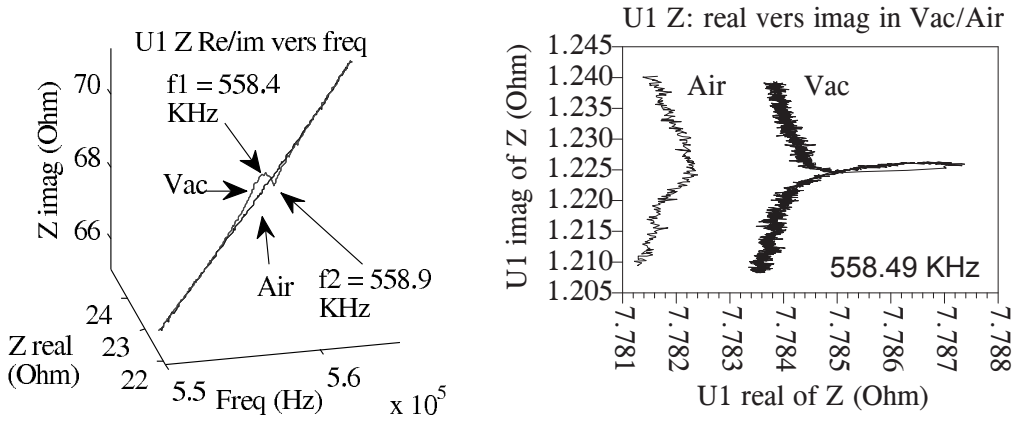

Figure 4.34: U1 measured imaginary versus real part of input impedance

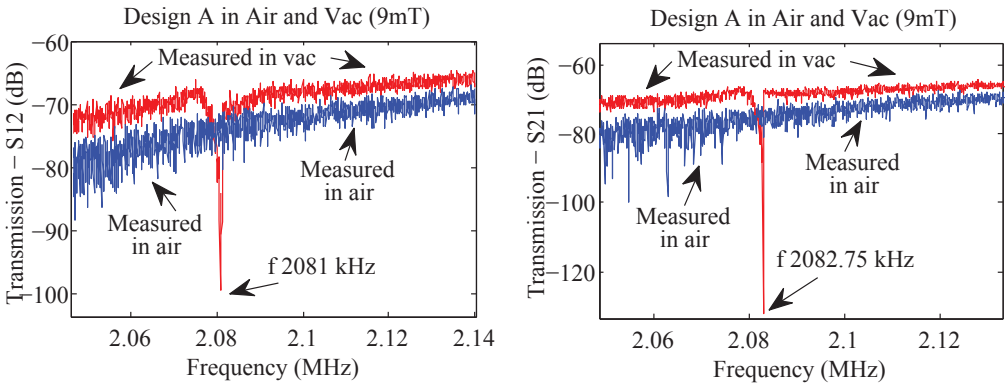

(a) A's freq response in air/vac - S12 (b) A's freq response in air/vac - S21

Figure 4.35: A's freq response in air/vac - S12, S21

Figures 4.35 and 4.36 illustrate two-port electrical measurements on designs A and B, displaying their corresponding frequency response. Agilent 8714ES VNA is employed for these measurements. The sharp change of electrical transmission at resonance in vacuum displayed in 4.35 and 4.36 are due to increase of motional resistance in vacuum, as derived from (3.13) and (3.13).

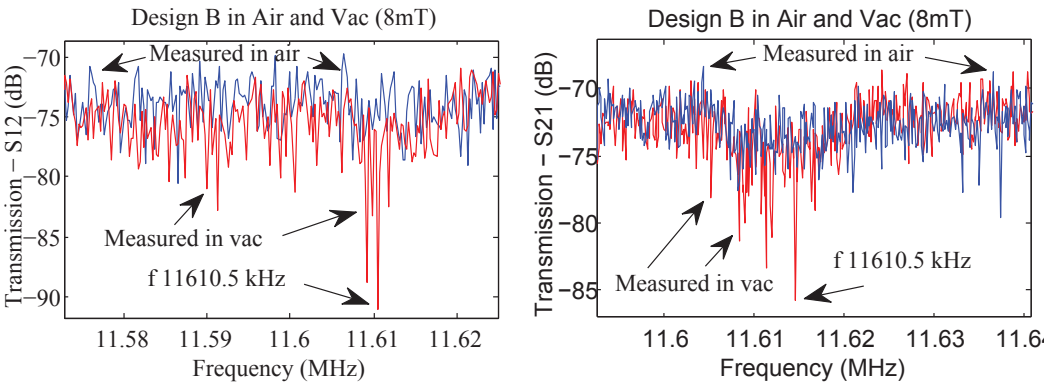

(a) B's freq response in air/vac - S12

(b) B's freq response in air/vac - S21

Figure 4.36: B's freq response in air and vac - S12, S21

4.3 Comparing measurements and computations

Table 4.1 summarizes and compares the specifications, computed performance values from equivalent models, and experimental measurement results of the single four fabricated CCμMR designs, C, P, U1, and U2. Single resonators performance is represented by their resonance frequency, quality factor, and motional impedance computed based on experimentally measured quality factor. Figure 4.33 shows the electrically measured quality factor of U1 in vacuum , which is 3724. This electrically measured Q is larger than the one measured by mechanical method. This result confirms the expectation that the actual Q should be larger than mechanically measured Q because of the vibrometer software resolution limitation. Furthermore, figure 4.34 displays an absolute change of motional resistance of U1 in air and vacuum equal to 3.4×10^{-3} (Ω) and 0.4×10^{-3} (Ω), respectively. Comparing the electrical measurements to the results from mechanical measurements shows some differences, which is due to the experimental limitations. However, the results that are in the range of $mili\Omega$ confirms the expected low motional resistance of Lorentz force transduction in the range of $mili\Omega$.

Table 4.2 summarizes and compares the specifications, computed performance values from equivalent models, and the measured performance of the two CMOS35 fabricated designs of coupled micromechanical resonators, A and B. Here, l, w, l_c, w_c, and C_l used in 4.2 are designated on the layouts of the coupled resonators, designs A and B in 4.7.

Table 4.1: Specifications of Lorentz-force driven single mechanical resonators

Designs	**C**	**P**	**U1**	**U2**
E^* (GPa)	67	133	62	50
ρ^* (Kg/m^3)	2425	6556	19300	19300
σ^* (MPa)	34.6	5.4	40.0	40.0
l (μm)	90	40	80	280
w (μm)	10	13	55	55
t (μm)	3.28	2.02	1.25	1.25
f (KHz) Eq. 3.20	2314.0	5849.5	480.0	94.5
f (KHz) *mech.measured*	2288.3	4441.3	558.3	97.2
R_m (Kg/s) *mech.measured*	3.2e-06	1.6e-05	2.2e-05	3.2e-05
R_{em} (Ω) *mech.measured*	6.4e-04	2.5e-05	7.2e-05	6e-04
$Q_m Air$ *mech.measured*	17	123	86	22
$Q_m Vac$ *mech.measured*	2069	758	1072	446
I_{rms} (A) Eq. 3.15	2.8e-05	5.7e-05	6.2e-06	2.2e-06
e_{rms} (V) Eq. 3.16	8.6e-07	3.6e-08	4.7e-08	7.7e-07
$B_{measured}$ (T)	0.5	0.5	0.5	0.5

Table 4.2: Specifications of Lorentz-force driven coupled mechanical resonators

2-pole filter design (Coupled clamped-clamped micromechancial resonators)	**A**	**B**
E^* (GPa)	67	67
ρ^* (Kg/m^3)	2425	2425
σ^* (MPa)	34.6	34.6
l (μm)	90	34
w (μm)	10	5
t (μm)	3.28	3.28
l_c (μm)	32.1	12.1
w_c (μm)	2.5	2.5
t_c (μm)	1.5	1.5
C_l (μm)	11.9	3.7
M_{eq} (Kg) Eq. 3.22	1.74e-11	4.69e-11
$K_{eq}c$ (N/m) Eq. 3.49	1.5e04	4.5e02
$K_{eq}r$ (N/m) Eq. 3.51	1.66e05	9.91e03
f $(KHz)(Comp)$ Eq. 3.20	2314.0	15549.2
$f_{air}(exp)(KHz)$ $mech.measured$	2112.50	11587.50
$f_{in-phase}(exp)(KHz)$ $mech.measured$	2078.75	11581.25
$f_{out-phase}(exp)(KHz)$ $mech.measured$	2082.50	11618.75
$Q_m air$ $mech.measured$	21	16
$Q_m(in-phase)vac$ $mech.measured$	3213	1976
$Q_m(out-phase)vac$ $mech.measured$	1309	2211
$R_m air$ $(Kg.s/m)$ $mech.measured$	2.96e-05	7.92e-05
$R_m vac(in-phase)$ $mech.measured$ $(Kg.s/m)$	1.91e-07	6.41e-07
$R_m vac(Out-of-phase)$ $mech.measured$ $(Kg.s/m)$	4.69e-07	5.75e-07
$R_{em} air$ $mech.measured$ (Ω)	6.83e-05	3.65e-06
$R_{em} vac(in-phase)$ $mech.measured$ (Ω)	1.06e-02	4.51e-04
$R_{em} vac(Out-of-phase)$ $mech.measured$ (Ω)	4.32e-03	5.03e-04
Filter $BW_{vac}(\%)$ Eq. 3.51	0.144	
Filter $BW_{air}(\%)$ $mech.measured$	4.80	6.25
Filter $BW_{vac}(\%)$ $mech.measured$	0.2	0.141

Chapter 5

Conclusions and Future Work

This conclusion reviews the work done, provides highlights and re-statements of the contributions, and outlines planned future work. The thesis includes those parts of the work whose results directly address the problem stated in section 1.1. The method described in Chapter 3 is limited to the work's experimental results reported in Chapter 4. However, the significant effort made on microfabrication of a variety of designs using magnetic transduction were not included in the thesis, although selected parts are briefly mentioned in Appendix A.

The "summary of the work" is a review of this research's background, methods, results, and discussions, including highlighted outcomes of this achievement. The previous work on the problem stated in section 1.1 is restated in a short form to show the position and motivation for this research.

"Contributions" summarizes work achievements based on the corresponding results. Accordingly, restatement of the contributions provides a list of achievements that illuminate the method's benefits for the field. As the research objective was to contribute to the use of micromechanical resonators for RF filter applications by implementing Lorenz force transduction, the contributions of this research are highlighted.

"Future work" lists the aspects of the research that the author plans to continue working on. Product development based on the research results is one significant interest. Commercialization rewards the research efforts, attracts new resources for further development, and provides feedback from users on aspects of the project

not observed initially.

5.1 Summary of the work

Wireless communication systems, including mobile phones, aim at single-chip integrated RF solutions. Mechanical resonators offer Qs in the order of hundreds of times better than those of comparable size using electrical elements. The majority of current mechanical filters and resonators, SAW, FBARs, and Quartz crystals, are off-chip components, that occupy a large space on a chip. Miniaturized mechanical filters fabricated by an IC-compatible technology are important requirements in this development. In addition to providing more space for added functionality, integrated solutions reduce size, lower power consumption, and decrease cost. However, mechanical filters require a transduction mechanism to couple energy between two domains, electrical and mechanical. The literature review on mechanical resonator use in RF filters, the problem statement on the current transduction techniques, the proposed solution of using electrodynamic transduction, research methods and analysis, and experimental work and results are summarized.

Electrostatic and piezoelectric are the two main transduction techniques used in microelectromechanical systems (MEMS) filters. The majority of the reported achievements on MEMS micromechanical filters use electrostatic excitation and capacitive (electrostatic) detection. The simplicity and compatibility of the silicon microstructures with micromachining technology make electrostatic transduction an attractive transduction method. Research on increasing the effective actuation/sensing area (A_0) [7] has not yet led to a significant improvement.

Accordingly, with limitations on increasing the bias voltage or decreasing the electrodes gap, the high motional resistance associated with electrostatic transduction remains a serious problem. Thin piezoelectric resonators demonstrate the advantage of having motional resistance comparable to 50 Ω RF circuits; however, the need for piezoelectric materials and limited Q obtainable compared to non-piezoelectric, electrostatically driven resonators are the method's shortcomings.

For the above-stated problems, this thesis has proposed the use of Lorentz-force transduction for RF micromechanical filters and explored the feasibility of the technique in experimental work on microfabricated resonating structures. In fact, this

research has introduced a method with none of the limitations of the current techniques for the application and with the following advantages: reduced motional resistance integrable with 50 Ω RF circuits, no need for piezoelectric material, ease of fabrication, and compatibility with IC fabrication technologies.

Equivalent circuit modeling of the electromechanical systems is the method used in the analysis of electromechanical systems involving electrodynamic transduction. Equivalent circuit modeling is used to develop a purely electrical or mechanical equivalent circuit model by combining mechanical and electrical elements of an electromechanical system. Single and coupled micromechanical resonators are modeled. The equivalent circuit representation of electromechanical systems reduces to pure electrical circuit at the given resonance frequency.

To implement electrodynamic transduction on micromechanical resonators, microstructure designs for fabrication are described. Single and coupled clamped-clamped microbeams are the resonators whose equivalent circuit models are already introduced. Design of multi-pole electrical filters using micromechanical resonators driven by Lorentz-force transduction is described by providing a detailed design process. The multi-pole filter design is based on standard electrical filter design for RF frequencies. However, the detailed procedure for realizing the coupled micromechanical filters using electrodynamic transduction is provided. Finally, the previous work on mutual inductance effect on the the coupled micromechanical resonators [4] is re-stated to recognize if there is any limitation in using electrodynamic transduction for RF filter application.

Microfabrication of single and coupled resonator designs that are described in Chapter 3 are implemented in several technologies. Experimental setup for providing in-plane and out-of-plane magnetic fields and accommodating chips and providing electrical and optical connections are described. The experimental setup includes a mini-vacuum chamber inside which the test fixtures holding the chips are fixed. The mini-vacuum chamber provides optical access for the laser beam as well as electrical connections to measure the microresonators motions in air and vacuum. Experimental results of using Lorentz-force transduction for micromechanical resonators includes mechanical and electrical measurement.

The reported experimental results have been evaluated using the equivalent circuit models. Greatly reduced motional resistance associated with the electrodynamic transduction is experimentally demonstrated using the equivalent mod-

els. Fabricated single and coupled microresonators in CMOS35 and their demonstrated performance confirm that electrodynamic transduction is achievable in an IC-compatible fabrication technology. Derived by laser vibrometer, mode shapes and resonance specifications of the designs both in air and vacuum provide the data for identifying mechanical performance of the microresonators. Furthermore, electrical measurements in air and vacuum of resonating microstructures facilitates identification of signals with mechanical origin.

The need for an external magnetic field that does not add limitations to mechanical resonators miniaturization and use of electrodynamic transduction is discussed. The mutual inductance effect is re-evaluated, and the possibilities for avoiding this challenge are mentioned. Finally, the consequence of this achievement in experimentally demonstrating use of electrodynamic transduction is listed.

By driving single and coupled microresonators to resonance using Lorentz force, this research has identified further advantages of the technique. Some of these advantages are already demonstrated in this study: compatibility with IC fabrication technologies, greatly reduced motional resistance, ease of fabrication and flexibility in the choice of resonators structural material, higher potential in power handling, and independence of filter center frequency from bias voltage.

A transduction method without the limitations of the current techniques has been proposed and studied in experimental work on microfabricated designs. Equivalent circuit modeling of the microfabricated designs using electrodynamic transduction has been carried out to evaluate the experimental results. Mechanical and electrical measurements in air and vacuum conducted on microstructures result in data that allows for evaluating electrodynamic transduction for RF filter application. The contributions of this research, including greatly reduced motional resistance associated with Lorentz-force transduction, are summarized in section 5.2.

5.2 Contributions

This research uses electrodynamic transduction for micromechanical resonators and demonstrates the feasibility of the technique for RF filter applications. This achievement results in the following contributions to the field: implementation of electrodynamic transduction for RF miniaturized filter applications; design and fabrication of

micromechanical resonators for electrodynamic transduction in various microfabrication technologies, including standard CMOS35; demonstration of greatly reduced motional resistance associated with electrodynamic transduction; adaptation of a design procedure for multi-port micromechanical filters using Lorentz-force transduction; higher mode driving; and experimental evaluation using a laser vibrometer to characterize single and coupled micromechanical resonators for RF filter applications.

Examining the idea of employing Lorentz-force transduction for RF micromechanical filters requires corresponding designs of micromechanical resonators and experimental evaluation. Addressing these requirements is the major outcome and contribution of this research. Implemented electrodynamic transduction for single and coupled micromechanical resonators demonstrates the feasibility, ease of use, and advantages of the proposed technique for RF miniaturized filter applications. Furthermore, the results of this study also show other advantages of electrodynamic transduction over current transduction techniques: independence of the filter center frequency from bias voltage, no need for a piezoelectric material and the corresponding fabrication challenges, higher power handling, no need for bias lines, thus decreasing the work in microfabrication.

The implemented design in CMOS35 (C) with the obtained Q and resonance performance demonstrates that use of electrodynamic transduction in IC-compatible technologies is achievable. These fabricated designs of single and coupled micromechanical resonators based on Lorentz-force transduction present promising performance enhancement in Q and resonance characteristics. Further to implementation in standard CMOS35 fabrication, the Lorentz-force driven micromechanical resonators are also fabricated in other microfabrication technologies including UW-MEMS and PolyMUMPs. The results show that the performance of the electrodynamically driven micromechanical resonators is promising in other technologies too, although implementation of the transduction technique in CMOS35 is more attractive. Smaller feature size and the distance between features in CMOS35 compared to other technologies studied in this research make CMOS technology a preferred fabrication. CMOS35 fabrication technology allows for more flexibility in applying the required coupling for a given bandpass and resonance frequency because of permitted smaller feature size, smaller distance between features, and availability of alternative Oxide and metal layers.

The results of this research contribute to the field by demonstrating multi-

ple orders of magnitude lower motional resistance associated with Lorentz-force transduction for RF micromechanical filters. The greatly reduced motional resistance associated with electrodynamic transduction presented in this work is the very important advantage of the transduction technique for RF micromechanical filters. Large values of motional resistance associated with electrostatic transduction limits its use for RF μmechanical filters. In fact, significant research in more than two past decades on electrostatic transduction for micromechanical filters has been devoted to lowering the corresponding motional resistance. This research provides experimental evidence confirming the feasibility of the proposed Lorentz-force transduction technique and its advantage over electrostatic method for RF filter applications for such a greatly reduced motional resistance. Should a similar device in size be driven electrostatically, the motional resistance can be shown that would be multiple orders of magnitude higher.

Greatly reduced motional resistance has also been computed for single and coupled micromechanical resonators implemented in different microfabrication technologies than CMOS35. The results confirm the low values of motional resistance associated with the electrodynamic transduction technique, regardless of the fabrication technology. The computed motional resistance values derived from experimental results are displayed in 4.1 and 4.2. The reason for this greatly reduced motional resistance is realized from 3.13 and 3.14 illustrating a striking fact: the electromagnetic transduction is an impedance inverter. Being "an impedance inverter" means that a mass reactance on the mechanical side becomes a capacitance reactance on the electrical side of the transformer and vice versa [52]. Similarly, an inductance on the electrical side reflects through the transformer as a mechanical compliance.

Multi-port electrical filter design techniques have been adapted to implement the design of multi-port micromechanical filters that function based on electrodynamic transduction. A detailed design process is described that includes an electrical filter design, computation of the coupling matrix, and realization step. The realization step of the work benefits from this research. Adapting the design technique to realize multi-port micromechanical filter functioning by electrodynamic transduction requires calculation of the resonators' frequency, coupling length, coupling stiffness, coupling location, and input/output couplings. The detailed analysis process is described in section 3.2.

Lorentz-force driven micromechanical resonators in higher modes are reported

in this thesis. For example, a clamped-clamped micromechanical resonator (U2) is driven to its 9th mode. Where the 1st flexural mode of this resonator is at about 95 KHz, the ninth mode resonates at 1.8172 MHz with Q of 3925 in a vacuum. Although no direct evidence can be provided in this step about whether the use of Lorentz-force transduction has enabled this performance, there is the possibility that this higher mode (9th) of driving occurs because of the bi-directional nature of the Lorentz force.

The micromechanical resonators produce very small signal amplitude at the level of a micro volt or fractions of microvolts, whether employed in sensing applications or electrical filtering. Furthermore, identification of the resonance characteristics, mode shape, and coupling beam performance are important in adjusting the design parameters. The use of a laser vibrometer to identify the mode shapes and resonance characteristics of single and coupled micromechanical filters in this research shows a more straightforward method and facilitating technique in characterizing micromechanical resonators before advancing work for electrical performance measurement.

This thesis makes its contributions by examining Lorentz-force transduction for RF micromechanical filters. Experimental work, analysis, and modeling of Lorentz-force transduction for single and coupled resonators, where the modeling is extendable to higher number of coupled resonators, fabrication of single and coupled microstructures driven by electrodynamic transduction, reporting of greatly reduced motional resistance associated with the transduction technique, demonstration of the strength and other advantages of the transduction technique for RF application including independence of filter center frequency from bias voltage, no requirement for bias lines that decrease the work in microfabrication, higher power handling, and no need for piezoelectric material. Furthermore, it provides a detailed process for the design and realization of multi-port micromechanical filters using Lorentz-force transduction, reports higher mode driving of micromechanical resonators, and employs a laser vibrometer to characterize single and coupled micromechanical resonators for the application. A list of selected contributions is given.

- implementing electrodynamic transduction for single and coupled micromechanical resonators for RF miniaturized filter applications
- designing and fabricating micromechanical resonators using electrodynamic transduction in standard CMOS35 microfabrication technology and display-

ing the feasibility of the technique in an IC-compatible microelectronic circuit technology

- reporting multiple orders of magnitude lower motional resistance associated with Lorentz-force transduction for RF micromechanical filters. This greatly reduced motional resistance associated with electrodynamic transduction presented in this work is the very important advantage of using the proposed transduction technique for RF micromechanical filters.

- highlighting other advantages of electrodynamic transduction over current transduction techniques: independence of the filter center frequency from bias voltage, larger electromechanical coupling compared to electrostatic [14], no need for a piezoelectric material and the corresponding fabrication challenges, higher power handling, and no requirement for bias lines, which decreases the work in microfabrication.

- adopting multi-port electrical filter design techniques in implementing design of multi-port micromechanical filters using electrodynamic transduction The detailed analysis process is described in section 3.2.

- employing electrodynamic transduction in driving a clamped-clamped micromechanical resonator (U2) to its higher modes (9th mode)

The results of this research was presented in Transducer Conference 2011 and published in IEEE Computer Society and IEEEXplore [16]. The journal version of the conference paper, "Lorentz force transduction for RF micromechanical filters," was published in the Journal of Micromechanics and Microengieering [17]. The second journal paper reporting another part of the results submitted for publication in Journal of Micromechanics and Microengieering on February 13, 2012.

5.3 Future work

This achievement on experimentally studying Lorentz-force transduction for RF micromechanical filters has initiated work on various aspects of the application. Accordingly, my future work will include research to address the need arising from the research. Furthermore, the potential of the alternative transduction methods introduced in my PhD thesis proposal motivate me to include these studies in my future work:

- Commercialization of the research results to attract resources for further technique development
- Experimental studies on contactless transduction techniques for RF filter needs and other sensing applications: use of eddy-current-based and magnetostriction transduction
- Implementation of multi-pole filters using Lorentz-force transduction for RF application by aiming at developing a product to serve the purpose
- Research on linearity in power handling
- Investigation of electrodynamic transduction in further applications in MEMS, from sensors and actuators to power generators. Each of these topics is interesting and requires the same research background.

References

[1] Kun Wang, Ark-Chew Wong, and Clark T. C Nguyen. VHF free-free beam high-Q micromechanical resonators. *Journal of Microelectromechanical Systems*, 9(3):347–360, 2000.

[2] E. Timothy Shirley. Frequency-pulling effects in microfabricated resonant structures, 1993.

[3] S. J. Martin, M. A. Butler, J. J. Spates, W. Kent Schubert, and M. A Mitchell. Magnetically-excited flexural plate wave resonator. *IEEE Transactions on Ultrasonics, Ferroelectrics and Frequency Control*, 45(5):1381–7, 1998.

[4] F. D. Bannon, J. R. Clark, and C. T. C Nguyen. High-Q HF microelectromechanical filters. *IEEE Journal of Solid-State Circuits*, 35(4):512–26, 04 2000.

[5] Robert A. Johnson 1932. *Mechanical filters in electronics*. Wiley, New York, 1983.

[6] R. Aigner. Mems in rf-filter applications: thin film bulk-acoustic-wave technology. In *Digest of Technical Papers*, volume 1 of *TRANSDUCERS '05. The 13th International Conference on Solid-State Sensors, Actuators and Microsystems*, pages 5–8, Seoul, South Korea, 5-9 June 2005 2005. IEEE.

[7] Gianluca Piazza, Philip J. Stephanou, and Albert P. Pisano. Piezoelectric aluminum nitride vibrating contour-mode MEMS resonators. *Journal of Microelectromechanical Systems*, 15(6):1406–1418, 2006.

[8] Clark T. C Nguyen. Future wireless designs will replace electronics with precision mechanical components. *IEEE Spectrum*, 46(12):30–35, 2009.

[9] Sheng-Shian Li, Yu-Wei Lin, Yuan Xie, Zeying Ren, and C. T. C Nguyen. Micromechanical "hollow-disk" ring resonators. In *Maastricht MEMS 2004 Technical Digest*, 17th IEEE International Conference on Micro Electro Mechanical Systems, pages 821–4, 25-29 Jan. 2004.

[10] Jing Wang, Ling Yang, S. Pietrangelo, Zeying Ren, and C. T. C Nguyen. RF MEMS resonators: getting the right frequency and Q. In *2007 IEEE Compound Semiconductor Integrated Circuit Symposium*, pages 1–4, 14-17 Oct. 2007.

[11] John R. Clark, Wan-Thai Hsu, Mohamed A. Abdelmoneum, and Clark T. C Nguyen. High-Q UHF micromechanical radial-contour mode disk resonators. *Journal of Microelectromechanical Systems*, 14(6):1298–1310, 2005.

[12] Clark T. C Nguyen. Frequency-selective MEMS for miniaturized low-power communication devices. *IEEE Transactions on Microwave Theory and Techniques*, 47(8):1486–1503, 1999.

[13] R. Adler. Compact electromechanical filter. *Electronics*, 20:100–105, 04 1947.

[14] R. S. Woollett. Transducer comparison methods based on the electromechanical coupling-coefficient concept. *IRE National Convention Record*, 5:23–27, 1957.

[15] A. T. Alastalo and V. Kaajakari. Third-order intermodulation in microelectromechanical filters coupled with capacitive transducers. *Journal of Microelectromechanical Systems*, 15(1):141–8, 02 2006.

[16] S. Forouzanfar, R. R. Mansour, and E. Abdel-Rahman. Lorentz force transduction for RF micromechanical filters. In *2011 16th International Solid-State Sensors, Actuators and Microsystems Conference, TRANSDUCERS'11, June 5, 2011 - June 9*, pages 2458–2461, Beijing, China, 2011 2011. IEEE Computer Society.

[17] Sepehr Forouzanfar, Raafat Mansour, and Eihab Abdel-Rahman. Lorentz-force transduction for RF micromechanical filters. *Journal of Micromechanics and Microengineering*, 22(3):035018, 2012.

[18] John T. Taylor and Qiuting Huang. *CRC handbook of electrical filters*. CRC publisher, 1997.

[19] Richard J. Cameron, Chandra M. Kudsia, and Raafat R. Mansour. *Microwave filters for communication systems : fundamentals, design and applications*. John Wiley Sons, Hoboken, N.J., 2007.

[20] Thomas D. Rossing. *Springer handbook of acoustics*. Springer, New York, N.Y., 2007.

[21] S. Fujishima. The history of ceramic filters. *IEEE Transactions on Ultrasonics, Ferroelectrics and Frequency Control*, 47(1):1–7, 01 2000.

[22] Y. Satoh, T. Nishihara, T. Yokoyama, M. Ueda, and T. Miyashita. Development of piezoelectric thin film resonator and its impact on future wireless communication systems. *Japanese Journal of Applied Physics, Part 2 (Letters)*, 44(5):2883–94, 05 2005.

[23] Gianluca Piazza. Piezoelectric aluminum nitride vibrating rf mems for radio front-end technology, 2005.

[24] Yong-Dae Kim, Kuk-Hyun Sunwoo, Sang-Chul Sul, Ju-Ho Lee, Duck-Hwan Kim, In-Sang Song, Sung-Hoon Choa, and Jong-Gwan Yook. Highly miniaturized rf bandpass filter based on thin-film bulk acoustic-wave resonator for 5-ghz-band application. *IEEE Transactions on Microwave Theory and Techniques*, 54(3):1218–1228, 2006.

[25] Desmond F. Sheahan and Robert A. Johnson. *Modern crystal & mechanical filters.* IEEE Press, New York, 1977.

[26] Warren P. (Warren Perry) Mason. *Electromechanical transducers and wave filters.* D. Van Nostrand Co. [1948], New York, 2d ed edition, 19uu.

[27] J. C. Hathaway and D. F. Babcock. Survey of mechanical filters and their applications. *Institute of Radio Engineers – Proceedings*, 45(1):5–16, 1957.

[28] Roger T. Howe and Richard S. Muller. Resonant-microbridge vapor sensor. *IEEE Transactions on Electron Devices*, ED-33(4):499–506, 1986.

[29] William C. Tang, Tu-Cuong H. Nguyen, and Roger T. Howe. Laterally driven polysilicon resonant microstructures. *Sensors and Actuators*, 20(1-2):25–32, 1989.

[30] G. Piazza. Integrated aluminum nitride piezoelectric microelectromechanical system for radio front ends. *Journal of Vacuum Science & Technology A (Vacuum, Surfaces, and Films)*, 27(4):776–84, 07 2009.

[31] Jing Wang, Z. Ren, and C. T. C Nguyen. 1.156-GHz self-aligned vibrating micromechanical disk resonator. *IEEE Transactions on Ultrasonics, Ferroelectrics and Frequency Control*, 51(12):1607–28, 12 2004.

[32] Yuan Xie, Sheng-Shian Li, Yu-Wei Lin, Zeying Ren, and C. T. C. Nguyen. Uhf micromechanical extensional wine-glass mode ring resonators. In *IEEE International Electron Devices Meeting*, pages 39–2, 8-10 Dec. 2003.

[33] S. Pourkamali and F. Ayazi. High frequency capacitive micromechanical resonators with reduced motional resistance using the HARPSS technology. In *Topical Meeting on Silicon Monolithic Integrated Circuits in RF Systems*, pages 147–50, 8-10 Sept. 2004.

[34] John R. Clark, Mohamed A. Abdelmoneum, and Clark T. C Nguyen. Uhf high-order radial-contour-mode disk resonators. In *Proceedings of the 2003 IEEE International Frequency Control Symposium and PDA Exhibition Jointly with the 17th European Frequency and Time Forum*, pages 802–809, May 4-8 2003.

[35] Ark-Chew Wong and C. T. C Nguyen. Micromechanical mixer-filters ("mixlers"). *Journal of Microelectromechanical Systems*, 13(1):100–12, 02 2004.

[36] M. U. Demirci and C. T. C. Nguyen. A low impedance VHF micromechanical filter using coupled-array composite resonators. In *Digest of Technical Papers*, volume 2 of *TRANSDUCERS '05. The 13th International Conference on Solid-State Sensors, Actuators and Microsystems*, pages 2131–4, 5-9 June 2005.

[37] Mehrnaz Motiee. Mems if/rf filters, 2003.

[38] M. Motiee, R. R. Mansour, and A. Khajepour. Micromechanical resonators and filters for microelectromechanical system applications. *Journal of Vacuum Science & Technology B (Microelectronics and Nanometer Structures)*, 24(6):2499–508, 11 2006.

[39] Philip J. Stephanou, Gianluca Piazza, Carolyn D. White, Muthu B. J. Wijesundara, and Albert P. Pisano. Piezoelectric aluminum nitride MEMS annular dual contour mode filter. *Sensors and Actuators, A: Physical*, 134(1):152–160, 2007.

[40] G. Piazza and A. P. Pisano. Two-port stacked piezoelectric aluminum nitride contour-mode resonant MEMS. *Sensors and Actuators A (Physical)*, 136(2):638–45, 05/16 2007.

[41] H. M. Frost, T. L. Szabo, and J. C. Sethares. Flat conductor electromagnetic saw transducer: Theory and experiment. *Metals Technology*, pages 601–603, 1975.

[42] T. L. Szabo and H. M. Frost. Saw electromagnetic transducer design for non-destructive evaluation applications. *IEEE Transactions on Sonics and Ultrasonics*, SU-23(5):323–8, 1976.

[43] S. J. Martin, M. A. Butler, J. J. Spates, W. K. Schubert, and M. A. Mitchell. Magnetically-excited flexural plate wave resonator. In *Proceedings of International Frequency Control Symposium*, pages 25–31, 28-30 May 1997.

[44] Velimir M. Ristic 1936. *Principles of acoustic devices.* Wiley, New York ; Toronto; New York, 1983.

[45] Kyoichi Ikeda, Hideki Kuwayama, Takashi Kobayashi, Tetsuya Watanabe, Tadashi Nishikawa, Takashi Yoshida, and Kinji Harada. Silicon pressure sensor integrates resonant strain gauge on diaphragm. *Sensors and Actuators, A: Physical*, 21(1-3):146–150, 1990.

[46] D. K. Fragoulis and J. N. Avaritsiotis. Acoustic electromechanical resonance filters. *Sensors and Actuators A (Physical)*, A99(3):270–6, 06/05 2002.

[47] A. C. 1. Stevenson and C. R. 1. Lowe. Magnetic-acoustic-resonator sensors (mars): a new sensing methodology. *Sensors and Actuators A (Physical)*, A72(1):32–7, 01/08 1999.

[48] A. C. 1. Stevenson, B. 1. Araya-Kleinsteuber, R. S. 1. Sethi, H. M. 1. Metha, and C. R. 1. Lowe. Planar coil excitation of multifrequency shear wave transducers. *Biosensors and bioelectronics*, 20(7):1298–304, 01/15 2005.

[49] F. Lucklum, B. Jakoby, P. Hauptmann, and N. F. de Rooij. Remote electromagnetic excitation of high-q silicon resonator sensors. In *Proceedings of the 2006 IEEE International Frequency Control Symposium and Exposition*, page 6, 4-7 June 2006 2006.

[50] Dennis S. Greywall. Micromechanical RF filters excited by the lorentz force. *Journal of Micromechanics and Microengineering*, 9(1):78–84, 1999.

[51] Hermann K. P. Neubert. *Instrument Transducers : an Introduction to Their Performance and Design.* Clarendon Press, Oxford (Eng.) : Clarendon Press, 1975; Oxford Eng., 1975.

[52] Leo Leroy Beranek 1914. *Acoustics.* Published by the American Institute of Physics for the Acoustical Society of America, New York, N.Y., 1986.

[53] Friedrich Alexander Fischer. *Fundamentals of electroacoustics. Translated by Stanley Ehrlich and Fritz Pordes.* Interscience Publishers, New York, 19uu.

[54] M. Elwenspoek. *Mechanical microsensors.* Springer, Berlin ; New York, 2001.

[55] Sepehr Forouzanfar. Micro-electro-thermo-magnetic actuators for MEMS applications, 2006.

[56] Aurelio Soma and Alberto Ballestra. Residual stress measurement method in MEMS microbeams using frequency shift data. *Journal of Micromechanics and Microengineering*, 19(9), 2009.

[57] Anatol I. Zverev. *Handbook of filter synthesis [by] Anatol I. Zverev.* New York, Wiley, 1967.

[58] TSMC 0.35 micron process
.

[59] MEMSCAP - the power of a small world
.

[60] UWMEMSDesignHandbook_ver3.pdf
.

[61] T. V. Roszhart. The effect of thermoelastic internal friction on the q of micromachined silicon resonators. In *90CH2783-9)*, Technical Digest. IEEE Solid-State Sensor and Actuator Workshop (Cat. No, pages 13–16. IEEE, 4-7 June 1990.

[62] Aurelio Soma and Alberto Ballestra. Residual stress measurement method in mems microbeams using frequency shift data. *Journal of Micromechanics and Microengineering*, 19(9), 2009.

[63] *CMOS-MEMS.* Wiley-VCH, Weinheim, 2005.

[64] David M. Pozar. *Microwave engineering.* J. Wiley, Hoboken, NJ, 3rd ed edition, 2005.

Appendix A

Magnetic transduction techniques

A.1 Microfabrication for eddy-current based magnetic transduction

Contactless magnetic transduction techniques are very attractive for RF filter application for the unique advantages they provide. One of the most important advantages over other transduction techniques is that driving and sensing do not require electrical connections to the resonators themselves. The no need for electrical connection to the resonators allow for obtaining very large values of Q. The resonators that are not fixed at the edge or sides produce mode shapes of more predictable allowing for their frequency response being less involved with parasitic effect. Pictures taken from fabrications implemented to investigate eddy-current based magnetic transduction are displayed in A.1.

For the configuration displayed in 2.11, if the meander shape conductor is fixed above the conducting substrate's surface and in the proximity of the surface, the configuration enables eddy current transduction implementation. For this configuration, the resistance, $R_0^(M)$, of M, D-long sections and the magnetomechanical coupling, k_m^2, are calculated from (A.1) and (A.2), respectively [44], where $\lambda_R = \lambda_0 = 2D$ is the resonant wavelength of the meander line. L_D is inductance per single D-line section per unit aperture width, w.

$$R_0^{(M)} = 4 f_0 C^2 L_D w M^2 \tag{A.1}$$

$$C[dB] = 20 \log e^{-\pi G/D} \approx -54.6 \frac{G}{\lambda_R} \tag{A.2}$$

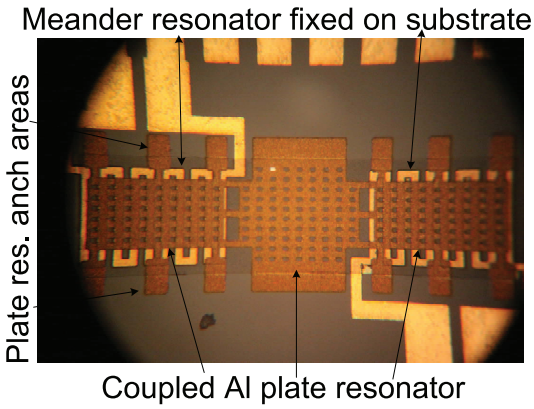

Coupled three plate resonators

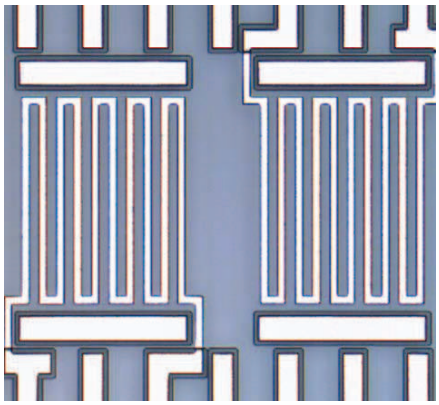

Partially fabricated meander coil

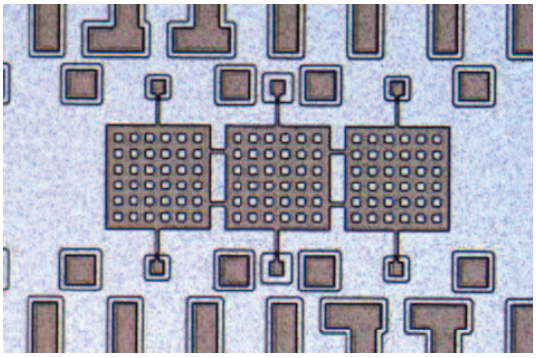

Coupled Al three-plate resonator

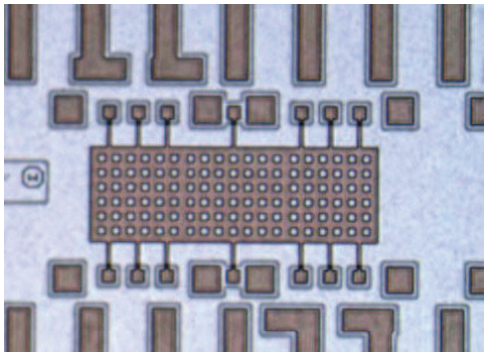

Al plate resonator

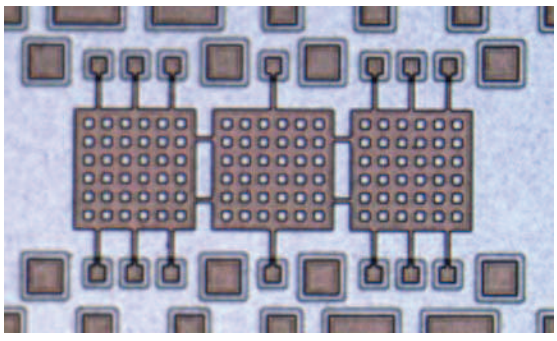

Coupled Al three-plate resonator

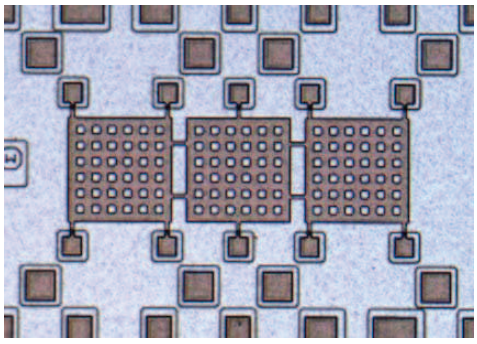

Coupled Al three-plate resonator

Figure A.1: Microfabrication for eddy-current driven microresonators

A.2 Microfabricated meander conductor for Lorentz-force transduction

For the configuration displayed in 2.11, the resistance, $R_0^{(}M)$, of M, D-long sections and the magnetomechanical coupling, k_m^2, are calculated from (A.3) and (A.4), respectively [44], [3]. L_D is inductance per single D-line section per unit aperture width, w.

$$R_0^{(M)} = 4 f_0 k_m^2 L_D w M^2 \tag{A.3}$$

$$k_m^2 = \frac{B^2 v_a D^4}{32 \rho_m f_0 L_D w^2 l} \tag{A.4}$$

Figure A.2 displays one of the fabricated designs for this research using meander shape coil made of gold to excite mechanical resonance in microstructure made of SiO2.

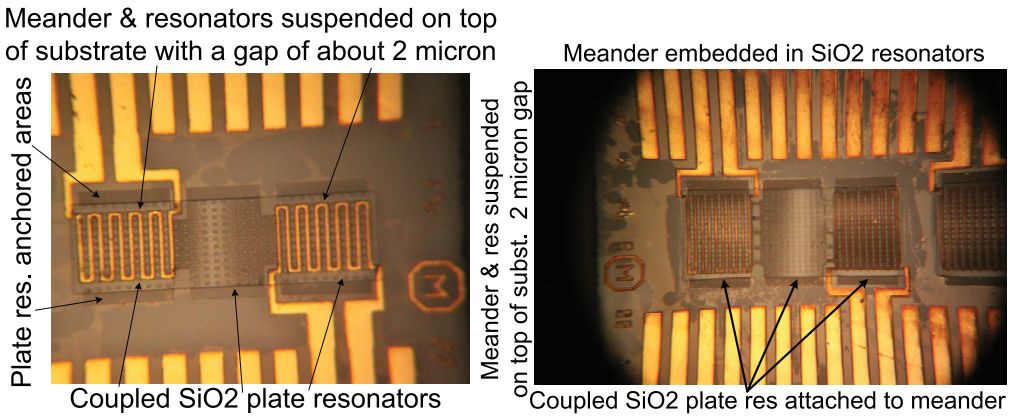

Figure A.2: Lorentz-force driven of microresonators incorporating meander coil

A.3 Magnetostrictive transduction

Magnetostrictive transduction is the second proposed transduction technique for RF MEMS filters that was included in my PhD thesis proposal. Experimental work on this technique was not pursued in practice for limitations in fabrication facilities.

Appendix B

Multi-pole electrical filter design

B.1 g-values computations for multi-pole filter design

Two main stages of electrical filter design are synthesis and approximate modeling. Synthesis is the work on circuit to synthesize the filter response. The initial data such as center frequency, bandwidth, return loss, and filter degree are the inputs for response synthesis. A simplified process for the response synthesis of a two-pole and three-port filter is described in section 3.2. The corresponding g-values specifying the designed filters are taken from filter handbooks or computed. To demonstrate the g-values computation, an assumed frequency and return loss are taken as the initial assumptions for which the corresponding g-values are computed.

For a given return loss of $RL = 25\ dB$, a center frequency of 50 MHz, and a bandwidth of 0.05 MHz, the filter synthesis for a three-pole filter is pursued by first deriving the g-values of a low pass filter providing the accepted ripple value for the band pass or the chosen return loss.

1. the passband ripple level, $1+k^2$, calculated from the insertion loss represented by $IL = 10 \log P_{LR}$ [64]
2. the power loss ratio, P_{LR}, and the passband ripple level are related by $P_{LR} = 1 + k^2 T_n^2 \left(\frac{\omega}{\omega_c}\right)$, where $T_n = \{0$ for n odd and 1 for n even$\}$
3. using the passband ripple level, the low pass prototype's lumped element values, $g_0, g_1, g_2, ..., g_{n+1}$, are computed

The normalized g-values computed for such a low pass three-pole filter with the above specifications are $g1 = 0.6704$, $g2 = 1.0027$, $g3 = 0.6704$, $g4 = 1$. The filter's response derived from these computation is illustrated in B.1.

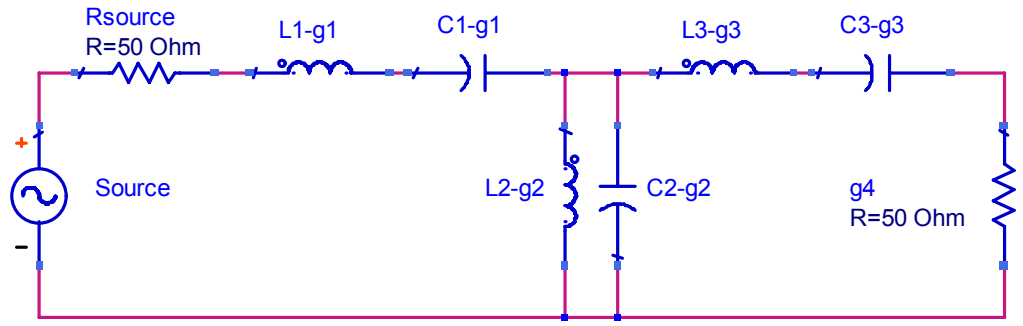

Figure B.1: Scaled g-values representing the filter response

$$\omega \rightarrow \frac{\omega_0}{\omega_2 - \omega_1}\left(\frac{\omega}{\omega_0} - \frac{\omega_0}{\omega}\right) = \frac{1}{\Delta}\left(\frac{\omega}{\omega_0} - \frac{\omega_0}{\omega}\right) \tag{B.1}$$

$$\Delta = \frac{\omega_2 - \omega_1}{\omega_0},\ \omega_0 = \sqrt{\omega_1 \omega_2} \tag{B.2}$$

Later, the prototype's lumped elements are scaled to derive a band pass response at the chosen example center frequency of 50 MHz. Accordingly, the scaled g-values displayed in B.1 are obtained:
$L1g1 = 106.7\ \mu H$
$C1g1 = 0.095\ pF$
$L2g2 = 0.159\ nH$
$C2g2 = 63.834\ nF$
$L3g3 = 106.7\ \mu H$
$C3g3 = 0.095\ pF$
$g4 = 50\ \Omega$.

Figure B.2 displays the filter's simulation in ADS using scaled g-values. The scaling process are through the following steps.

- the series inductor, L_k, is converted to a series LC circuit whose elements' values are $\acute{L}_k = \frac{L_k}{\Delta\omega_0}$ and $\acute{C}_k = \frac{\Delta}{L_k\omega_0}$.

- the shunt capacitor, C_k, is converted to a shunt LC circuit whose elements' values are $\acute{L}_k = \frac{\Delta}{C_k \omega_0}$ and $\acute{C}_k = \frac{C_k}{\Delta \omega_0}$.
- the source and load impedance scaled proportionally: $\acute{R}_s = R_0$ and $\acute{R}_L = R_0 R_L$

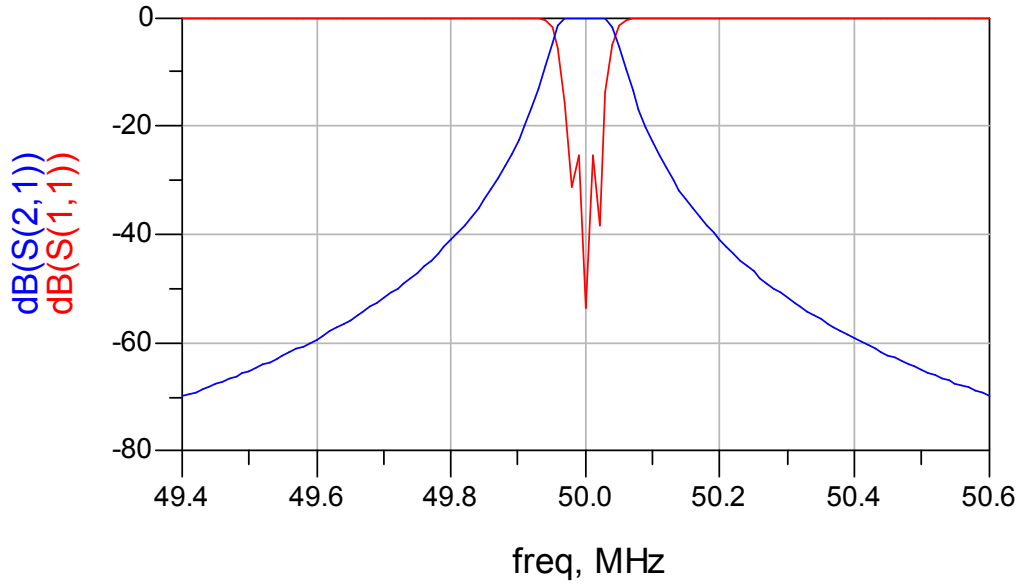

Figure B.2: Simulated in ADS scaled g-values for the 3-pole filter

B.2 Y-matrix elements computation

The relationship between ABCD matrix elements in B.3 and Y matrix in B.4 are given in B.5.

$$\begin{bmatrix} F_1 \\ v_1 \end{bmatrix} = \begin{bmatrix} A & B \\ C & D \end{bmatrix} \begin{bmatrix} F_2 \\ v_2 \end{bmatrix} \tag{B.3}$$

$$\begin{bmatrix} F_1 \\ F_2 \end{bmatrix} = \begin{bmatrix} Y_{11} & Y_{12} \\ Y_{21} & Y_{22} \end{bmatrix} \begin{bmatrix} v_1 \\ v_2 \end{bmatrix} \tag{B.4}$$

$$A = -\frac{Y22}{Y21}, \quad B = -\frac{1}{Y21}, \quad C = -\frac{Y11Y22 - Y12Y21}{Y21}, \quad D = -\frac{Y11}{Y21} \tag{B.5}$$

According to the given values of the π-network of 3.13, the corresponding elements of ABCD matrix are computed from B.5 as displayed in B.6.

$$Y_{11} = Y_{22} = Ya + Yb,\ Y_{12} = Y_{21} = -Yb,\ \Rightarrow\quad A = D = 0,\ B = \frac{1}{Yb},\ C = -Yb \tag{B.6}$$

Figure B.3 illustrates a pi-network using Y-parameters to represent a coupling

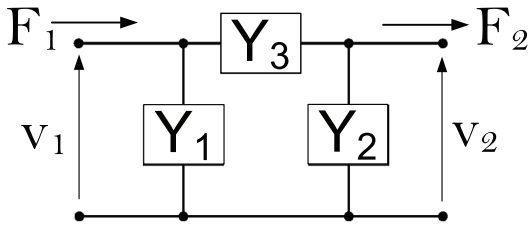

Figure B.3: Pi-network representation for Y-parameters of a coupling beam

beam. Equation B.7 shows the effort-flow relationships in using mobility analogy for a two-port representation of a coupling beam.

$$F_1 = Y1v_1 + Y3(v_1 - v_2) = (Y1 + Y3)v_1 - Y3v_2 = Y_{11}v_1 + Y_{12} \times v_2 \tag{B.7}$$

$$F_2 = Y3(v_2 - v_1) + Y2v_2 = -Y3v_1 + (Y2 + Y3)v_2 = Y_{21}v_1 + Y_{22}v_2 \tag{B.8}$$

Appendix C

Videos of measured mode shapes and mechanical vibrations

C.1 Micromechanical resonators in motion 4.1

This Appendix includes a few selected mechanical measurements "avi" files. These videos display identified by laser vibrometer mode shapes of Lorentz-force driven micromechanical resonators that are reported in section 4.2.

1. Electrodynamically driven single microresonator:

   - $CFirstModeAir1.avi$
     1st flexural mode of C, CMOS35 fabricated single resonator whose specifications are given in 4.1
   - $PFirstMode1.avi$
     1st flexural mode of P, PolyMUMPs fabricated single resonator whose specifications are given in 4.1
   - $U1FirstModeAir1.avi$
     1st flexural mode of U1, UW-MEMS fabricated single resonator whose specifications are given in 4.1
   - $U2FifthMode1.avi$
     1st flexural mode of U2, UW-MEMS fabricated single resonator whose specifications are given in 4.1
   - $U2ThirdmodeAir1.avi$
     3rd flexural mode of U2, UW-MEMS fabricated single resonator in air whose specifications are given in 4.1

- *U2ThirdmodeVac1.avi*
  3rd flexural mode of U2, UW-MEMS fabricated single resonator in vac whose specifications are given in 4.1
- *U2Thirdmode1.avi*
  3rd flexural mode of U2, UW-MEMS fabricated single resonator whose specifications are given in 4.1
- *U2FifthmodeVac1.avi*
  5th flexural mode of U2, UW-MEMS fabricated single resonator in vac whose specifications are given in 4.1

2. Electrodynamically driven CMOS35 fabricated coupled two-microresonators:

   - *AFirstModeInphase3.avi*
     1st flexural mode shape of A CMOS35 fabricated whose specifications are given in 4.2
   - *AFirstModeOutphase3.avi*
     1st flexural mode shape of A CMOS35 fabricated whose specifications are given in 4.2
   - *BFirstModeInphase2.avi*
     1st flexural mode shape of B CMOS35 fabricated whose specifications are given in 4.2
   - *BFirstModeOutphase2.avi*
     1st flexural mode shape of B CMOS35 fabricated whose specifications are given in 4.2
   - *AThirdmodeInphase2.avi*
     3rd flexural mode shape of A CMOS35 fabricated whose specifications are given in 4.2
   - *AThirdModeOutphase2.avi*
     3rd flexural mode shape of A CMOS35 fabricated whose specifications are given in 4.2

3. Electrodynamically driven UW-MEMS fabricated coupled two-microresonators:

   - *CoupledUWMEMShigherMode1.avi*
     Coupled UW-MEMS resonators at its 5th mode with the coupling at the mid-point
   - *CoupUWMEMSQuartInphase1.avi*
     Coupled UW-MEMS resonators at its 1st mode with the coupling at the quarter-point

- *CoupUWMEMSQuartOutphase*1.*avi*
  Coupled UW-MEMS resonators at its 1st mode with the coupling at the quarter-point
- *CoupUWQuartInphase*1.*avi*
  Coupled UW-MEMS resonators at its 1st mode with the coupling at the quarter-point in air
- *CoupUWQuartOutphase*1.*avi*
  Coupled UW-MEMS resonators at its 1st mode with the coupling at the quarter-point in vac
- *CoupUWMEMS*476*KHzInphase*1*stMode.avi*
  Coupled UW-MEMS resonators at its 1st mode with the coupling at the quarter-point
- *CoupUWMEMS*598*KHzOutphase*1*stMode.avi*
  Coupled UW-MEMS resonators at its 1st mode with the coupling at the quarter-point

4. Electrodynamically driven CMOS35 fabricated coupled three-microresonators:

   - *DFirstModeInphase*3.*avi*
     1st flexural mode shape of coupled three-resonators
   - *DFirstModeInphase*5.*avi*
     1st flexural mode shape of coupled three-resonators
   - *DFirstModeInOutphse*1.*avi*
     1st flexural mode shape of coupled three-resonators
   - *DFirstModeOutphase*2.*avi*
     1st flexural mode shape of coupled three-resonators
   - *DFirstModeOutphase*3.*avi*
     1st flexural mode shape of coupled three-resonators
   - *DFirstModeOutphase*4.*avi*
     1st flexural mode shape of coupled three-resonators
   - *DFirstModeOutphase*5.*avi*
     1st flexural mode shape of coupled three-resonators
   - *DFirstModeOutphase*6.*avi*
     1st flexural mode shape of coupled three-resonators
   - *DFirstModeOutphase*7.*avi*
     1st flexural mode shape of coupled three-resonators

- $DFirstModeOutphase8.avi$
  1st flexural mode shape of coupled three-resonators
- $DFirstModeOutphase9.avi$
  1st flexural mode shape of coupled three-resonators
- $DThirdModeInphase1.avi$
  3rd flexural mode shape of coupled three-resonators
- $DThirdModeInphase2.avi$
  3rd flexural mode shape of coupled three-resonators

Appendix D

Notes

D.1 "Quotes"

"Of the forty-three scientists who, since 1912, have contributed most to radio's scientific development and progress, only two have received compensation in any way commensurate with their achievements. We have here a complex and serious economic phenomenon. Great discoveries are made and the discovers profit little. The public which owns the ether...profits little. A third party steps in and, discovering nothing, inventing nothing, and owning nothing, nevertheless, makes great fortunes." George Henry Payne, Commissioner, Federal Communications Commission (FCC), 1936 [Erickson 211]

"The fruits of scientific discovery over the centuries became a part of our everyday lives as a result of decades of work by inventors and entrepreneurs scattered across the world. Many scientists were not inventors, and many inventors were not entrepreneurs, either because they were not capable of or were not interested in attempting to fill more than one role. The history of the development of the radio industry from which today's high-tech entrepreneurs may draw some lessons illustrates that a new, technologically-based industry is like a coral reef. The top, living layer of coral rests on a large body of material laid down over the eons. Likewise, the technologically-based industry rests upon a large body of scientific and technological knowledge ac-

cumulated over the centuries. As had been true of an earlier" from http://www.myspace.com/523077219/comments